Role of Surface Evapotranspiration on Moist Convection along the Eastern Flanks of the Andes

by

Xiaoming Sun

Department of Civil and Environmental Engineering
Duke University

Date:_____

Approved:

_____
Ana P. Barros, Supervisor

_____
Gary M. Lackmann

_____
Yuh-Lang Lin

_____
Miguel A. Medina

_____
Wenhong Li

Dissertation submitted in partial fulfillment of
the requirements for the degree of Doctor
of Philosophy in the Department of
Civil and Environmental Engineering in the Graduate School
of Duke University

2014

ABSTRACT

Role of Surface Evapotranspiration on Moist Convection along the Eastern Flanks of the Andes

by

Xiaoming Sun

Department of Civil and Environmental Engineering
Duke University

Date:_____

Approved:

_____
Ana P. Barros, Supervisor

_____
Gary M. Lackmann

_____
Yuh-Lang Lin

_____
Miguel A. Medina

_____
Wenhong Li

An abstract of a dissertation submitted in partial
fulfillment of the requirements for the degree
of Doctor of Philosophy in the Department of
Civil and Environmental Engineering in the Graduate School of
Duke University

2014

Abstract

The contribution of surface evapotranspiration (ET) to moist convection, cloudiness and precipitation along the eastern flanks of the Andes (EADS) was investigated using the Weather Research and Forecasting (ARW-WRF3.4.1) model with nested simulations of selected weather conditions down to 1.2 km grid spacing. To isolate the role of surface ET, numerical experiments were conducted using a quasi-idealized approach whereby at every time step the surface sensible heat effects are exactly the same as in the reference simulations, whereas the surface latent heat fluxes are prevented from entering the atmosphere.

Energy balance analysis indicates that local surface ET along the EADS influences moist convection primarily through its impact on conditional instability, because it acts as an important source of moist entropy in this region. The energy available for convection decreases by up to ~60% when the ET contribution is withdrawn. In contrast, when convective motion is not thermally driven, or under conditionally stable conditions, latent heating from the land surface becomes secondary. At the scale of the Andes proper, removal of surface ET weakens upslope flows by increasing static stability of the lower troposphere, as the vertical gradient of water vapor mixing ratio tends to be less negative. Consequently, moisture convergence is reduced over the EADS. In the absence of local surface ET, this process operates in

concert with damped convective energy, suppressing cloudiness, and decreasing daily precipitation by up to ~50% in the simulations presented here.

When the surface ET is eliminated over the Amazon lowlands (AMZL), the results show that, without surface ET, daily precipitation within the AMZL drops by up to ~75%, but nearly doubles over the surrounded mountainous regions. This dramatic influence is attributed to a dipole structure of convergence-divergence anomalies over the AMZL, primarily due to the considerable cooling of the troposphere associated with suppressed convection. Further examination of moist static energy evolution indicates that the net decrease in CAPE (Convective Available Potential Energy) over the AMZL is due to the removal of surface ET that is only partially compensated by related regional circulation changes. Because of the concave shape of the Andean mountain range, the enhanced low-level divergence promotes air mass accumulation to the east of the central EADS. This perturbation becomes sufficiently strong around nightfall and produces significant eastward low-level pressure gradient force, rendering wind currents more away from the Andes. Moisture convergence and convection over the EADS vary accordingly, strengthened in the day but attenuated at night. Nocturnal convective motion, however, is more widespread. Analytical solutions of simplified diagnostic equations of convective fraction suggest that reduction of lower troposphere evaporation is the driving mechanism. Additional exploratory experiments mimicking various levels of thinning and densification of AMZL forests via changes in surface ET

magnitude demonstrate that the connection between the AMZL ET and EADS precipitation is robust.

Dedication

This dissertation is dedicated to my beloved mother Yueyun Ji (1950-2002).

Contents

List of Tables

List of Figures

Acknowledgements

First, I would like to show my great gratitude to my advisor, Dr. Ana P. Barros, for her patient guidance, constant encouragement, support and understanding. I also would like to thank my Ph.D. committee members, Drs. Gary M. Lackmann, Yuh-Lang Lin, Miguel A. Medina and Wenhong Li, for their valuable comments and suggestions.

I offer my sincere thanks to many research scientists at the National Center for Atmospheric Research for their advices during my three months visit at NCAR, in particular Drs. Fei Chen, Michael Barlage and Jimy Dudhia.

Special appreciation goes to Dr. Roni Avissar for the one-to-one instruction on Boundary Layer Meteorology and the faculty members of the Department of Marine, Earth and Atmospheric Sciences at NCSU, including Drs. Matthew D. Parker, Lian Xie, Anantha R. Aiyyer and Walter A. Robinson, for teaching me Atmospheric Dynamics and Mesoscale Modeling.

My group members provided wonderful time at Duke, especially Do-Hyuk Kang, Prabhakar Shrestha, Julien Brun and Miguel Nogueira, among others. Many thanks to my beloved wife Xiao Kan and little girl Alyssa Sun, without them I would have not been able to study here and finish my Ph. D. Lastly, my heartfelt appreciation to my parents.

1 Introduction

1.1 Motivation

Averaged over the globe, more than half of the solar energy absorbed at the land surface is used to evaporate water (Trenberth et al. 2009). The connection between surface evapotranspiration (ET) and precipitation, however, is difficult to establish unambiguously, as it varies from region to region and a large number of interacting thermodynamic and dynamical processes are involved (Shukla and Mintz 1982). Recently, based on in situ measurements (FLUXNET), meteorological and remote-sensing observations, Jung et al. (2010) reported a decline trend of terrestrial ET after the major El Niño event in 1998. Although whether this reduction is a natural oscillation or a climate change signal remains elusive, and whether it is due to increased soil moisture limitation (Jung et al. 2010) or through directly or indirectly induced anthropogenic diming associated with increased cloudiness (Oliveira et al. 2011; Wild 2012) is unclear, it is not unexpected that atmospheric convection would be altered, especially in the tropics, where diabatic heating acts as the primary convective energy source.

Over mountainous regions, moisture budget analysis at the diurnal time-scale has drawn attention to the contribution of surface ET to the observed precipitation. For instance, using observations from the Monsoon Himalayan Precipitation Experiment (MOHPREX) and the NCEP-NCAR reanalysis, Barros and Lang (2003) estimated that

~15-35% of daily surface ET is recycled at the ridge-valley scale in the central Himalayas. This result is in keeping with Bhushan and Barros (2007) focusing on the inner Sierra Madre Mountains in Mexico, and consistent with Iwasaki (2004), who attributed a daily increase of precipitable water on the order of 2 to 5 mm to surface ET and ridge-valley circulations around Mount Tanigawa in Japan. Barros and Lang (2003) also reported a close agreement between the diurnal cycle of precipitable water and the diurnal cycle of CAPE, both peaking before late afternoon convective initiation. Elucidating the role of surface ET on cloud formation and precipitation processes in regions of complex terrain, and orographic convection in particular, is a central objective of this research.

About 60-70% of the world's population relies on mountains for freshwater needs (United Nations, 2002 International year of the Mountains, http://www.mountains2002.org), and mountains host the greatest biodiversity in the planet. Evolving in special niches but isolated from others, mountain ecosystems are particularly sensitive to environmental change (Thomas et al. 2004). Among them, montane cloud forests in the tropics generally, and along the eastern slopes of the Andes in particular, are especially vulnerable, since these ecosystems resort to persistent low level cloudiness for additional water and nutrients (Beiderwieden et al. 2007).

Spanning across the entire South America from north to south, the environment of the Andes cordillera is strongly influenced by the climate systems over this continent.

For example, previous studies have suggested prominent impacts from the Bolivian high, a southwestward propagating Rossby wave forced by the condensational heating over the Amazon (Gill 1980; Lenters and Cook 1997). As shown in Garreaud (1999), a reinforced and southward displaced Bolivian high can promote upslope moisture transport through enhanced easterlies. He argued that the resultant increased boundary layer moisture is of significance on feeding deep convection over the largely semi-arid Altiplano, a plateau (~3800 in height) along the Andes approximately 250 km in width and roughly spans from 15°S to 22°S. In the lower troposphere, the year-round South American Low Level Jet (SALLJ) carries warm and moist air from the Amazon basin southward to 35°S (Garreaud et al. 2009). With its core ranging from 1 to 1.5 km in height, this low level jet can be an important moisture source for the eastern slopes of the Andes (Giovannettone and Barros 2009). Quantifying the impact of Amazonian ET on moisture transport and convection along the eastern slopes of the Andes is another focus of this thesis.

Understanding the relative contributions of remote (Amazon lowlands) and local (eastern Andes) surface ET to observed precipitation is also of specific regional interests, stemming from concerns with Amazonian deforestation in the past decades (Skole and Tucker 1993; Walker et al. 2011), and the upward migration of alpine plants and tree lines potentially induced by global warming via raised cloud base and decreased

precipitation (Peñuelas and Boada 2003). Compared with earlier efforts toward deforestation or land-use land-cover (LULC) changes in the Amazon (e.g., Dickinson and Kennedy 1992; Werth and Avissar 2002; Costa et al. 2007; Mei and Wang 2010; Medvigy et al. 2011; among many others) using General Circulation Models (GCMs), which tend to bias the near-surface temperature and humidity and produce incorrect surface fluxes (Dirmeyer et al. 2006), the numerical simulations were conducted by a mesoscale model at very high resolution (down to 1.2 km grid spacing). To obtain an essential view of atmospheric response when surface moisture supplies are modified, the role of surface ET was isolated from other processes induced by changes of other land surface attributes, such as albedo, surface roughness and Bowen ratio. This was accomplished using an assembled land surface model as detailed in Chapter 2. In contrast with previous studies over mountainous regions (e.g., Barros and Lang 2003; Iwasaki 2004; Bhushan and Barros 2007; among others), where the contribution of surface ET was primarily inferred as the residual in the atmospheric moisture budget, we concentrate more on energetics.

1.2 Hypothesis and Research Objectives

Building on previous work, and recognizing that in arid mountain regions, and despite significant moisture transport aloft, drought is persistent, the research hypothesis investigated here is that surface latent heat fluxes account for a large portion

of energy transferred from the land surface to the atmosphere, and that this energy is necessary to trigger convective activity and explain the observed diurnal cycle of orographic clouds and rainfall. The research objectives are to understand

1) The relative contribution of local and remote (from the Amazon) surface ET to atmospheric convection over the eastern flanks of the Andes (EADS);

2) How the local surface ET over the EADS impacts thermodynamic properties of the lower troposphere, and whether relevant mountain range scale feedbacks exist;

3) Once the Amazonian surface ET is withdrawn, how the large-scale atmosphere would adjust and what are the mechanisms behind;

4) How moisture transport and convective motion over the EADS is connected with Amazonian ET.

1.3 Overview of the Thesis

Chapter 2 introduces the assembled land surface, which provides a clear representation of the land surface sensible heat effects in the Weather Research and Forecasting (ARW-WRF3.4.1) model. This is important because it offers the framework to isolate the role of surface ET on moist convection from processes associated with other land surface properties. The simulations involved are reviewed and the relevant modifications of ARW-WRF3.4.1 are detailed.

Chapter 3 reviews the methodologies employed to quantify the role of surface ET. Specifically, surface ET and precipitation are incorporated into the hydrostatic surface pressure tendency equation, the apparent heat source and apparent moisture sink in σ-coordinates are derived, and the calculation of temperature tendency over irregular areas are illustrated, which is also applicable to the column integrated moist static energy analysis.

Chapter 4 evaluates model performance through analyses of numerous observational comparisons, including the products from the Tropical Rainfall Measuring Mission (TRMM), the Geostationary Operational Environmental Satellite (GOES) images, and the rainguge and sounding observations obtained during the South American Low Level Jet Experiment (SALLJEX).

Chapter 5 studies how local surface ET impact moist convection along the eastern flanks of the Andes, mainly from an energy perspective.

Chapter 6 investigates the influences of Amazonian ET, with an emphasis toward the eastern flanks of the Andes. Besides numerical analyses, a simple analytical solution of convective fraction is formulated.

Chapter 7 concludes this research, with future work suggested.

2 Isolating the Role of Surface ET: A Quasi-idealized Approach

To isolate the role of surface ET, the moderate-complex Noah land surface model (Chen and Dudhia 2001, henceforth Noah) and the revised MM5 surface layer (Jimenéz et al. 2012, henceforth RMM5) in the Advanced Research Weather Research and Forecasting (ARW-WRF3.4.1, Skamarock et al. 2008) model was simplified as an *assembled land surface*. It essentially contains merely 13 variables, representing the feedbacks from the land surface to the atmosphere. Given these variables, also referred as "connectors" in this dissertation, formulate the only path from the land surface to the atmosphere, provided their values are exactly the same at *every time step*, any simulation shall produce identical atmosphere even in the absence of Noah and RMM5 (see section 2.1.1 for the verification). This offers the chance to define surface sensible heat effects, i.e., any temperature related variables involved in the computation of these connectors. Consequently, if at *each time step* the surface sensible heat effects are exactly the same as in the reference runs while surface moisture and latent heat fluxes vary according to artificial specifications, e.g., completely removed from the atmosphere, the role of surface ET can be isolated.

Section 2.1 describes the assembled land surface. Specifically, section 2.1.1 documents the connectors from the land surface to the atmosphere and shows that its 13

connectors from the land surface to the atmosphere are sufficient and necessary; section 2.1.2 defines surface sensible heat effects, after a thorough examination of the relevant codes detailed in section 2.1.3. Experiment design is overviewed in section 2.2, with the implementation in ARW-WRF3.4.1 detailed in Section 2.3.

2.1 The Assembled Land Surface

2.1.1 Connectors from the Land Surface to the Atmosphere

In ARW-WRF3.4.1 *with the configurations described in Section 2.2*[1], the feedback from the land surface to the atmosphere can be described as

$$F_{LA} = f\left(\alpha,\ \varepsilon,\ T_{sk},\ H,\ E,\ z_0,\ F_{\psi_m},\ F_{\psi_h},\ R_B,\ u_{10},\ v_{10},\ u_*,\ U_L\right), \quad (2.1)$$

where α is albedo; ε is emissivity; T_{sk} is surface skin temperature; H and E denote surface sensible and moisture fluxes respectively, and note that surface latent heat flux LE can be derived from E; z_0 is the surface roughness length; F_{ψ_m} (F_{ψ_h}) is a function of stability function for momentum ψ_m (heat/moisture ψ_h); R_B represents bulk Richardson number; u_{10} and v_{10} are the 10 m wind speed; u_* is the frictional velocity; and U_L represents the adjusted lowest model level wind speed to adapt free convection conditions (Beljaars 1995) with sub-grid velocity scale considerations (Mahrt and Sun 1995). Among them, α, ε and T_{sk} are calculated in the Noah land surface model (Chen

[1] Equation (2.1) is model and parameterization dependent.

and Dudhia 2001, henceforth Noah) and impact atmospheric radiation; H and E are from Noah or the revised MM5 surface layer (Jiménez et al. 2012, henceforth RMM5), depending on over land or water; the surface roughness z_0 can be time variant when snowfall is present or externally specified and updated in Noah; the remainder variables are evaluated in RMM5, thereafter, along with z_0, H and E, entering into the YSU boundary layer scheme [Hong et al. 2006; and see section 2.1 of Sun and Barros (2013) for the key processes of this parameterization].

The variables in Eq. (2.1) are referred to hereafter as the "connectors" *from the land surface to the atmosphere*, in the sense that, provided their values are exactly the same *at every time step*, any simulation shall produce identical atmosphere no matter how the Noah and/or RMM5 are modified. In other words, the connectors in Eq. (2.1) constitute *an assembled land surface model, including the surface layer as well as the land surface scheme*. To verify the diagnosed connectors and the validity of this approach, a group of one-hour experiments were conducted. One of them is a typical real-data case simulation (VERF_CNTL) with the connectors outputted at every time step. In another simulation (VERF_CONC), various variables in the Noah and RMM5 are multiplied by arbitrary numbers (artificially crashing the Noah and RMM5), but with the connectors from the VERF_CNTL imposed at each time step. The remaining experiments are replicates of VERF_CONC, except for imposing extra variables (e.g., soil moisture and soil

temperature) besides the diagnosed connectors (VERF_MORE) or only a subset of the 13 connectors (VERF_LESS). Using the same workstation and identical number of computer cores, VERF_CONC and VERF_MORE reproduced exactly the same atmosphere as in the VERF_CNTL, whereas any member of VERF_LESS failed in this respect, suggesting that the 13 connectors in Eq. (2.1) are necessary and sufficient.

2.1.2 The Land Surface Sensible Heat Effect

The *assembled land surface model* described above offers the chance to define the land surface sensible heat effects, including the impacts on radiation, diffusion and stability. Obviously, α, ε, T_{sk} and H belong to the surface sensible heat variables, but not E and z_0. For the remaining connectors, detailed examinations of ARW-WRF3.4.1 in Section 2.1.3 reveal that[2]

$$F_{\psi_m,\,\psi_h} = f\left(z_0,\ z_L,\ \psi_m,\ \psi_h\right) \tag{2.2}$$

$$R_B = f_i\left(z_0,\ z_L,\ \frac{z_L}{L_{MO}},\ \theta_L,\ \theta_{vL},\ U_L,\ \theta_v,\ \psi_m,\ \psi_h\right) \tag{2.3}$$

$$u_{10},\ v_{10} = f\left(z_0,\ z_L,\ u_L,\ v_L,\ \psi_m\right) \tag{2.4}$$

$$u_* = f\left(z_0,\ z_L,\ U_L,\ \psi_m\right) \tag{2.5}$$

$$U_L = f\left(\theta_L,\ u_L,\ v_L,\ \rho_{aL},\ h_{PBL},\ T_{sk},\ H,\ E,\ \theta_g,\ \theta_v,\ q_s,\ \Delta_h\right), \tag{2.6}$$

---

[2] The symbol f in the following equations represents general relationships.

where

$$\psi_m,\ \psi_h = f\left(\frac{z}{L_{MO}},\ R_B\right)\ (z\ \text{can be}\ \frac{z_0}{L_{MO}},\ \frac{z_L+z_0}{L_{MO}},\ \frac{10+z_0}{L_{MO}}\ \text{or}\ \frac{2+z_0}{L_{MO}}) \tag{2.7}$$

$$\theta_v=\theta_g\left(1+0.61q_s\right) \tag{2.8}$$

$$\theta_g=T_{sk}\left(\frac{p_0}{p_s}\right)^{R/c_p} \tag{2.9}$$

$$q_s = f\left(r_L,\ E_p,\ E_d,\ E_c,\ E_t,\ C_H,\ \sigma_{snow}\right) \tag{2.10}$$

$$E_p = f\left(\varepsilon,\ L_v,\ T_L,\ \theta_L,\ q_L,\ q_L^*,\ \left(\frac{dq^*}{dT}\right)_L,\ \rho_{aL},\ p_L,\ SW_{dn},\ LW_{dn},\ G,\ P,\ C_H\right) \tag{2.11}$$

$$E_d = f\left(\sigma_f,\ E_p,\ \Theta_1,\ \Theta_{ref},\ \Theta_w\right) \tag{2.12}$$

$$E_c = f\left(\sigma_f,\ E_p,\ W_{canp},\ S\right) \tag{2.13}$$

$$E_t = f\left(\sigma_f,\ E_p,\ B_c,\ W_{canp},\ S\right) \tag{2.14}$$

$$C_H = f\left(z_0,\ z_L,\ \rho_{aL},\ u_*,\ \psi_m,\ \psi_h\right) \tag{2.15}$$

$$B_c = f\left(\varepsilon,\ L_v,\ T_L,\ \left(\frac{dq^*}{dT}\right)_L,\ \rho_{aL},\ p_L,\ P,\ C_H,\ R_c\right) \tag{2.16}$$

$$G = f\left(K_t,\ T_{sk},\ T_{soil1},\ D_{soil1},\ D_{snow}\right) \tag{2.17}$$

$$W_{canp} = f\left(\sigma_f,\ E_c,\ P,\ D\right) \tag{2.18}$$

$$K_t = f\left(\Theta,\ \Theta_H,\ \Theta_s,\ S_q\right) \tag{2.19}$$

$$\Theta_H = f_i\left(\Theta,\ \Theta_{ice},\ \Theta_s,\ T_{soil},\ T_{soilB},\ \psi_s,\ b\right). \tag{2.20}$$

In the above, *subscript* L denotes variables at the lowest mass level of the Arakawa-C grid, with z and Δ_h as the model height and horizontal grid spacing respectively. Most of the notations are conventional, where ρ_a is air density, h_{PBL} represents boundary layer height, r is water vapor mixing ratio, q is specific humidity (q^* corresponding to the saturated value, with $\left(\frac{dq^*}{dT}\right)_L$ as the slope of saturated specific humidity curve at T_L), SW_{dn} (LW_{dn}) is downward shortwave (longwave) radiation, G is ground heat flux, P is precipitation, and D_{snow} (σ_{snow}) describes snow depth (cover fraction). The symbols E_p, E_d, E_c and E_t represent potential evaporation, ground surface evaporation, canopy evaporation and canopy evapotranspiration respectively. Other vegetation related variables include green vegetation fraction (σ_f), intercepted canopy water content (W_{canp}), drip (D), maximum canopy capacity (S), plant coefficient (B_c) and canopy resistance (R_c). For the soil, T_{soil} denotes soil temperature, with its top layer and bottom values indicated by T_{soil1} and T_{soilB} correspondingly; Θ is the volumetric soil moisture, using Θ_1 for its top layer values; Θ_H, Θ_{ice} and Θ_s represent liquid, frozen and maximum volumetric soil moisture content; Θ_{ref} and Θ_w are field capacity and wilting point; K_t is soil thermal conductivity; ψ_s is the saturation soil matric potential; both quartz content S_q and constant b are soil type dependent, but not for the top layer

soil depth (D_{soil1}). Note that the stability parameter $\frac{z}{L_{MO}}$ is computed as one quantity in RMM5, with the Monin-Obukhov length L_{MO} diagnosed thereafter. Instead of dimensionless, wind speed is incorporated in the exchange coefficient C_H. The symbol f_i in Eqs. (2.3) and (2.20) indicates that numerical iterations are involved, rather than explicit.

An inspection of Eqs. (2.2) to (2.20) indicates that T_{sk}, T_{soil} and T_{soilB} are indispensible to obtain connectors F_{ψ_m}, F_{ψ_h}, R_B, u_{10}, v_{10}, u_* and U_L. As the 13 connectors are the only path from the land surface to the atmosphere, the land surface sensible heat effects are therefore represented by α, ε, T_{sk}, H, T_{soil} and T_{soilB}.

2.1.3 Details on the Connectors in the Assembled Land Surface Model

Since α, ε, T_{sk} and H belong to the surface sensible heat variables, but not E and z_0, only the rest connectors will be examined. We start from U_L, because its computation is the most complex and impacts other connectors.

2.1.3.1 The adjusted lowest model level wind speed

In RMM5, the lowest model level wind speed U_L is calculated as

$$U_L = \max\begin{cases}\sqrt{{u_L}^2 + {v_L}^2 + (\beta w_*)^2 + {v_{sg}}^2} \\ 0.1\end{cases}, \tag{2.21}$$

where

$$w_* = \begin{cases} \left(h_{PBL} \dfrac{g}{T_{sk}} \overline{w'\theta_v'} \right)^{\frac{1}{3}} & (land) \\ \begin{cases} c(\theta_g - \theta_L)^{\frac{1}{2}}, & \theta_g \geq \theta_L \\ 0, & \theta_g < \theta_L \end{cases} & (water) \end{cases} \tag{2.22}$$

$$\overline{w'\theta_v'} = \max \begin{cases} \overline{w'\theta'} + 0.61 \times 10^{-3} \theta_v \overline{w'q'} \\ 0 \end{cases} \tag{2.23}$$

$$\overline{w'\theta'} = \frac{H}{\rho_{aL} c_p}, \ \overline{w'q'} = \frac{E}{\rho_{aL}}, \ \rho_{aL} = \frac{p_s}{R_d T_{vL}} \tag{2.24}$$

$$v_{sg} = \max \begin{cases} 0.32 \left(\dfrac{\Delta_h}{5000} - 1 \right)^{0.33} \\ 0 \end{cases} \tag{2.25}$$

In the above, *subscript* s denotes variables at the surface, with constant $c = 2.0 m \ \ s^{-1} K^{\frac{1}{2}}$. For the remaining symbols, u and v represent wind speed; p is pressure; θ_v and θ_g are obtained per Eqs. (2.8) and (2.9) respectively; β is a constant of order 1 and sets as 1.0 in ARW-WRF3.4.1; w_* stands for the free-convection velocity scale proposed by Beljaars (1995); and v_{sg} is the sub-grid velocity consideration from Mahrt and Sun (1995), which would be effectively zero when $\Delta_h \leq 5000$ m. According to Eqs. (2.21) to (2.25), q_s is the only variable needs to be considered due to its relationship with surface temperature variables as will show next.

In module_sf_noahdrv.F[3]

$$q_s = \frac{q_1}{1-q_1} \text{ and } q_1 = \frac{r_L}{1+r_L} + \frac{c_p E_{knem}}{C_H}, \tag{2.26}$$

where E_{knem} is the kinematic moisture flux and C_H denotes exchange coefficient with wind speed incorporated (provided by RMM5). Note that, in different modules of the WRF codes, q_s is converted between specific humidity and mixing ratio for the convenience of calculating other quantities (F. Chen and M. Barlage 2013; personal communication), and in Eq. (2.26) it is mixing ratio. Apparently, Eq. (2.26) suggests that no further examinations on q_s are needed, since in most of the quasi-idealized simulations introduced later, E (such that LE) is set as zero. Yet, what is desired is that the land surface evolves physically normal, but its evaporation does not enter the atmosphere. Consequently, besides C_H, the calculation of E_{knem} still matters, because of its relationship with q_s which will be passed to RMM5 (after converting back to specific humidity) in the next time step, influencing θ_v (Eq. 2.8) and thus U_L (Eqs. 2.21 to 2.24).

The kinematic moisture flux E_{knem} in WRF-Noah is obtained per the following equations,

[3] Unless otherwise stated, any Fortran code in this dissertation is from ARW-WRF3.4.1.

$$E_{knem} = \begin{cases} E_d + E_t + E_c, & without \quad snow \\ E_{snow} + (1-\sigma_{snow})(E_d + E_c + E_t), & with \quad snow \\ E_{snow}, & glacier \quad or \quad sea \quad ice \end{cases}, \tag{2.27}$$

where

$$E_d = (1-\sigma_f)\frac{\Theta_1 - \Theta_w}{\Theta_{ref} - \Theta_w} E_p \tag{2.28}$$

$$E_t = \sigma_f E_p B_c \left[1 - \left(\frac{W_{canp}}{S} \right)^{0.5} \right] \tag{2.29}$$

$$E_c = \sigma_f E_p \left(\frac{W_{canp}}{S} \right)^{0.5} \tag{2.30}$$

$$E_{snow} = \sigma_{snow} E_p \tag{2.31}$$

$$B_c = \frac{R_r + \Delta}{(1 + R_c C_H) R_r + \Delta} \tag{2.32}$$

$$E_p = \frac{RAD \times \Delta + A \times R_r}{\Delta + R_r} \tag{2.33}$$

$$RAD = \frac{SW_{dn} + LW_{dn} - G - \varepsilon\sigma T_L^4}{\rho_{aL} c_p C_H} + (\theta_L - T_L) \tag{2.34}$$

$$\Delta = \frac{L_v}{c_p} \left(\frac{dq^*}{dT} \right)_L \tag{2.35}$$

$$A = (q_L^* - q_L) \frac{L_v}{c_p} \tag{2.36}$$

$$R_r = \frac{4\varepsilon\sigma T_L^4 R_d}{p_L c_p C_H} + 1 + \frac{P c_{pw}}{\rho_{aL} c_p C_H} \tag{2.37}$$

$$G = \frac{K_t\left(T_{sk} - T_{soil1}\right)}{D_{tot}} \text{ and } D_{tot} = D_{soil1} + D_{snow} \tag{2.38}$$

$$\frac{\partial W_{canp}}{\partial t} = \sigma_f P - D - E_c \tag{2.39}$$

$$K_t = f\left(\Theta,\ \Theta_H,\ \Theta_s,\ S_q\right) \tag{2.40}$$

$$\Theta_H = f_i\left(\Theta,\ \Theta_{ice},\ \Theta_s,\ T_{soil},\ T_{soilB},\ \psi_s,\ b\right), \tag{2.41}$$

where c_{pw} represents the specific heat for water at constant pressure, with the detailed iteration procedure for Eq. (2.41) documented in the Appendix. Since the computation of D_{snow} does not involve any variables related with surface temperature in the current formulation of Noah, Eqs. (2.27) to (2.41) suggest that T_{soil} and T_{soilB} are parts of the surface sensible heat effect, although the latter is typically set as time invariant for weather-scale simulations.

As implied by Eqs. (2.26), (2.32), (2.34) and (2.37), another variable needs to be investigated is

$$C_H = \rho_{aL} c_p \frac{\kappa u_*}{\left(\ln\frac{z_L}{z_0} - \psi_h\right)}, \tag{2.42}$$

where κ is the von Kármán constant and note that instead of dimensionless, wind speed is absorbed in C_H (Ek and Mahrt 1991). This equation suggests further investigations of u_* and ψ_h, which will be presented in section 2.1.3.3 and 2.1.3.4 respectively.

2.1.3.2 The bulk Richardson number

In RMM5, the bulk Richardson number R_B is obtained after solving the following equation iteratively

$$R_B = \frac{z_L}{L_{MO}} \frac{\ln\left(\frac{z_L + z_0}{z_0}\right) - \psi_h\left(\frac{z_L + z_0}{L_{MO}}\right) + \psi_h\left(\frac{z_0}{L_{MO}}\right)}{\left[\ln\left(\frac{z_L + z_0}{z_0}\right) - \psi_m\left(\frac{z_L + z_0}{L_{MO}}\right) + \psi_m\left(\frac{z_0}{L_{MO}}\right)\right]^2}, \tag{2.43}$$

to have R_B consistent with the stability parameter $\zeta = \frac{z_L}{L_{MO}}$ (see Figure 2 of Jiménez et al. 2012). However, the first guess of R_B before getting into the iteration procedure is determined by

$$R_B = \frac{g}{\theta_L} z_L \frac{\theta_{vL} - \theta_v}{U_L^{\,2}}. \tag{2.44}$$

Per the analysis in section 2.1.3.1, no extra surface temperature related variables are involved by Eqs. (2.43) and (2.44), besides the stability function for momentum and heat/moisture, which will be examined in the next section.

2.1.3.3 Stability function for momentum and heat/moisture

The connectors F_{ψ_m} and F_{ψ_h} in Eq. (2.1) are

$$F_{\psi_m} = \ln\frac{z_L}{z_0} - \psi_m \text{ and } F_{\psi_h} = \ln\frac{z_L}{z_0} - \psi_h, \tag{2.45}$$

which are the parameters passed from the RMM5 into the Yonsei University (YSU) boundary layer parameterization employed in this study[4]. In RMM5, the stability function is treated separately for unstable, stable and neutral conditions.

1) For unstable conditions

$$\psi_{h,m} = \frac{\psi_{Kh,m}(\zeta) + \zeta^2 \psi_{Ch,m}(\zeta)}{1+\zeta^2} \tag{2.46}$$

$$\psi_{Kh,m}(\zeta) = \begin{cases} \psi_m(\zeta) = 2\ln(\frac{x+1}{2}) + \ln(\frac{x^2+1}{2}) - 2\tan^{-1}(x) + \frac{\pi}{2}, \quad with \quad x = (1-\gamma_1\zeta)^{1/4}, \quad \gamma_1 = 16 \\ \psi_h(\zeta) = 2\ln(\frac{y+1}{2})6, \quad with \quad y = (1-\gamma_2\zeta)^{1/2} \quad and \quad \gamma_2 = 16 \end{cases}$$

(2.47)

$$\psi_{Ch,m}(\zeta) = \frac{3}{2}\ln(\frac{y^2+y+1}{3}) - \sqrt{3}\tan^{-1}(\frac{2y+1}{\sqrt{3}}) + \frac{\pi}{\sqrt{3}}, \quad with \quad y = \left[1-\alpha_{h,m}(\zeta)\right]^{1/3}, \quad \begin{cases} \alpha_m = 10 \\ \alpha_h = 34 \end{cases}, \tag{2.48}$$

---

[4] The naming convection in module_bl_ysu.F, as well as the relevant comments in the code, can cause confusions on the parameters passed to the YSU from RMM5. In this module, it appears ψ_m and ψ_h are transferred in. However, the upper-level module, i.e., module_pbl_driver.F, shows that they are the global variables grid%FM and grid%FH, which are calculated per Eq. (2.45).

where the $\psi_{Kh,m}(\zeta)$ denotes the contribution from Kansans-type function (Paulson 1970), while $\psi_{Ch,m}(\zeta)$ represents convective contribution (Fairall et al. 1996; Grachev et al. 2000). The stability parameter $\zeta = \frac{z_L}{L_{MO}}$ for unstable conditions is obtained per

$$\frac{z_L}{L_{MO}} = \begin{cases} R_B \ln\left(\frac{z + z_0}{z_0}\right), & u_* < 0.001 m/s \\ Solve \quad Eq.(2.43) \quad iteratively, & u_* \geq 0.001 m/s \end{cases} \tag{2.49}$$

2) For stable conditions

$$\psi_m = -a \ln\left[\zeta + \left(1 + \zeta^b\right)^{\frac{1}{b}}\right] \tag{2.50}$$

$$\psi_h = -c \ln\left[\zeta + \left(1 + \zeta^d\right)^{\frac{1}{d}}\right], \tag{2.51}$$

where $a = 6.1, \quad b = 2.5 \quad c = 5.3$, and $d = 1.1$, and ζ relies on the iterative solution of Eq. (2.43).

3) For neutral conditions (forced convection)

$$\zeta = 0 \text{ and } \psi_{m,h} = 0 . \tag{2.52}$$

Equations (2.45) to (2.52) suggest that no extra surface temperature related variables are needed, besides those diagnosed in earlier sections.

2.1.3.4 Frictional velocity and 10 m wind

In RMM5, the friction velocity u_* is calculated as

$$u_* = 0.5 * u_* + 0.5\kappa \frac{U_L}{\ln\left(\frac{z_L + z_0}{z_L}\right) - \psi_m\left(\frac{z_L + z_0}{L_{MO}}\right) + \psi_m\left(\frac{z_0}{L_{MO}}\right)} \tag{2.53}$$

The u_* on the RHS of Eq. (2.53) is from the previous time step to prevent oscillation, and the 10 m wind fields are obtained through

$$u_{10} = u_L \frac{\ln\left(\frac{10 + z_0}{z_0}\right) - \psi_m\left(\frac{10 + z_0}{L_{MO}}\right) + \psi_m\left(\frac{z_0}{L_{MO}}\right)}{\ln\left(\frac{z_L + z_0}{z_0}\right) - \psi_m\left(\frac{z_L + z_0}{L_{MO}}\right) + \psi_m\left(\frac{z_0}{L_{MO}}\right)} \tag{2.54}$$

$$v_{10} = v_L \frac{\ln\left(\frac{10 + z_0}{z_0}\right) - \psi_m\left(\frac{10 + z_0}{L_{MO}}\right) + \psi_m\left(\frac{z_0}{L_{MO}}\right)}{\ln\left(\frac{z_L + z_0}{z_0}\right) - \psi_m\left(\frac{z_L + z_0}{L_{MO}}\right) + \psi_m\left(\frac{z_0}{L_{MO}}\right)} \tag{2.55}$$

Clearly, no extra surface temperature variables are introduced by Eqs. (2.53), (2.54) and (2.55).

2.2 Experiments Design

2.2.1 Selected Weather Conditions

As the moisture budget along the eastern slopes of the Andes is closely related to SALLJ, two simulations were conducted for events during the SALLJ Experiment (SALLJEX, Nov. 15, 2002 to Feb. 15 2003; Vera et al. 2005) to take the advantage of existing observations. The first simulation is for a weak LLJ event (WLLJ, Jan. 15, 2003) and the second is for a strong one (SLLJ, Feb. 6, 2003). In the former, the Bolivian high

(BH), potentially influential to cloud formation and precipitation over the high Andes (Garreaud 1999), is more prominent (cf. Figures 2.1a and 2.1b). The Chaco low (~25°S) is present in the latter (Figure 2.1g), resembling the typical circulation features accompanied by intense low level jets described by Salio et al. (2002). These two simulations represent atmospheric conditions that are observed frequently during the monsoon season.

Table 2.1: Events description

Experiment	Simulation period (UTC, D02 and D03)	Synoptic conditions
WLLJ	0000 Jan 15 - 1200 Jan 16, 2003	Weak LLJ and prominent Bolivian high
SLLJ	0000 Feb 6 - 1200 Feb 7, 2003	Strong LLJ and debilitated Bolivian high
NDRY	0000 Jun 28 - 1200 Jun 29, 2003	Typical dry conditions in the austral winter
CDRY	0000 Aug 9 - 1200 Aug 10, 2003	Cold surge
EDRY	0000 Jul 20 - 1200 Jul 21, 2003	Rainless over the EADS

Another three experiments were carried out in the dry season: a precipitation event with accumulations around the climatological mean (NDRY, Jun. 28, 2003); a relatively wet day in the winter (CDRY, Aug. 9, 2003); and an extremely dry case (EDRY, Jul. 20, 2003). In these three dry season simulations, characteristic conditions of the austral winter in South America occur, including the absence of the BH (Figures 2.1c to 2.1e) associated with suppressed latent heating in the Amazon (Lenters and Cook 1997, their Figure 1), and moist air masses that mainly originate from the subtropical Atlantic high (Figures 2.1h to 2.1j), rather than from the tropical Atlantic as in the wet season

(Figures 2.1f and 2.1g) (Rao et al. 1996). Specifically for CDRY, the anticyclone centered around 35˚S, as well as the southerly low level flows to the east of the Andes (Figure 2.1i), suggest the intrusion of Southern Hemisphere middle latitude systems into the subtropics and tropics (i.e., the so-called cold surge; see also Figures 4b, 5b and 10 in Garreaud 2000b). These five cases thus cover a wide range of weather conditions prevalent in South America. A summary description is provided in Table 2.1.

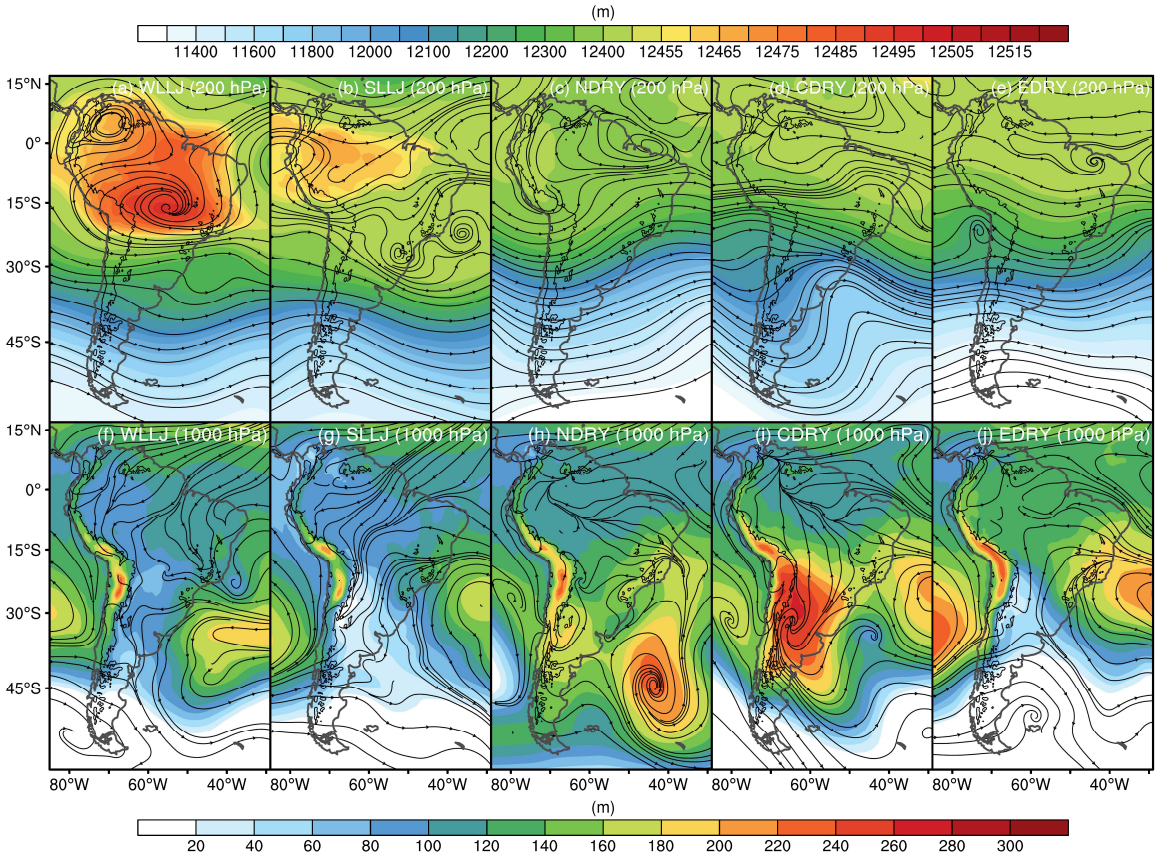

Figure 2.1: Geopotential height (m, shaded) and streamlines (dark gray) at 200 (top) and 1000 (bottom) hPa from the NCEP-FNL for the WLLJ, SLLJ, NDRY, CDRY and EDRY as indicated in the panel titles. The black contours represent 1000 m topography.

2.2.2 The WRFCTL Simulations

Using ARW-WRF3.4.1 and focusing on the central Andes in Peru, the simulations were implemented on three nests (316 × 496, 433 × 604 and 756 × 726 grid cells) at 18, 6 and 1.2 km grid spacing (Figure 2.2), with the initial and lateral boundary conditions derived from the Final Operational Global Analysis produced by the National Centers for Environmental Prediction (NCEP-FNL). In the vertical direction, each grid consists of 60 sigma levels, and nearly 14 layers are within the lowest 1 km. The physics options applied are the Dudhia shortwave, RRTM longwave (Rapid Radiative Transfer Model), Lin et al. microphysics, Kain-Fritsch cumulus parameterization (for the two outer domains only), Yonsei University (YSU) boundary layer, revised MM5 surface layer and Noah land surface (Skamarock et al. 2008, and references therein). One-way nesting was employed.

The outermost grid was initialized one day earlier than the period of interest at 0600 UTC (around midnight in the Andes) to provide lateral boundary conditions more consistent with model physics. For the two inner domains, the model ran for 36 hours from 0000 UTC on the same day of each case, with the first six hours model integration deemed as the spin-up of the atmosphere (e.g., Sun and Barros 2012). The land surface conditions were initialized using the National Center for Atmospheric Research (NCAR) High-Resolution Land Data Assimilation System (HRLDAS; Chen et al. 2007), forced by

the product from the Global Land Data Assimilation System (GLDAS; Rodell et al. 2004). HRLDAS was run on the same grid as the ARW-WRF3.4.1 simulations with five cycles (each cycle lasts for one year) for a sufficient spin-up of soil moisture, one of the fundamental variables determining surface evapotranspiration.

These simulations are called WRFCTL, with each case labeled as WLLJ_CTL, SLLJ_CTL, NDRY_CTL, CDRY_CTL and EDRY_CTL respectively.

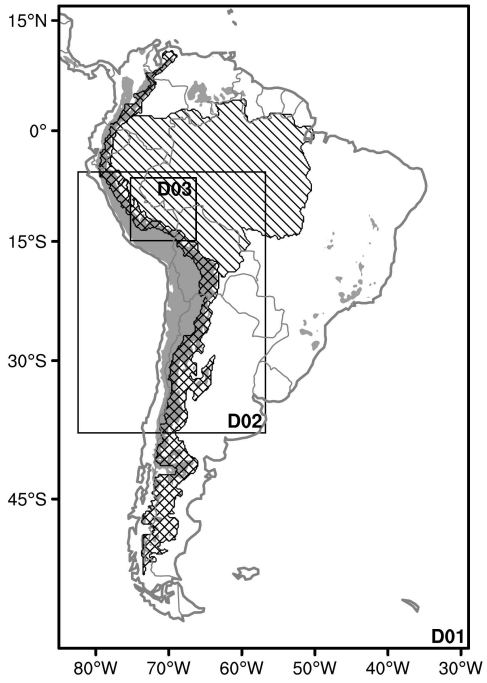

Figure 2.2: Simulation nests at 18 (D01), 6 (D02) and 1.2 (D03) km grid spacing, with areas higher than 1000 m shaded in dark gray. The black mesh denotes the eastern flanks of the Andes (EADS), while the hatched region is the Amazon lowlands (AMZL).

2.2.3 The STRICT Experiments

To isolate the role of surface evapotranspiration (ET), quasi-idealized experiments were conducted, where at *each time step* the surface sensible heat variables, including α, ε, T_{sk}, H, T_{soil} and T_{soilB}, were imposed exactly the same as in the WRFCTL runs, but with E, such that LE, specified as zero when they represent a source to the atmosphere. In this dissertation, they are referred as STRICT experiments in the sense that the surface sensible heat effects are strictly identical to their WRFCTL counterparts.

To understand the local influences of surface ET, the manipulations described above were applied along the eastern flanks of the Andes (EADS), approximated as the elevation band between 500 and 3500 m and for the eastern side only (Figure 2.2). These experiments are named as WLLJ_ADS, SLLJ_ADS, NDRY_ADS, CDRY_ADS and EDRY_ADS, respectively.

The other group of simulations is the same as the first one, but with surface ET removed over the Amazon lowlands (AMZL). The AMZL refers to the Amazonian region with elevation lower than 500 m (Figure 2.2). The objective of these simulations is to understand the role of Amazonian ET on the evolution of atmospheric circulations over South America, with a special emphasis toward moisture transport and convection

along the EADS. They are labeled as WLLJ_AMZ, SLLJ_AMZ, NDRY_AMZ, CDRY_AMZ and EDRY_AMZ, respectively.

As the second group of simulations suggests significant influences toward the EADS by the remote surface ET over the AMZL, another group of simulations at 18 km grid increment were conducted to examine the robustness of this relationship. Preferring rainfall as a simple measure, the WLLJ was selected, because the EADS rainfall in the WLLJ_AMZ increases in the day, but decreases at night as compared with the WLLJ_CTL. These set of experiments are configured the same as the STRICT simulations, except that, instead of removing surface ET over the AMZL, it is modified from negative to positive 100 percent anomalies at every 20 percent intervals.

2.3 Modifications of ARW-WRF3.4.1

As shown in Figure 2.2, the EADS and AMZL are irregular. The former was built upon the topography generated by the WRF Preprocessing System (WPS), while the latter was based on the Amazon border obtained from HYBAM (http://www.ore-hybam.org/index.php/eng/Data/Cartography/Amazon-basin-hydrography). The created masks were included in the WPS-met data, with the WRF registry (Registry.EM_COMMON) modified correspondingly. As a consequence, not only the real program of ARW-WRF3.4.1 can handle them automatically, avoiding issues of

directly changing relevant parallel reading and writing subroutines, these masks also become available to the WRF codes, allowing run-time geographical positioning.

The time-step imposition of surface sensible heat variables were accomplished using auxiliary data stream technique. However, the time step for simulations at 1.2 km grid spacing requires sub-second time step (down to 0.2 s), whereas the "time clock" of ARW-WRF3.4.1 controlling auxiliary input/output cannot be less than one second. To implement sub-second imposition, i.e., artificially forcing the surface sensible heat effects exactly the same as in the WRFCTL runs at every time step, substantial modifications of the WRF codes are indispensable. This is because the most relevant changes are at very low-levels of ARW-WRF3.4.1 from the software structure point of view. In details, the modifications involve 22 Fortran, C and head files[5],

1) convert_em.F

2) dfi.F

3) ext_ncd_get_var_td.code

4) ext_ncd_put_var_td.code

5) gen_streams.c

6) gen_wrf_io.c

7) ideal_em.F

[5] In ARW-WRF3.4.1, some head files are required to generate source codes automatically.

8) input_wrf.F

9) mediation_integrate.F

10) module_integrate.F

11) module_io_domain.F

12) module_io.F

13) ndown_em.F

14) nup_em.F

15) output_wrf.F

16) real_em.F

17) tc_em.F

18) wrf_bdyin.F

19) wrf_bdyout.F

20) wrf_ext_read_field.F

21) wrf_ext_write_field.F

22) wrf_io.F90

The modified ARW-WRF3.4.1 was thoroughly tested thereafter and proved operating as desired.

3 Methodology

3.1 Hydrostatic Surface Pressure Tendency

For an air column of unit area,

$$\tilde{m} = \int_0^{z_{top}} \rho_a dz\,,\ \tilde{m}_d = \int_0^{z_{top}} \rho_a (1-q) dz\,,\ \tilde{m}_v = \int_0^{z_{top}} \rho_a q dz\,,\ \tilde{m}_e = \int_0^{z_{top}} \rho_a e dz\,,\ \tilde{m}_c = \int_0^{z_{top}} \rho_a c dz\,,$$

where e (c) is evaporation (condensation) per unit mass in kg kg^{-1}; $\tilde{m}$, $\tilde{m}_d$, $\tilde{m}_v$, $\tilde{m}_e$ and $\tilde{m}_c$ are the column integrated mass of air, dry air, water vapor, evaporation and condensate respectively. As $\tilde{m}_d$ is conserved, but not $\tilde{m}_v$,

$$\frac{\partial \tilde{m}_d}{\partial t} + \nabla \cdot \int_0^{z_{top}} \rho_a (1-q)\mathbf{v} dz = 0 \tag{3.1}$$

$$\frac{\partial \tilde{m}_v}{\partial t} + \nabla \cdot \int_0^{z_{top}} \rho_a q\mathbf{v} dz = \frac{\partial \tilde{m}_e}{\partial t} - \frac{\partial \tilde{m}_c}{\partial t}\,, \tag{3.2}$$

where $\mathbf{v}$ represents the velocity vector. Under hydrostatic balance,

$$\frac{\partial p_s}{\partial t} = g\left(\frac{\partial \tilde{m}_d}{\partial t} + \frac{\partial \tilde{m}_v}{\partial t} \right). \tag{3.3}$$

Substitute Eqs. (3.1) and (3.2) into (3.3) and given that the vertical velocity vanishes at the top of the atmosphere and the land surface, as well as the fact that $\frac{\partial \tilde{m}_e}{\partial t} - \frac{\partial \tilde{m}_c}{\partial t} = \rho_l (E - P)$,

$$\frac{\partial p_s}{\partial t} = -g\nabla \cdot \int_0^{z_{top}} \rho_a \mathbf{v}_\mathbf{H} dz + g\rho_l E - g\rho_l P\,. \tag{3.4}$$

When applies to a limited region, Eq. (3.4) becomes

$$\frac{\partial \overline{p_s}}{\partial t} = -g\nabla \cdot \int_0^{z_{top}} \rho_a \mathbf{v_H} dz + g\rho_l \overline{E} - g\rho_l \overline{P}, \quad (3.5)$$

where p_s is the hydrostatic surface pressure, $\mathbf{v_H}$ represents the horizontal component of the total velocity vector and ρ_l is the density of liquid water, with the integration spanning from the land surface to the top of the atmosphere (z_{top}). The overbar in Eq. (3.5) indicates average over a specified region (e.g., the EADS). For heavily precipitating systems (e.g., tropical cyclones), Lackmann and Yablonsky (2004) demonstrated that the component associated with precipitation $-g\rho_l P$ is not negligible [up to -1.56 hPa h^{-1} for Hurricane Lili (2002)], though not dominant. In this study, each term of Eq. (3.5) was evaluated to examine the magnitude of the mass removed by turning off surface ET.

3.2 Moisture Budget

The moisture budget equation can be written as

$$\frac{\partial W}{\partial t} + P = E - \nabla \cdot \frac{1}{g} \int_0^{p_s} q\mathbf{v_H} dp, \quad (3.6)$$

where $W = \frac{1}{g} \int_0^{p_s} q dp$ represents precipitable water vapor (e.g., Trenberth and Guillemot 1995). At time scales greater than 10 days, the column moisture convergence nearly balances the difference between precipitation and surface evaporation (e.g., Li et al. 2013), indicating only a small fraction of the large-scale forcing of water vapor can be absorbed by the atmospheric water vapor storage (Emanuel 1994). At shorter time

scales, $\frac{\partial W}{\partial t}$ is non-negligible and could be influential to environmental dynamics and thermodynamics, as well as microphysics.

3.3 Apparent Heat Source and Apparent Moisture Sink in σ-coordinates

The results discussed later in Chapter 5 suggest that convection over the EADS can be dramatically suppressed in the STRICT experiments. To quantify the relevant impacts to the atmospheric environment, the apparent heat source Q_1 and apparent moisture sink Q_2 (Yanai et al. 1973; Nitta 1977) are examined. Ignoring eddy horizontal transport terms, these two measures can be obtained from mass continuity, heat energy and moisture continuity equations,

$$Q_1 \equiv c_p\left(\frac{p}{p_0}\right)^{\frac{R}{c_p}}\left(\frac{\partial \overline{\theta}}{\partial t}+\overline{\mathbf{v_H}\cdot\nabla\theta}+\overline{\omega}\frac{\partial \overline{\theta}}{\partial p}\right)=Q_R+Q_L-\frac{\partial \overline{\theta'\omega'}}{\partial p} \tag{3.7}$$

$$Q_2 \equiv -L_v\left(\frac{\partial \overline{q}}{\partial t}+\overline{\mathbf{v_H}\cdot\nabla q}+\overline{\omega}\frac{\partial \overline{q}}{\partial p}\right)=Q_L+L_v\frac{\partial \overline{q'\omega'}}{\partial p}, \tag{3.8}$$

where L_v is the latent heat of vaporization, ω is the vertical velocity in pressure-coordinate, Q_R represents radiative heating and Q_L denotes latent heating. The overbar indicates spatial average over an area sufficiently large to contain ensembles of clouds, but small enough to be regarded as a fraction of the large-scale system, and the prime indicates deviations from the horizontal average. Because (Q_1-Q_R) and Q_2 would be

zero if there were no convective clouds, any non-zero values may be attributed to convection (Emanuel 1994), except in the subcloud layer where turbulent mixing can be dominant. The "apparent" literally means besides true sources and sinks, the unresolved eddy fluxes are also accounted for (Yanai and Johnson 1993).

According to Kasahara (1974),

$$\left(\frac{\partial A}{\partial t}\right)_p = \left(\frac{\partial A}{\partial t}\right)_\sigma - \frac{\partial \sigma}{\partial p}\left(\frac{\partial p}{\partial t}\right)_\sigma \frac{\partial A}{\partial \sigma} \tag{3.9}$$

$$\nabla_p A = \nabla_\sigma A - \frac{\partial \sigma}{\partial p}(\nabla_\sigma p)\frac{\partial A}{\partial \sigma}, \tag{3.10}$$

where A can be any scalar functions and the subscript p and σ indicate a particular vertical coordinate to be held constant for partial differentiations. Thus,

$$\left(\frac{\partial \bar{q}}{\partial t}\right)_p = \left(\frac{\partial \bar{q}}{\partial t}\right)_\sigma - \frac{\partial \sigma}{\partial p}\left(\frac{\partial p}{\partial t}\right)_\sigma \frac{\partial \bar{q}}{\partial \sigma} \tag{3.11}$$

$$\left(\frac{\partial \bar{\theta}}{\partial t}\right)_p = \left(\frac{\partial \bar{\theta}}{\partial t}\right)_\sigma - \frac{\partial \sigma}{\partial p}\left(\frac{\partial p}{\partial t}\right)_\sigma \frac{\partial \bar{\theta}}{\partial \sigma} \tag{3.12}$$

$$\overline{(\mathbf{v_H}\cdot\nabla q)}_p = \overline{\mathbf{v_H}\cdot\nabla_\sigma q} - \overline{\mathbf{v_H}\cdot\left[\frac{\partial \sigma}{\partial p}(\nabla_\sigma p)\frac{\partial q}{\partial \sigma}\right]} \tag{3.13}$$

$$\overline{(\mathbf{v_H}\cdot\nabla \theta)}_p = \overline{\mathbf{v_H}\cdot\nabla_\sigma \theta} - \overline{\mathbf{v_H}\cdot\left[\frac{\partial \sigma}{\partial p}(\nabla_\sigma p)\frac{\partial \theta}{\partial \sigma}\right]}. \tag{3.14}$$

Divided by c_p to be converted into temperature tendency and using the relationship $\frac{\partial A}{\partial p} = \frac{\partial A}{\partial \sigma}\frac{\partial \sigma}{\partial p}$, Q_1 and Q_2 in σ-coordinates can be obtained after substituting Eqs. (3.11) to (3.14) into Eqs. (3.7) and (3.8),

$$Q_1 \equiv \left(\frac{p}{p_0}\right)^{\frac{R}{c_p}} \left\{ \left(\frac{\partial \bar{\theta}}{\partial t}\right)_\sigma + \overline{\mathbf{v_H} \cdot \nabla_\sigma \theta} + \frac{\partial \sigma}{\partial p}\left[\bar{\omega} - \left(\frac{\partial p}{\partial t}\right)_\sigma\right]\frac{\partial \bar{\theta}}{\partial \sigma} - \overline{\mathbf{v_H} \cdot \left[\frac{\partial \sigma}{\partial p}\left(\nabla_\sigma p\right)\frac{\partial \theta}{\partial \sigma}\right]} \right\} \quad (3.15)$$

$$Q_2 \equiv -\frac{L_v}{c_p}\left\{ \left(\frac{\partial \bar{q}}{\partial t}\right)_\sigma + \overline{\mathbf{v_H} \cdot \nabla_\sigma q} + \frac{\partial \sigma}{\partial p}\left[\bar{\omega} - \left(\frac{\partial p}{\partial t}\right)_\sigma\right]\frac{\partial \bar{q}}{\partial \sigma} - \overline{\mathbf{v_H} \cdot \left[\frac{\partial \sigma}{\partial p}\left(\nabla_\sigma p\right)\frac{\partial q}{\partial \sigma}\right]} \right\}, \quad (3.16)$$

in which $\bar{\omega} \approx -g\overline{\rho_a w}$ (w is the vertical velocity in m s^{-1}) and the subscript σ indicates partial differentiations with respect to σ. Vertical eddy fluxes of sensible (FC_H), latent (FC_{LE}) and total (FC) heat can be defined as

$$FC_H = -\frac{c_p}{g}\overline{\theta'\omega'} = \frac{c_p}{g}\int_{p_{top}}^{p}\left(Q_1 - Q_R - Q_L\right)dp \quad (3.17)$$

$$FC_{LE} = -\frac{c_p}{g}L_v\overline{q'\omega'} = \frac{c_p}{g}\int_{p_{top}}^{p}\left(Q_L - Q_2\right)dp \quad (3.18)$$

$$FC = -\frac{c_p}{g}\left(\overline{\theta'\omega'} + L_v\overline{q'\omega'}\right) = \frac{c_p}{g}\int_{p_{top}}^{p}\left(Q_1 - Q_2 - Q_R\right)dp, \quad (3.19)$$

where p_{top} denotes the top of the atmosphere. The integral term $\int_{p_{top}}^{p} dp$ represents the *required* vertical eddy flux at level p to close the energy balance (see also Thompson et al. 1979).

3.4 Temperature Tendency over Irregular Areas

The first law of thermodynamics is given as follows (Holton 2004)

$$c_p \frac{DT}{Dt} - \alpha \frac{Dp}{Dt} = J \,. \tag{3.20}$$

Using the explicit form of substantial derivative in pressure coordinate

$$\frac{DT}{Dt} = \frac{\partial T}{\partial t} + \mathbf{v_H} \cdot \nabla T + \omega \frac{\partial T}{\partial p}, \tag{3.21}$$

the continuity equation

$$\nabla \cdot \mathbf{v_H} + \frac{\partial \omega}{\partial p} = 0, \tag{3.22}$$

and the identity

$$\nabla \cdot \left(T\mathbf{v_H} \right) = \mathbf{v_H} \cdot \nabla T + T \nabla \cdot \mathbf{v_H}, \tag{3.23}$$

Eq. (3.20) becomes,

$$\frac{\partial T}{\partial t} + \nabla \cdot \left(T\mathbf{v_H} \right) + \frac{\partial \omega T}{\partial p} - \frac{\alpha}{c_p} \frac{Dp}{Dt} = \frac{J}{c_p} \tag{3.24}$$

Vertically integrated (mass-weighted) over a layer bounded by p_B and p_T, it becomes

$$\int_{p_T}^{p_B} \frac{\partial T}{\partial t} dp + \int_{p_T}^{p_B} \nabla \cdot T\mathbf{v_H} dp + \int_{p_T}^{p_B} \frac{\partial \omega T}{\partial p} dp - \int_{p_T}^{p_B} \frac{\alpha}{c_p} \frac{Dp}{Dt} dp = \int_{p_T}^{p_B} \frac{J}{c_p} dp \,. \tag{3.25}$$

Since the Leibniz rule dictates that

$$\frac{\partial}{\partial t} \int_{p_T}^{p_B} T dp = \int_{p_T}^{p_B} \frac{\partial T}{\partial t} dp + T_B \frac{\partial p_B}{\partial t} - T_T \frac{\partial p_T}{\partial t} \tag{3.26}$$

$$\nabla \cdot \int_{p_T}^{p_B} T\mathbf{v_H} dp = \int_{p_T}^{p_B} \nabla \cdot T\mathbf{v_H} dp + T_B \mathbf{v}_{\mathbf{H}B} \cdot \nabla p_B - T_T \mathbf{v}_{\mathbf{H}T} \cdot \nabla p_T \tag{3.27}$$

$$\begin{aligned} &\int_{p_T}^{p_B} \frac{\partial \omega T}{\partial p} dp = \omega_B T_B - \omega_T T_T \\ &= T_B \left(\frac{\partial p_B}{\partial t} + \mathbf{v}_{\mathbf{H}B} \cdot \nabla p_B - \rho_B g w_B \right) - T_T \left(\frac{\partial p_T}{\partial t} + \mathbf{v}_{\mathbf{H}T} \cdot \nabla p_T - \rho_T g w_T \right) \end{aligned}, \tag{3.28}$$

in which hydrostatic assumption is applied and ω represents the vertical velocity in pressure-coordinate. Equation (3.29) can be obtained after substituting Eqs. (3.26) to (3.28) into Eq. (3.25),

$$\frac{\partial}{\partial t} \int_{p_T}^{p_B} T dp = -\nabla \cdot \int_{p_T}^{p_B} T\mathbf{v_H} dp - g\left(\rho_T T_T w_T - \rho_B T_B w_B\right) + \int_{p_T}^{p_B} \frac{\alpha}{c_p} \frac{Dp}{Dt} dp + \int_{p_T}^{p_B} \frac{J}{c_p} dp \,, \tag{3.29}$$

in which subscript B (T) denotes variables at the lower (upper) boundary, with g as the acceleration of gravity and c_p as the specific heat of air at constant pressure. For the remaining symbols, t is time; T is temperature; p is pressure; ρ is air density; $\mathbf{v_H}$ represents the horizontal component of the total velocity vector; w is vertical velocity; α is specific volume; and J stands for diabatic heating in J kg^{-1} s^{-1}. For a specified region, denoting $\int_{p_T}^{p_B} T\mathbf{v_H} dp = \mathbf{T}$ and using the Green's theorem

$$\iint \left(\nabla \cdot \int_{p_T}^{p_B} T\mathbf{v_H} dp \right) dA = \iint (\nabla \cdot \mathbf{T}) dA = \oint \mathbf{T}_n dl \,, \tag{3.30}$$

where dA represents the area element, dl is the line element along the lateral boundary and $\mathbf{T}_n$ is the normal component of $\mathbf{T}$ to dl. This relationship facilitates the calculation

of horizontal divergence over irregular regions, as the LHS of Eq. (3.30) is numerically convenient to acquire.

As will show in Chapter 6, atmospheric circulations over the Amazon lowlands adjust dramatically after the removal of surface ET. To understand the dominant forcing for this change, each term in Eq. (3.29) was evaluated. In the WRF model, $\frac{J}{c_p} = Q_{MP} + Q_{CU} + Q_{BL} + Q_R$, with Q_{MP}, Q_{CU}, Q_{BL} and Q_R representing heating from microphysics, cumulus, boundary layer and radiation parameterizations, respectively. Since $\frac{\partial}{\partial t}\int_{p_T}^{p_B} T dp$ can be directly diagnosed from model output, the adiabatic contribution $\int_{p_T}^{p_B} \frac{\alpha}{c_p}\frac{Dp}{Dt} dp$ to temperature tendency can be obtained as the residual of other terms. To have a unit as K s^{-1}, besides these two terms, the contribution from horizontal convergence $-\nabla \cdot \int_{p_T}^{p_B} T\mathbf{v_H} dp$, vertical divergence $-g\left(\rho_T T_T w_T - \rho_B T_B w_B\right)$ and diabatic processes $\int_{p_T}^{p_B} \frac{J}{c_p} dp$ need to be divided by layer depth.

3.5 Column Integrated Moist Static Energy Equation

The moist static energy (h) equation can be written as (Neelin and Held 1987)

$$\frac{\partial h}{\partial t} + \nabla \cdot h\mathbf{v_H} + \frac{\partial h\omega}{\partial p} = g\frac{\partial F}{\partial p}, \tag{3.31}$$

in which $F = F^R + F^s + F^L$, with F^R, F^s and F^L as the upward directed vertical fluxes due to radiation of sensible heat, diffusion of sensible heat and diffusion of latent heat, respectively. Vertically integrated (mass-weighted) over a layer bounded by p_B and p_T, it becomes

$$\frac{1}{g}\int_{p_T}^{p_B}\frac{\partial h}{\partial t}dp + \frac{1}{g}\int_{p_T}^{p_B}\nabla \cdot h\mathbf{v_H}dp + \frac{1}{g}\int_{p_T}^{p_B}\frac{\partial h\omega}{\partial p}dp = F_B - F_T. \tag{3.32}$$

Processing the LHS of Eq. (3.32) with the same approach as in Section 3.4, as well as the fact that

$$F_B - F_T = \frac{c_p}{g}\int_{p_T}^{p_B} Q_R dp + \left(F_B{}^S - F_T{}^S + F_B{}^L - F_T{}^L\right), \tag{3.33}$$

Eq. (3.32) becomes

$$\begin{aligned}&\frac{1}{g}\frac{\partial}{\partial t}\int_{p_T}^{p_B} h dp + \nabla \cdot \frac{1}{g}\int_{p_T}^{p_B} h\mathbf{v_H}dp + \left(\rho_T h_T w_T - \rho_B h_B w_B\right)\\ &= \frac{c_p}{g}\int_{p_T}^{p_B} Q_R dp + \left(F_B{}^S - F_T{}^S + F_B{}^L - F_T{}^L\right)\end{aligned}. \tag{3.34}$$

When the atmospheric layer incorporates the entire air column, thus $p_B = p_s$, $p_T = 0$, $w_B = w_s = 0$, $w_T = 0$ and $F_B - F_T = \frac{c_p}{g}\int_0^{p_s} Q_R dp + H + LE$, this equation reduces to Eq. (3.35), where the second term on its LHS bears the same

convenience for the computation over irregular regions as illustrated in Eq. (3.30).

$$\frac{1}{g}\frac{\partial}{\partial t}\int_0^{p_s} h dp + \nabla \cdot \frac{1}{g}\int_0^{p_s} h\mathbf{v_H} dp = \frac{c_p}{g}\int_0^{p_s} Q_R dp + H + LE\,, \tag{3.35}$$

where subscript s denotes variables at the land surface and H (LE) represents surface sensible (latent) heat flux.

4 Evaluation of Model Performance

In the outermost grid (Figure 4.1), the simulated precipitation from the WRFCTL experiments compares reasonably well with the Tropical Rainfall Measuring Mission (TRMM) product (3B42 Version 7, Huffman et al. 2007), including orographic precipitation along the EADS, tropical mesoscale convective systems (MCSs) in the Amazon, footprints of the Southern Hemisphere storm tracks, as well as the South Atlantic (SACZ) and inter-tropical (ITCZ) convergence zones.

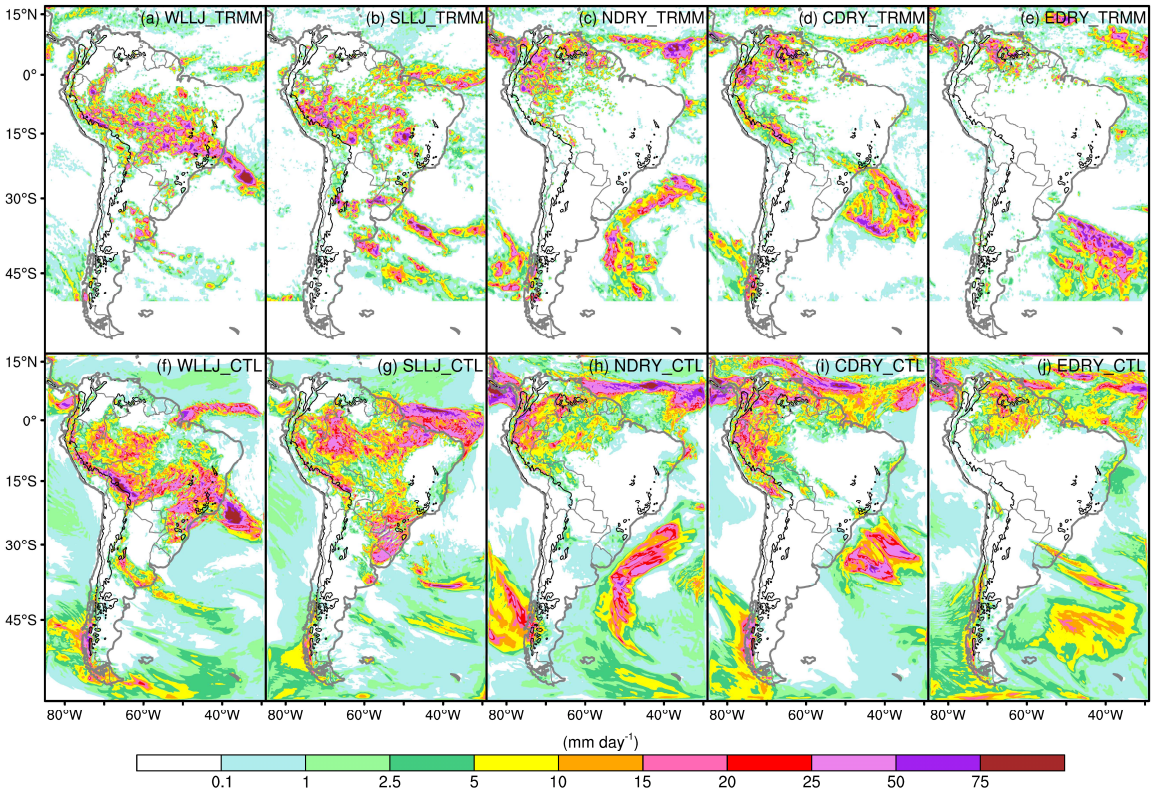

Figure 4.1: Daily precipitation (mm day^{-1}) from TRMM-3B42 (top) and WRFCTL simulations (bottom) as indicated in the panel titles. The black contours represent the 1000 m topography. They are from the outermost grid (Δ_h = 18 km).

The consistency of simulated precipitation patterns with the TRMM-3B42 rainfall product persists in the intermediate domain at 6 km grid spacing (Figure 4.2), with a weak low level jet near Santa Cruz de la Sierra, Bolivia reproduced in the WLLJ_CTL, and a much stronger one in the SLLJ_CTL (cf. Figures 4.3a and 4.3b). This contrast on the strength of low level jet is in agreement with the SALLJEX observations as detailed in Vera et al. (2006, their Figure 5). Also, the cold surge is well simulated in CDRY_CTL as manifested by the southerly low level flows to the east of the Andes (cf. Figures 4.3d and 2.1i). Apparently, precipitation magnitude is in general overestimated in terms of TRMM rainfall, and a comparison of TRMM-3B42 and TRMM PR (precipitation radar) 2A25 products shows that they are in close agreement for the dates of the simulations (not shown). However, the TRMM PR algorithm tends to underestimate precipitation associated with various storm types in South America, leading to negative biases ~40% for deep convective systems, ~25% for wide convective cores and ~15% for broad stratiform regions (Rasmussen et al. 2013). As detailed in Romatschke and Houze (2010), the latter two are prevalent over the Amazon in the wet season.

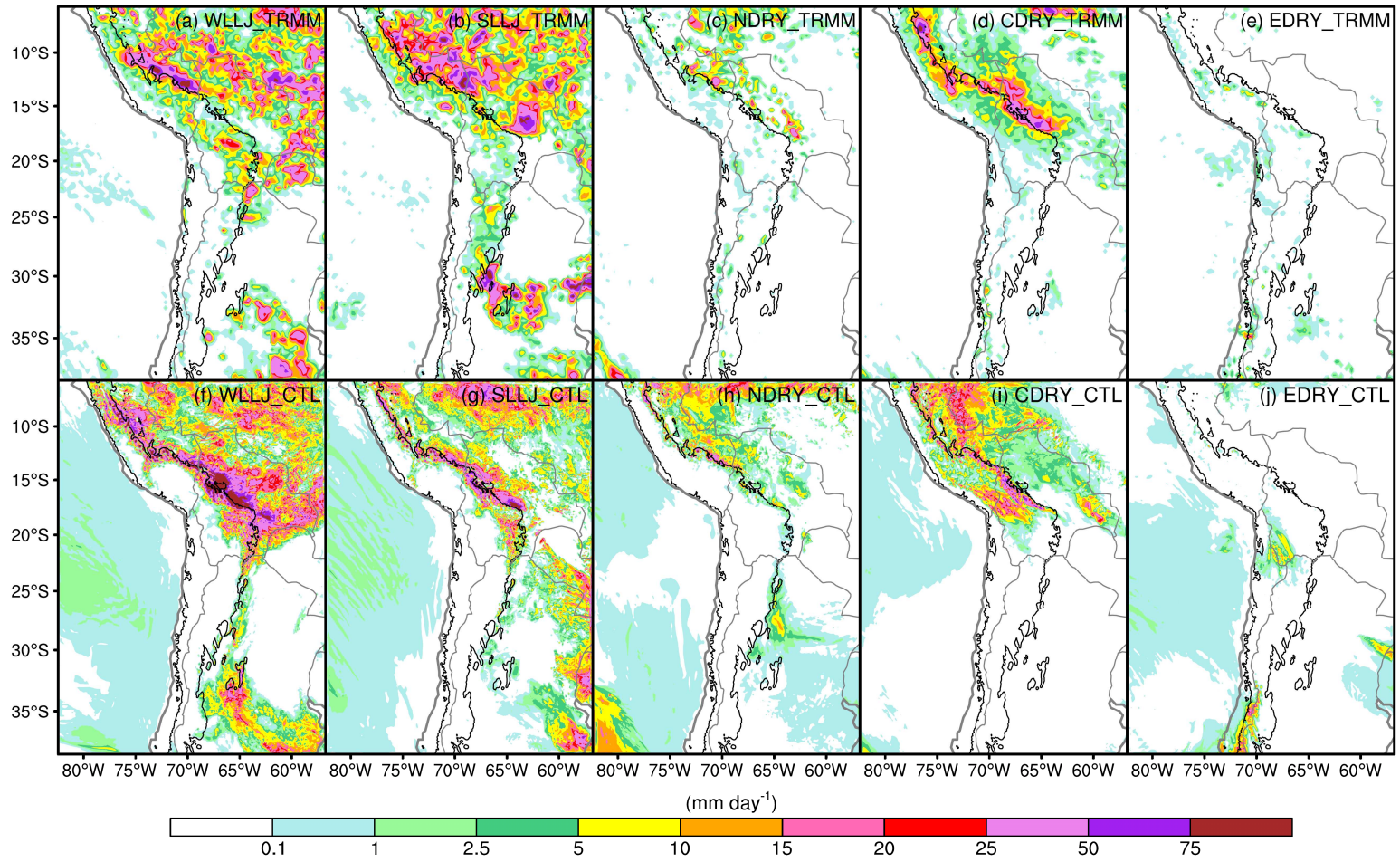

Figure 4.2: The same as Figure 4.1, but from the intermediate domain (Δ_h = 6 km).

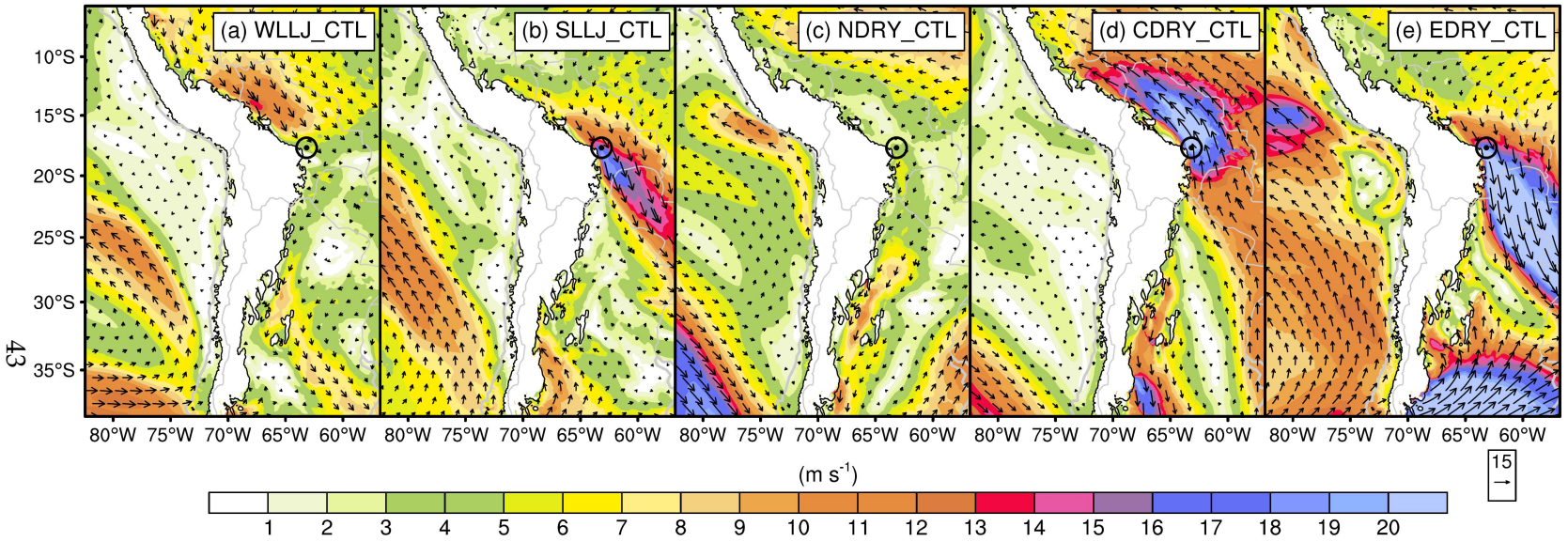

Figure 4.3: Horizontal wind speed (m s^{-1}) at 1250 m from WRFCTL simulations as indicated in the panel titles, with the black circle denoting Santa Cruz de la Sierra, Bolivia, where the strongest SALLJ is typically observed. The black contours represent the 1000 m topography. They are daily averaged and from the intermediate grid (Δ_h = 6 km).

Within the innermost nest, the ARW-WRF3.4.1 appears to overestimate precipitation (Figure 4.4) along the EADS and at higher elevations compared to TRMM-3B42. Yet, underestimation of orographic precipitation by remote-sensing retrieval algorithms in mountainous regions is well established (e.g., Barros et al. 2000). An evaluation of a recent network of raingauges up to 4000 m elevation against TRMM precipitation features (Liu et al. 2008) in the Central Andes suggests that the TRMM 3B42 product underestimates precipitation by as much as ~300-400% during the wet season (Lowman and Barros 2014). Indeed, deep convection over the Andes in Peru and Bolivia was observed by the Geostationary Operational Environmental Satellite (GOES, available online at http://www.goes.noaa.gov), as shown by the persistent low cloud-top temperature in Figures 4.5. Along the foothills and over the adjacent lowlands in the Amazon, the model strongly underestimates precipitation, especially for the WLLJ and SLLJ cases. In part, this may be attributed to the fact that explicit simulations at 1.2 km grid increment may not be sufficient to capture tropical MCSs, in which mass fluxes and mesoscale self-organization are relatively weaker compared to other weather systems, e.g., tropical cyclones (Hong and Dudhia 2012; Sun and Barros 2012, 2013). Since rainfall underestimation also occurs in the west Amazon around the border between Peru and Brazil in the two outer domains (Figures 4.1f, 4.1g, 4.2f and 4.2g), limitations of model physics can be another source of under-predicted precipitation, although other physics

options were examined and could not improve model performance (not shown). On the other hand, the 0.25 degree TRMM-3B42 itself may not be reliable at low elevations in this region, because the 14 SALLJEX daily raingauge measurements during the WLLJ and SLLJ events report much lower precipitation, with a maximum merely up to 15.5 mm day^{-1} and less than 11 mm day^{-1} over the Amazon proper (Figure 4.6 and Table 4.1). Thus, the precipitation simulated in the ARW-WRF3.4.1 may not be as insufficient as an inspection of Figures 4.4a (4.4b) and 4.4f (4.4g) may suggest.

Table 4.1: SALLJEX raingauge measurements in Figure 4.6.

Event	Latitude (°)	Longitude (°)	Elevation (m)	Rain (mm day^{-1})
WLLJ	-6.67	-69.87	131.39	4.1
	-8.17	-70.77	190.16	6.1
	-12.63	-69.20	194.51	6.1
	-14.30	-67.37	282.58	2.0
	-14.48	-67.48	388.29	15.5
	-14.73	-68.42	1993.59	1.0
	-14.87	-66.75	289.22	2.8
SLLJ	-7.63	-72.67	187.91	10.9
	-8.17	-70.77	190.16	0.3
	-10.00	-67.80	154.19	0.3
	-11.08	-68.87	289.52	4.6
	-14.30	-67.37	282.58	2.0
	-14.48	-67.48	388.29	9.9
	-14.87	-66.75	289.22	4.3

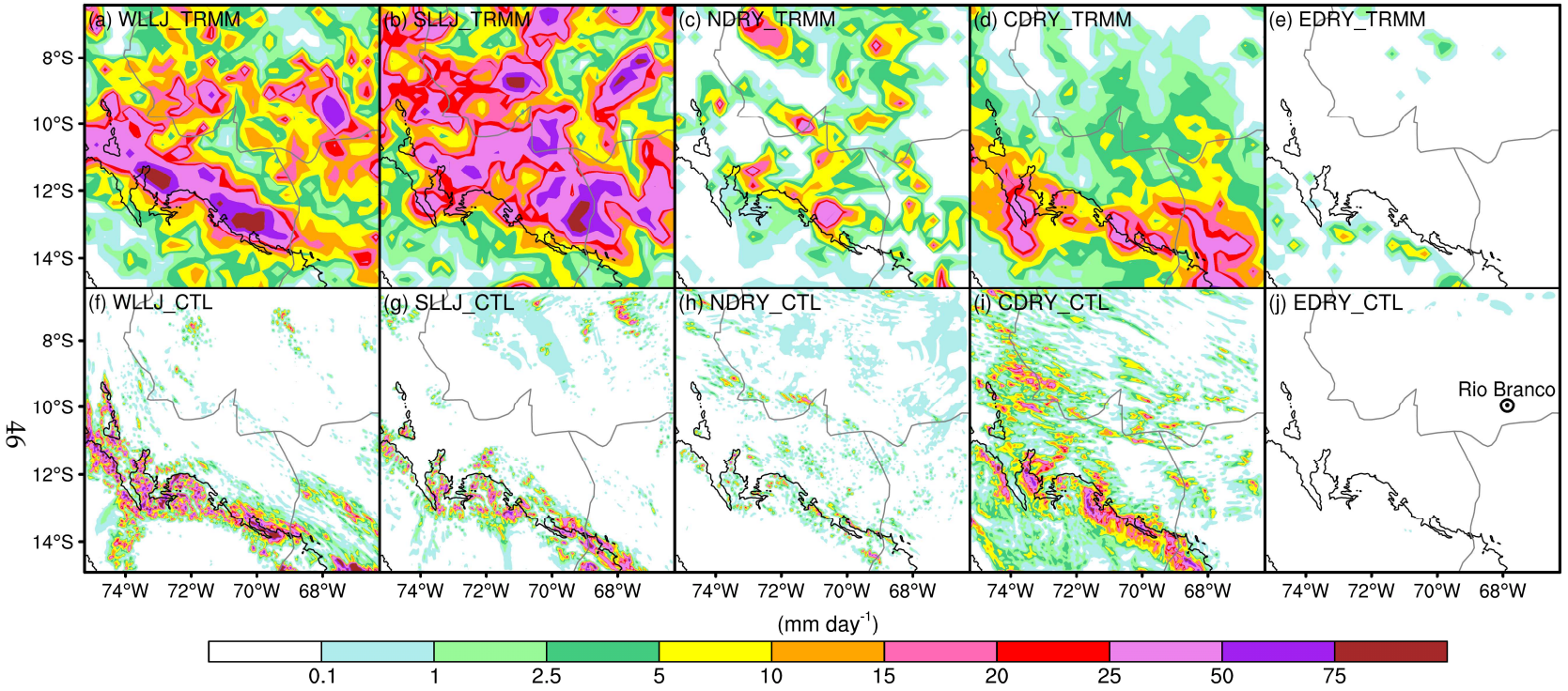

Figure 4.4: Daily precipitation (mm day^{-1}) from TRMM-3B42 (top) and WRFCTL simulations (bottom) as indicated in the panel titles. The black contours represent the 1000 m topography, with the black circle in panel (j) denoting Rio Branco, Brazil (9.96˚S, 67.87˚W) at 180 m in height. They are from the innermost nest (Δ_h = 1.2 km).

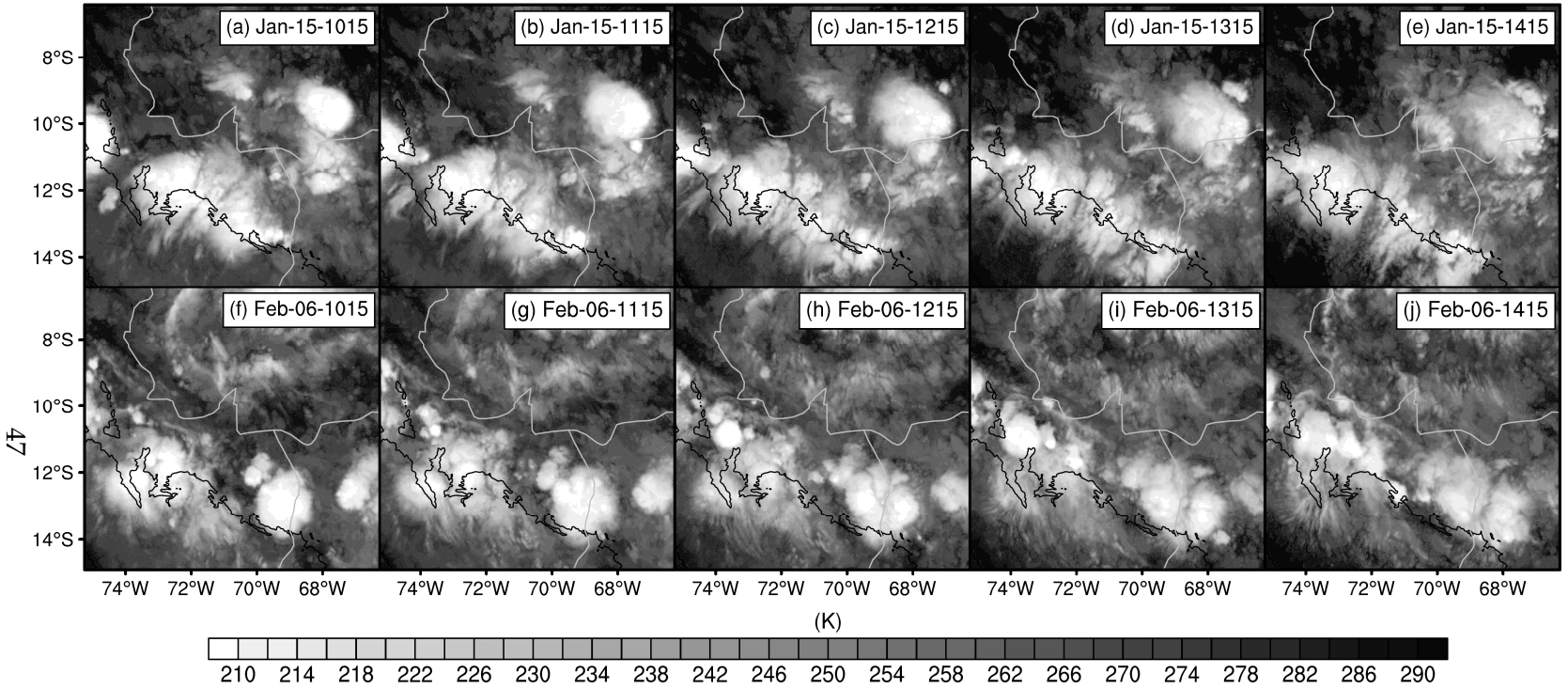

Figure 4.5: Cloud-top temperature (K) from GOES at various times (UTC) as indicated in the panel titles for WLLJ (top) and SLLJ (bottom). The black contours represent the 1000 m topography, with country borders in white.

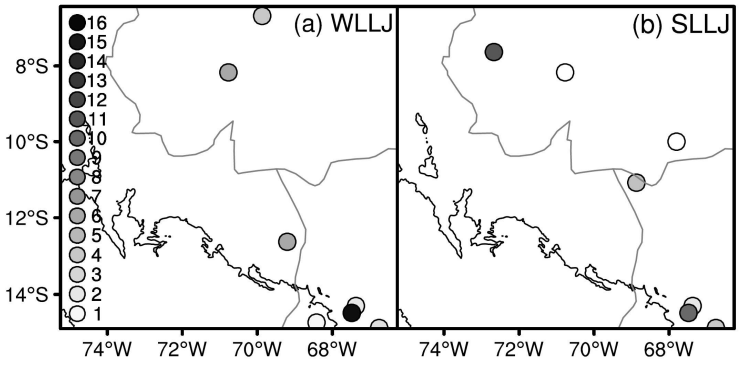

Figure 4.6: Daily precipitation (mm day^{-1}) from SALLJEX rain gauges for the (a) WLLJ and (b) SLLJ events (see Table 4.1 for details). The black contours represent the 1000 m topography.

The agreement with SALLJEX sounding observations at Rio Branco, Brazil (Figure 4.7; and see Figure 4.4j for its location) is the source of greater confidence on model results. Note that the differences with the observed wind speed at relatively high altitudes (column 1, Figure 4.7) can be explained by the fact that the weather balloon moves with the background wind and can be significantly downwind from the launch location by the time it is far above the ground (the vertical velocity is on the order of 0.02 m s^{-1}, while the horizontal wind speed roughly ranges from 1 to 15 m s^{-1}).

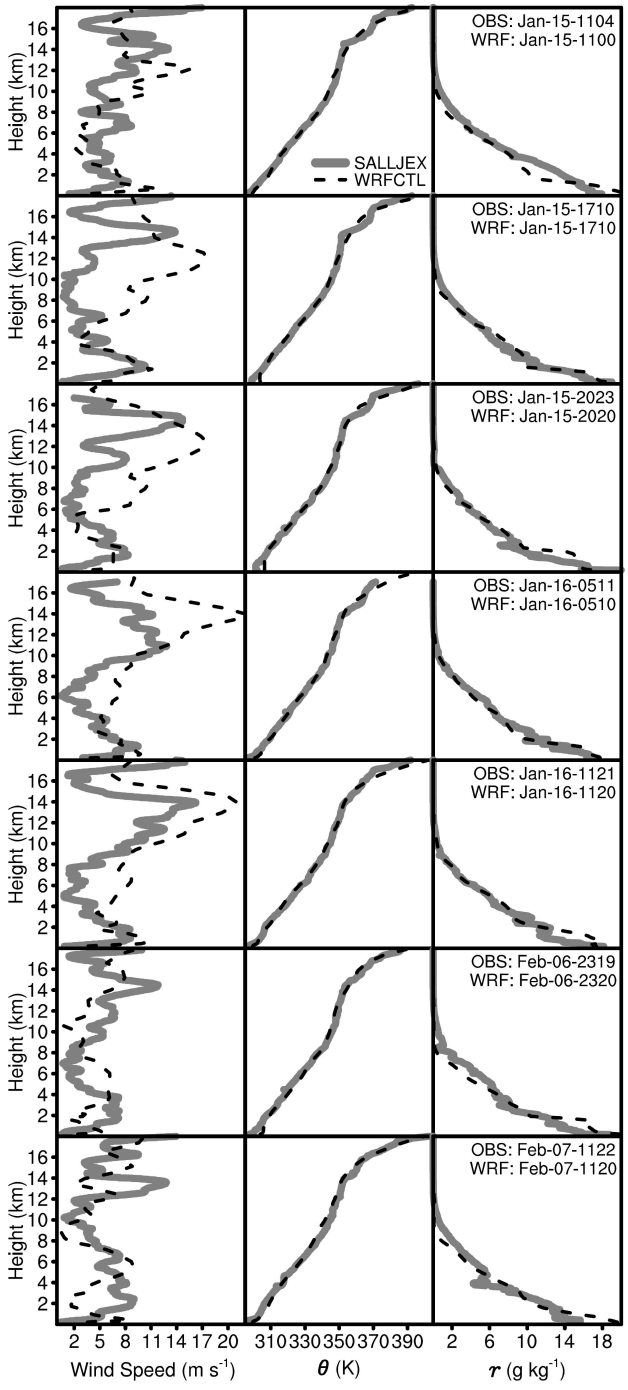

Figure 4.7: Vertical profiles of wind speed (m s^{-1}, left), potential temperature θ (K, center) and water vapor mixing ratio r (g kg^{-1}, right) from the SALLJEX sounding

(thick gray) and WRFCTL simulations (thin dashed black) in the innermost grid (Δ_h = 1. 2 km). The top five rows are for the WLLJ event, while the remaining two rows are for the SLLJ, with the corresponding times (UTC) indicated in the right column. The sounding is located at Rio Branco, Brazil (9.96˚S, 67.87˚W) at 180 m in height (see Fig. 4.4j).

5 Role of Surface ET on Moist Convection along the Eastern Andes

5.1 Introduction

Surface sensible and latent heat fluxes, redistributed aloft mainly through turbulent mixing in the boundary layer and by moist convection in the free atmosphere, function as the heat source needed to balance the net radiative cooling of the troposphere. Because the source is located at a higher pressure level than the sink, this process can be regarded as a heat engine (Rennó and Ingersoll 1996). Following this framework, Rennó and Ingersoll (1996) showed that the convective strength in equilibrium, as measured by the convective velocity scale w_s, depends explicitly on the heat input at the earth's surface (F_{in}):

$$w_s \approx \left[\left(\frac{c_p}{8\varepsilon_a \sigma_R T_c^3} \right) \frac{\eta F_{in}}{\mu} \right]^{\frac{1}{2}}, \tag{5.1}$$

where ε_a is atmospheric emissivity, σ_R is the Stefan-Boltzmann constant, T_c denotes the entropy-weighted mean temperature of the layer emitting infrared radiation, η is the efficiency of the heat engine and μ represents the mechanical dissipation coefficient, with c_p as the specific heat of air at constant pressure.

From the standpoint of parcel dynamics, as a subcloud-layer air sample is lifted adiabatically, the evolution of its convective available potential energy (CAPE) is described as follows (Emanuel 1994)

$$\frac{\partial CAPE_i}{\partial \tau} \approx \left(T_i - T_{LNBi}\right)\frac{\partial s_i}{\partial \tau} - \int_{z_i}^{z_{LNBi}} \left(\frac{gQ_R}{c_p T} - \frac{g}{\theta}\mathbf{v_r}\cdot\nabla\theta - N^2 w \right) dz \,. \tag{5.2}$$

The *subscript* i denotes properties of the air parcel i as it moves along within the boundary layer, with g representing the acceleration of gravity. For the remaining variables, τ stands for time in the reference frame of the parcel i, T is temperature, s is moist entropy, Q_R is radiative heating, θ is potential temperature, $\mathbf{v_r}$ represents the horizontal velocity relative to a coordinate system translating with the parcel, N^2 is the buoyancy frequency of unsaturated air, w is the large-scale vertical velocity and LNB indicates the level of neutral buoyancy. Equation (5.2) states that the energy available for convection depends on the parcel's entropy (the first term on the right-hand side of Eq. 5.2), which increases with surface evapotranspiration (ET), and processes adjusting the temperature of the atmosphere above the air parcel (the colder the upper level air, the larger the CAPE), including radiative cooling, horizontal advection and adiabatic cooling associated with large-scale ascent (the integral term on the right-hand side of Eq. 5.2). In the tropics and per scaling analysis, Emanuel (1994) demonstrated that the contribution from the surface ET is around 1.5 times greater than the effects owing to

large-scale motion and more than triple that of the radiative forcing. Thus, surface ET influences convective overturning through its impact on conditional instability, a central concept of moist convection for more than a century (Emanuel et al. 1994). This interaction between surface ET and convection was also noted by Barros and Hwu (2002), who identified a positive feedback of surface ET on local rainfall in the phase-space of surface Bowen ratio and tropospheric relative humidity using results from numerical simulations at the meso-γ scale and observations from the Oklahoma ARM-CART research site in the Southern Great Plains.

Over mountainous regions, the role of surface ET on rainfall processes has been also investigated previously through diagnostic studies. Based on the observations from the Monsoon Himalayan Precipitation Experiment (MOHPREX) and the NCEP-NCAR reanalysis, Barros and Lang (2003) found that ~15-35% of daily surface ET is recycled at the ridge-valley scale in the central Himalayas. This estimate is consistent with the results by Iwasaki (2004) who attributed a daily increase of precipitable water on the order of 2 to 5 mm to surface ET and ridge-valley circulations alone around Mount Tanigawa in Japan, and similar analysis by Bhushan and Barros (2007) using numerical simulations in the inner region of the Sierra Madre Mountains in Mexico. At seasonal scales and using the Regional Climate Model (RegCM3), Grimm et al. (2007) demonstrated that antecedent dry conditions over the Brazilian Highlands in the spring

can induce cyclonic circulations and enhance low-level moisture convergence, establishing favorable conditions for excessive rainfall in the subsequent summer. Focusing on southwestern Germany and eastern France (a mountainous region), Barthlott and Kalthoff (2011) conducted a set of simulations with varied initial soil moisture. They concluded that when the soil wetness is low and surface ET is limited by soil moisture availability, a positive relationship between daily rainfall and soil moisture exists; in contrast, for wet soils, where surface ET is controlled by net radiation, the influence of increasing soil moisture is tenuous and a systematic feedback is lacking. One limitation of previous modeling studies is that sensible and latent heat fluxes vary jointly and cannot be decoupled.

In the Southern Hemisphere, the most prominent mountain range is the Andes, running across seven countries from the north to the southern tip of South America. A salient climatic feature of this continent is the year-round South American Low Level Jet (SALLJ), carrying warm and moist air from the Amazon basin southward to 35˚S (Garreaud et al. 2009). With its core ranging from 1 to 1.5 km in height, this low level jet can be an important moisture source for the eastern slopes of the Andes (Lin et al. 2001; Giovannettone and Barros 2009). At higher elevations, the Bolivian high, a southwestward propagating Rossby wave forced by the condensational heating over the Amazon (Gill 1980; Lenters and Cook 1997), may also play a role on cloud formation and

precipitation. For instance, Garreaud (1999) showed that stronger than average easterly winds aloft over the central Andes, associated with a reinforcement and southward displacement of the Bolivian high, can promote upslope flows and enhance low-level easterlies within the Altiplano boundary layer, leading to increased moisture transport from the continental lowlands that feeds deep convection. In contrast with the central Himalayas, where LULCC (land-use and land-cover change) has severely reduced the density and connectedness of vegetation, the eastern slopes of the Andes are densely forested, and therefore it is expected that the ET contribution to the atmospheric moisture supply should be significant. This local effect was highlighted by Wei and Dirmeyer (2012) who conducted a diagnostic study to characterize the local versus remote impacts of soil moisture on precipitation (Eq. 1, Wei and Dirmeyer 2012). Relying on a back-trajectory method, their results suggest that during the austral summer, surface ET over the eastern Andes outweighs the contribution from remote regions (their Figure S4d), but the opposite occurs at higher altitudes (their Figure S4f).

The goal of this chapter is to understand the impact of local surface evapotranspiration (ET) on moist convection along the eastern flanks of the Andes (EADS), in particular its contribution to cloud formation and precipitation processes. In Chapter 2, the moderate-complex Noah land surface model (Chen and Dudhia 2001) and the revised MM5 surface layer (Jiménez et al. 2012) are simplified and an *assembled land*

surface for the Advanced Research Weather Research and Forecasting (ARW-WRF, Skamarock et al. 2008) model is formulated. This provides a framework to isolate the role of surface ET. The methodologies employed to quantify this effect are briefly reviewed in Chapter 3, with the apparent heat source and apparent moisture sink casted into σ-coordinates. The configurations of WRFCTL simulations are detailed in section 2.2, with the STRICT experiments involved in this chapter introduced in section 5.2. Analyses and interpretation of the results are presented in section 5.3. Conclusions and discussion are documented in section 5.4.

5.2 Numerical Experiments

To isolate the role of surface evapotranspiration, quasi-idealized experiments were conducted, where *at each time step* the surface sensible heat variables, including α, ε, T_{sk}, H, T_{soil} and T_{soilB}[1], are imposed exactly the same as in the WRFCTL runs described in section 2.2.2, but with E, such that LE, specified as zero when they represent a source to the atmosphere along the eastern flanks of the Andes. The eastern flanks of the Andes (EADS) are approximated as the elevation band between 500 and 3500 m and for the eastern side only (Figure 2.2). These experiments are labeled as

[1] For weather-scale simulations, T_{soilB} is generally set as time invariant.

WLLJ_ADS, SLLJ_ADS, NDRY_ADS, CDRY_ADS and EDRY_ADS, with their corresponding simulations (WRFCTL) detailed previously in section 2.2.2 named as WLLJ_CTL, SLLJ_CTL, NDRY_CTL, CDRY_CTL and EDRY_CTL, respectively. In the remainder of this dissertation, these quasi-idealized simulations are also referred as STRICT experiments, consistent with the fact that the surface sensible heat effect in these simulations are strictly identical to their WRFCTL runs. A summary overview of the experiments is presented in Table 2.1 (see also section 2.2.1 for the details of the selected weather conditions).

5.3 Results

Upon removal of surface ET, daily precipitation over the EADS is considerably reduced in the WLLJ_ADS (~52%, Figures 5.1a and 5.2a) and SLLJ_ADS (~46%, Figures 5.1b and 5.2b) simulations, along with dramatically decreased cloud content (cf. Figures 5.3a and 5.3b with 5.3f and 5.3g). Among the three remaining cases, although no influence is expected for EDRY (Figure 5.1e and cf. Figures 5.3e and 5.3j) based on the lack of clouds in the control simulation, the impacts on rainfall are marginal for both NDRY (Figure 5.1c) and CDRY (Figure 5.1d). Cloudiness changes very slightly in the CDRY (cf. Figures 5.3d and 5.3i), while the shallow clouds over the EADS in NDRY_CTL nearly disappear in the NDRY_ADS (cf. Figures 5.3c and 5.3h). Further, the feedback is

not constrained to daytime when the surface ET is strong, but also weakens nocturnal precipitation, especially in the cases of WLLJ and SLLJ (Figure 5.2).

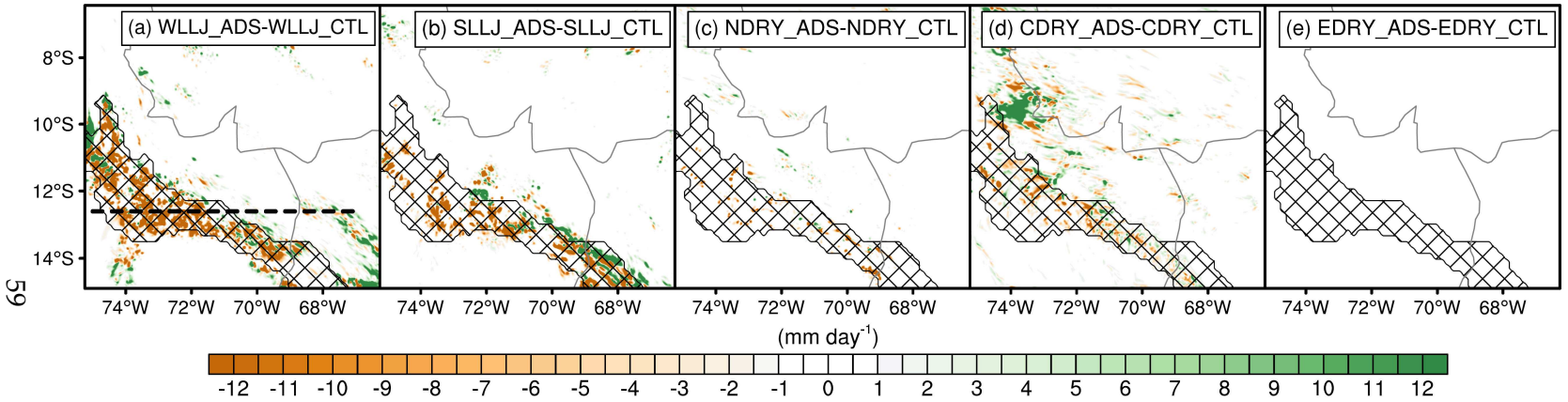

Figure 5.1: Residual of daily precipitation (mm day^{-1}) between the WRFCTL and STRICT simulations (STRICT - WRFCTL) as indicated in the panel titles, with the black mesh denoting the eastern flanks of the Andes (EADS). They are from the innermost domain (Δ_h = 1.2 km).

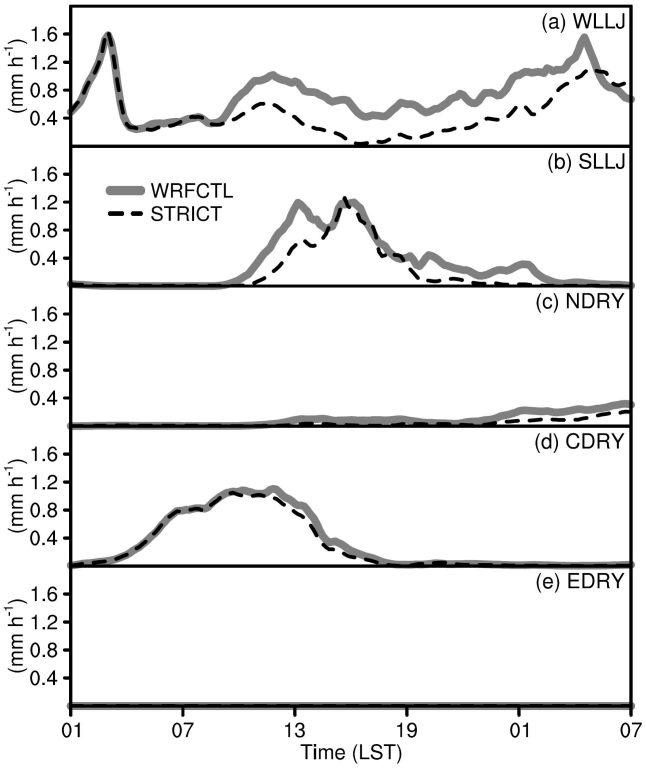

Figure 5.2: Rain rate (mm h^{-1}) from WRFCTL (thick gray) and STRICT (thin dashed black) simulations as indicated in the panel titles. They are averaged over the EADS (the black mesh in Fig. 5.1a) and from the innermost grid (Δ_h = 1.2 km).

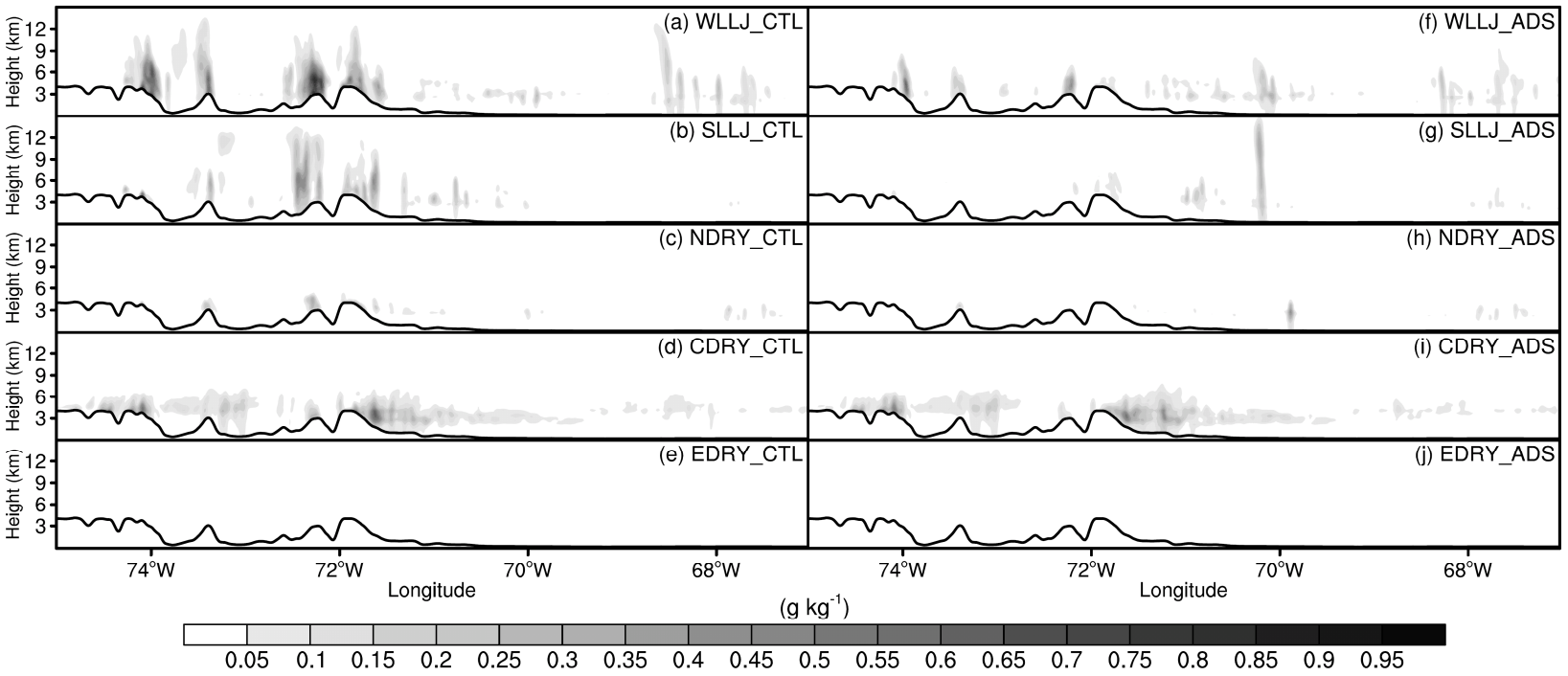

Figure 5.3: Daytime averaged cloud content (g kg^{-1}, cloud water, ice, snow and graupel) along the cross section denoted by the dashed line in Fig. 5.1a. As indicated in the panel titles, the left is for the WRFCTL simulations, while the right is for the STRICT experiments. They are from the innermost nest (Δ_h = 1.2 km).

5.3.1 Impact on Mass Balance

Analysis of the hydrostatic surface pressure tendency (Figure 5.4) indicates that surface ET and precipitation induced atmospheric mass modifications are trivial compared to convergence, which nearly balances mass changes within the air column over the EADS. The implication is that variations in clouds and precipitation in the STRICT experiments should not be *directly* related to air mass adjustment associated with the shutting down of surface moisture supplies to the atmosphere.

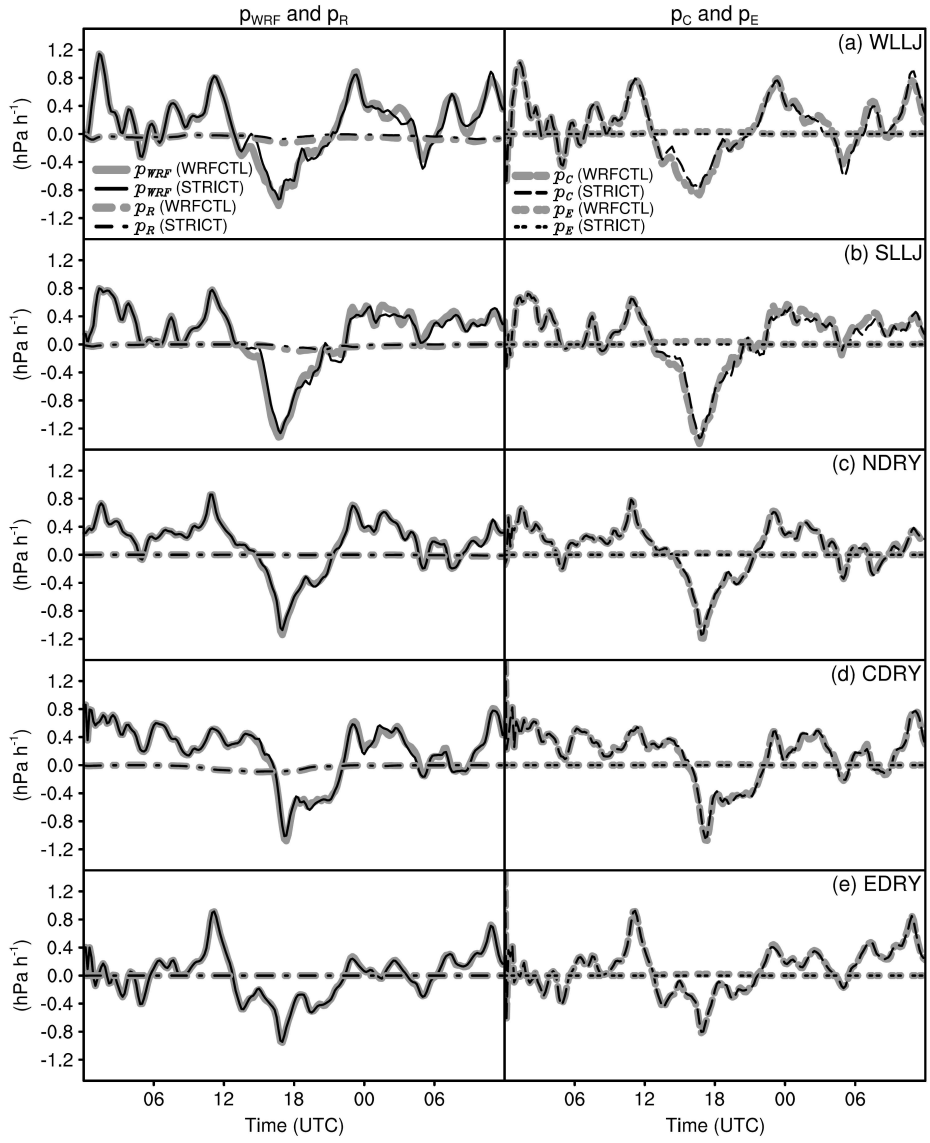

Figure 5.4: Hydrostatic surface pressure tendency (hPa h^{-1}) associated with precipitation ($p_R = -g\rho_l \overline{P}$, dashed-dot), convergence ($p_C = -g\nabla \cdot \int_0^{z_{top}} \rho_a \mathbf{v_H} dz$, dashed) and ET ($p_E = g\rho_l \overline{E}$, dotted), as well as the surface pressure tendency (hPa h^{-1}) diagnosed from the WRF model ($p_{WRF} = \frac{\partial \overline{p_s}}{\partial t}$, solid). They are averaged over the EADS and from the innermost grid (Δ_h = 1.2 km), with the thick gray (thin black) for the WRFCTL (STRICT) simulations as indicated in the panel titles.

5.3.2 Moisture Budget Analysis

The contribution from the land surface to the atmospheric moisture budget is not negligible in the two monsoon season events (WLLJ and SLLJ; see right panels of Figures 5.5a and 5.5b), but varies during the dry season: negligible in the CDRY (right panel, Figure 5.5d) while of the same order of magnitude as convergence in NDRY (right panel, Figure 5.5c) and EDRY (right panel, Figure 5.5e). Compared with the WRFCTL runs, the reduction of moisture convergence over the EADS is obvious in the WLLJ_ADS and SLLJ_ADS, but not so in the NDRY_ADS, CDRY_ADS and NDRY_ADS (right panels, Figure 5.5). Nonetheless, precipitation, when substantial, can be a strong sink of atmospheric moisture (left panels, Figures 5.5a, 5.5b and 5.5d), and convergence represents a significant moisture source or sink among all experiments (right panels, Figures 5.5).

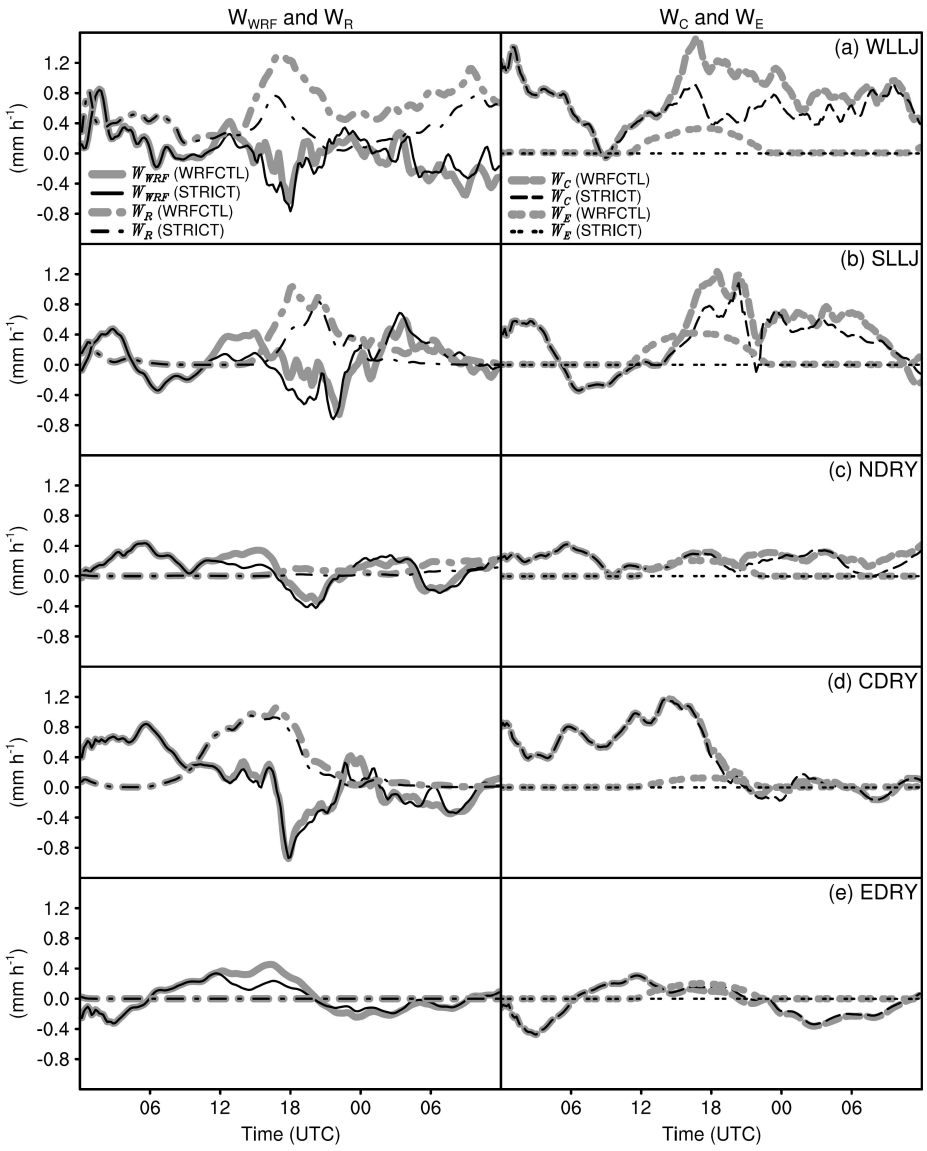

Figure 5.5: Moisture budget (mm h^{-1}) associated with precipitation ($W_R = P$, dashed-dot), convergence ($W_C = -\nabla \cdot \frac{1}{g}\int_0^{p_s} q\mathbf{v}_\mathbf{H} dp$, dashed), and ET ($W_E = E$, dotted), as well as the precipitable water tendency (mm h^{-1}) diagnosed from the WRF model ($W_{WRF} = \frac{\partial W}{\partial t}$, solid). They are averaged over the EADS and from the innermost grid (Δ_h = 1.2 km), with the thick gray (thin black) for the WRFCTL (STRICT) simulations as indicated in the panel titles.

5.3.3 Heat Balance, Convection and Interactions with the Environment

In the WLLJ_ADS and SLLJ_ADS, the convective available potential energy (CAPE) over the EADS decreases appreciably, with peak values dropping to ~500 J kg^{-1} from ~1200 J kg^{-1} in the corresponding WRFCTL simulations (Figures 5.6a and 5.6b). The level of free convection (LFC), another essential factor in triggering conditional instability, is also enhanced by up to ~3.5 km (not shown). This is consistent with the reduced low-level atmospheric water vapor content as shown in Figure 5.7 (row 1), because the surface moisture supply is eliminated and moisture convergence is reduced (Figures 5.5a and 5.5b). Correspondingly, the lifting condensation level (LCL), which is proportional to the dew point depression and a rough measure of potential cloud base, increases by as much as ~400 m (Figures 5.6a and 5.6b). The same situation applies to the NDRY_ADS, except at a smaller magnitude. For the CDRY (Figure 5.6d) and EDRY (Figure 5.6e), increase of LCL is still observed, although the modifications to CAPE are hardly identified since itself is already very low in the control simulations.

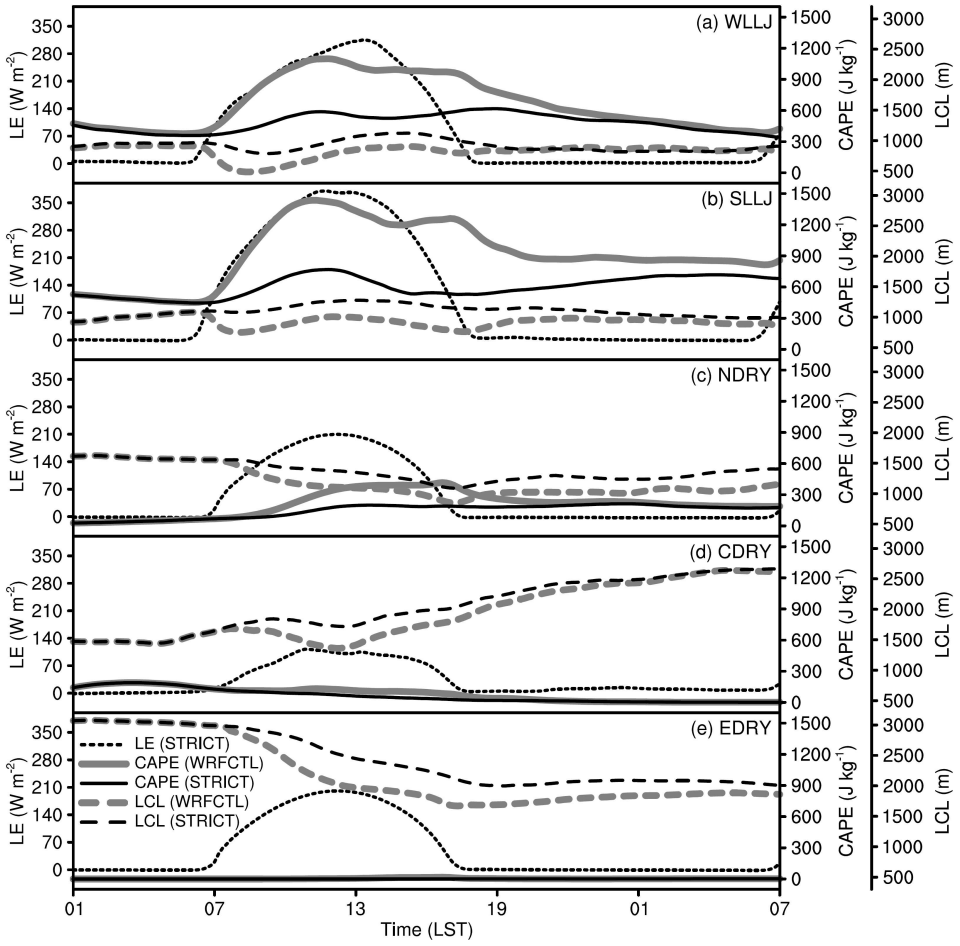

Figure 5.6: Surface latent heat flux *LE removed* from the atmosphere (W m^{-2}, dotted thin black) in the STRICT experiments, as well as CAPE (J kg^{-1}, solid) and LCL (m, dashed) from the WRFCTL (thick gray) and STRICT (thin black) simulations as indicated in the panel titles. They are averaged over the EADS and from the innermost domain (Δ_h = 1.2 km).

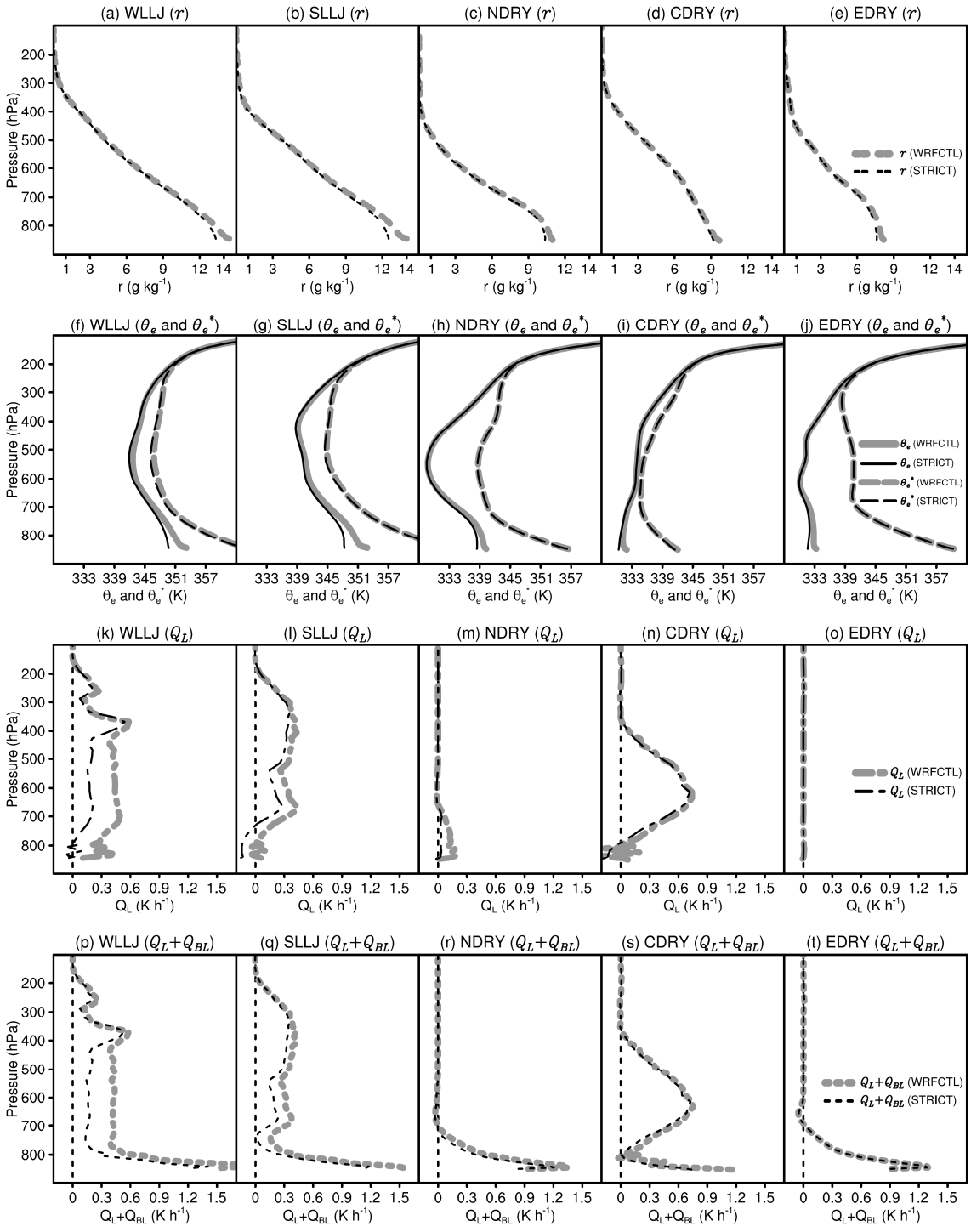
(a) WLLJ (r)
(b) SLLJ (r)
(c) NDRY (r)
(d) CDRY (r)
(e) EDRY (r)
Pressure (hPa)
r (g kg^{-1})
r (WRFCTL)
r (STRICT)
(f) WLLJ (θ_e and θ_e^*)
(g) SLLJ (θ_e and θ_e^*)
(h) NDRY (θ_e and θ_e^*)
(i) CDRY (θ_e and θ_e^*)
(j) EDRY (θ_e and θ_e^*)
θe and θe* (K)
θe (WRFCTL)
θe (STRICT)
θe* (WRFCTL)
θe* (STRICT)
(k) WLLJ (Q_L)
(l) SLLJ (Q_L)
(m) NDRY (Q_L)
(n) CDRY (Q_L)
(o) EDRY (Q_L)
QL (K h^{-1})
Q_L (WRFCTL)
Q_L (STRICT)
(p) WLLJ (Q_L+Q_{BL})
(q) SLLJ (Q_L+Q_{BL})
(r) NDRY (Q_L+Q_{BL})
(s) CDRY (Q_L+Q_{BL})
(t) EDRY (Q_L+Q_{BL})
QL+QBL (K h^{-1})
Q_L+Q_{BL} (WRFCTL)
Q_L+Q_{BL} (STRICT)

Figure 5.7: Daytime averaged vertical profiles of water vapor mixing ratio r (g kg^{-1}, double-dotted), equivalent potential temperature θ_e (K, solid), saturation equivalent potential temperature θ_e^* (K, dashed), latent heating Q_L (K h^{-1}, dashed-dot), as well as latent and turbulent heating $Q_L + Q_{BL}$ (K h^{-1}, dotted) from the WRFCTL (thick gray) and STRICT (thin black) simulations as indicated in the panel titles. They are averaged over the EADS and from the innermost domain (Δ_h = 1.2 km).

An approach to quantify directly the contribution of surface ET to CAPE is difficult to accomplish, because CAPE is released as the atmosphere evolves. However, a first-order understanding can be obtained under radiative-convective equilibrium (RCE) conditions, in which energy removed by an external forcing (e.g., radiation to space or adiabatic cooling due to forced ascent) is balanced by fluxes of sensible and latent heat from the earth's surface that have been mixed through the troposphere via convective motion. Assuming dissipation of kinetic energy is the only irreversible entropy source, and using the Raymond (1995) subcloud layer moist enthalpy budget as the closure, Emanuel and Bister (1996) showed that

$$CAPE \approx (h_b - h_m)\left[\frac{\overline{Q_A}\,\overline{T_{irr}}\left(\frac{1}{\overline{T}} - \frac{1}{T_s}\right)}{\overline{Q_{Acl}}}\right], \tag{5.3}$$

where h_b (h_m) represents the average moist static energy of downdraft air (the subcloud layer), $\overline{Q_A}$ ($\overline{Q_{Acl}}$) is the mass-integrated radiative heating of the atmosphere (the cloud layer), $\overline{T_{irr}}$ denotes the mean temperature at which entropy is produced by irreversible

processes [i.e., the temperature at which mechanical energy is dissipated (Klein 1997)], $\overline{T}$ is the mean temperature at which radiation is emitted by the atmosphere, and T_s is the surface temperature. When the subcloud layer is relatively shallow (e.g., left panels, Figure 5.3), $\overline{Q_A}$ is close to $\overline{Q_{Acl}}$ and related to the net absorption of radiation at the land surface $\overline{Q_s}$ as

$$\overline{Q_s} = -\overline{Q_A} \approx \overline{Q_H} + \overline{Q_{LE}} = \overline{Q_{LE}}(1+\beta), \tag{5.4}$$

where $\overline{Q_H}$ ($\overline{Q_{LE}}$) is the contribution from the surface sensible (latent) heating and β is the Bowen ratio. In Eq. (5.4), the ground heat flux is omitted, because during the daytime it is one to two orders of magnitude smaller than the surface sensible and latent heat fluxes. Hence, the contribution to CAPE owing to surface latent heat flux can be approximated by

$$FCAPE_{LE} = \frac{CAPE_{LE}}{CAPE} = \frac{1}{1+\beta}, \tag{5.5}$$

which decreases as β increases and drops fast when β is small (Figure 5.8). Specifically for the WLLJ, SLLJ and NDRY simulations in this study, when β is close to unity, the maximum $FCAPE_{LE}$ is around 60 percent (Figures 5.6a to 5.6c), roughly in agreement with Eq. (5.5).

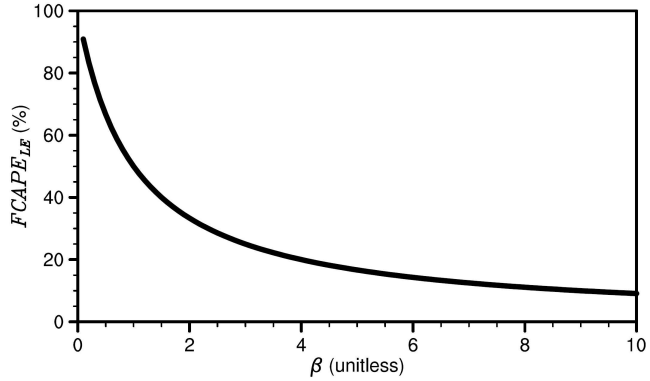

Figure 5.8: Surface latent heat flux contribution (%) to CAPE under radiative-convective equilibrium ($FCAPE_{LE}$) as a function of Bowen ratio β (based on Emanuel and Bister 1996).

Since the convective velocity scale

$$w_s \sim \sqrt{2CAPE}\ , \tag{5.6}$$

convection is expected to weaken if surface latent heat flux is prevented from entering the atmosphere, especially when it accounts for a large fraction of the surface energy budget. Indeed, the daytime maximum vertical velocity is strongly damped in the WLLJ_ADS (cf. Figures 5.9a and 5.9f) and SLLJ_ADS (cf. Figures 5.9b and 5.9g), as well as in the NDRY_ADS although to a lesser extent (cf. Figures 5.9c and 5.9h). For CDRY, it appears that the formation of clouds (cf. Figures 5.3d and 5.3i), and therefore precipitation (Figures 4.4d and 4.4i), is not associated with conditional instability. This is because in spite of the upward-decreasing saturation equivalent potential temperature (θ_e^*) in the lower troposphere, the equivalent potential temperature (θ_e) of an air parcel lifted from below ~700 hPa can never reach θ_e^* along its path (Figure 5.7i), consistent

with the low CAPE values in the CDRY (Figure 5.6d). On the other hand, typical of situations during the intrusion of Southern Hemisphere middle latitude systems, forced ascent over the EADS can be enhanced in the CDRY. The atmosphere in the CDRY_CTL, however, is potentially stable (θ_e increases with height), and merely modified slightly in the CDRY_ADS (Figure 5.7i). These properties imply that the precipitation produced in the CDRY experiment is primarily from elevated convection, and the role of the land surface becomes secondary. In EDRY, the atmosphere is conditionally stable throughout the entire troposphere and potentially near neutral below ~450 hPa (Figure 5.7j). The corresponding latent heating profile in Figure 5.7o indicates that either moist convection is absent or all the water condenses inside the cloud, if it exists, and eventually re-evaporates. Consequently, although the precipitable water vapor is reduced to some extent in the EDRY_ADS (solid black in Figure 5.5e), and thus the elevated LCL (Figure 5.6e), as surface moisture support accounts for a large portion of moisture budget (Figure 5.5e), no changes in convective activity can be detected (cf. Figure 5.9e and 5.9f).

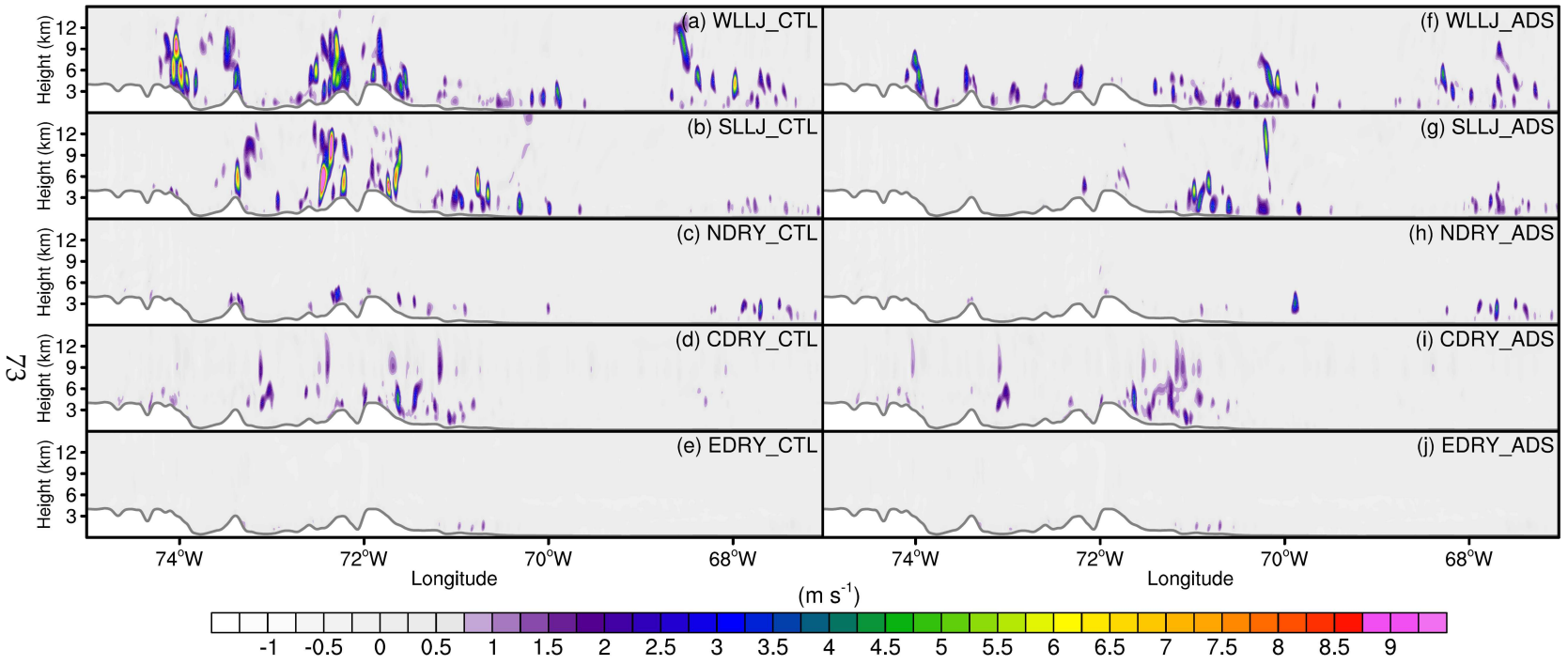

Figure 5.9: Daytime maximum vertical velocity (m s^{-1}) along the cross section denoted by the dashed line in Fig. 5.1a. As indicated in the panel titles, the left is for the WRFCTL simulations, while the right is for the STRICT experiments. They are from the innermost grid (Δ_h = 1.2 km).

The effects of convective clouds on the atmospheric environment can be quantified using the apparent heat source Q_1 and apparent moisture sink Q_2 shown in Figure 5.10. In the subcloud layer, however, the steep vertical gradients of Q_1 and Q_2 essentially result from boundary layer turbulent motions, instead of convection. This is because at low levels the major contributors to Q_1 and Q_2 are $-\frac{\partial\overline{\theta'\omega'}}{\partial p}$ and $L_v\frac{\partial\overline{q'\omega'}}{\partial p}$ associated with boundary layer turbulent mixing[1] rather than Q_L (cf. row 3 and 4, Figure 5.7) and Q_R, which is very small (not shown) [see Eqs. (3.7) and (3.8)]. In other words, although the penetrative updrafts and downdrafts can interact with the boundary layer and modify its properties, turbulent mixing dominates vertical eddy flux transport below the cloud base. Consequently, the enhanced boundary layer moisture sink (Q_2) in the STRICT experiments is associated with the elimination of surface moisture supplies (middle panels, Figure 5.10). As the difference between Q_1 and Q_2 represents the source or sink of moist static energy (MSE) h as follows (e.g., Yanai et al. 1973; Emanuel 1994):

$$\frac{\partial\bar{h}}{\partial t}+\overline{\mathbf{v_H}}\cdot\nabla\bar{h}+\bar{\omega}\frac{\partial\bar{h}}{\partial p}-Q_R=Q_1-Q_2, \tag{5.7}$$

[1] These two terms can be obtained from the YSU boundary layer scheme and equivalently parameterized as $\frac{\partial\theta}{\partial t}=-\frac{\partial\overline{\theta'\omega'}}{\partial p}$ and $\frac{\partial q}{\partial t}=-\frac{\partial\overline{q'\omega'}}{\partial p}$.

the bottom row panels of Figure 5.10 suggests that during the daytime, especially for the WLLJ and SLLJ, the boundary layer serves as a source of MSE, which is significantly reduced when the surface ET is removed. This explains the lower θ_e in the STRICT experiments (row 2, Figure 5.7), thus the damped conditional instability, owing to the relationship between these two variables ($dh \approx c_p T d \ln \theta_e$, Holton 2004). The extent of this reduction appears to be somewhat proportional to the surface latent heat taken away from the system (Figure 5.6), as illustrated by the fact that the CDRY exhibits the slightest variations (Figure 5.10i).

In the free atmosphere, the profiles of Q_1 and Q_2 are dominated by convection (cf. rows 3 and 4 of Figure 5.7). When deep convection is present, such as in the WLLJ, SLLJ and CDRY as indicated by the relevant latent heating profiles (Figures 5.7k, 5.7l and 5.7n), convective clouds affect nearly the entire depth of the troposphere. This is further confirmed by the fact that Q_1 peaks at an altitude above the peak of Q_2 (Yanai et al. 1973), but not in the NDRY (Figures 5.10c and 5.10h) and EDRY (Figures 5.10e and 5.10j). Overall, deep convection tends to heat and dehumidify the surrounding environment (Figures 5.10a, 5.10b, 5.10d, 5.10f, 5.10g and 5.10i), mainly through compensating subsidence (Yanai et al. 1973). Accompanied with damped convection, the free atmosphere in WLLJ_ADS and SLLJ_ADS is colder and drier than in the corresponding WRFCTL runs. Clearly, convection acts as a net sink of MSE at low levels

(above the boundary layer) but as a source in the middle and upper troposphere (bottom panels, Figure 5.10), and tends to neutralize the atmosphere.

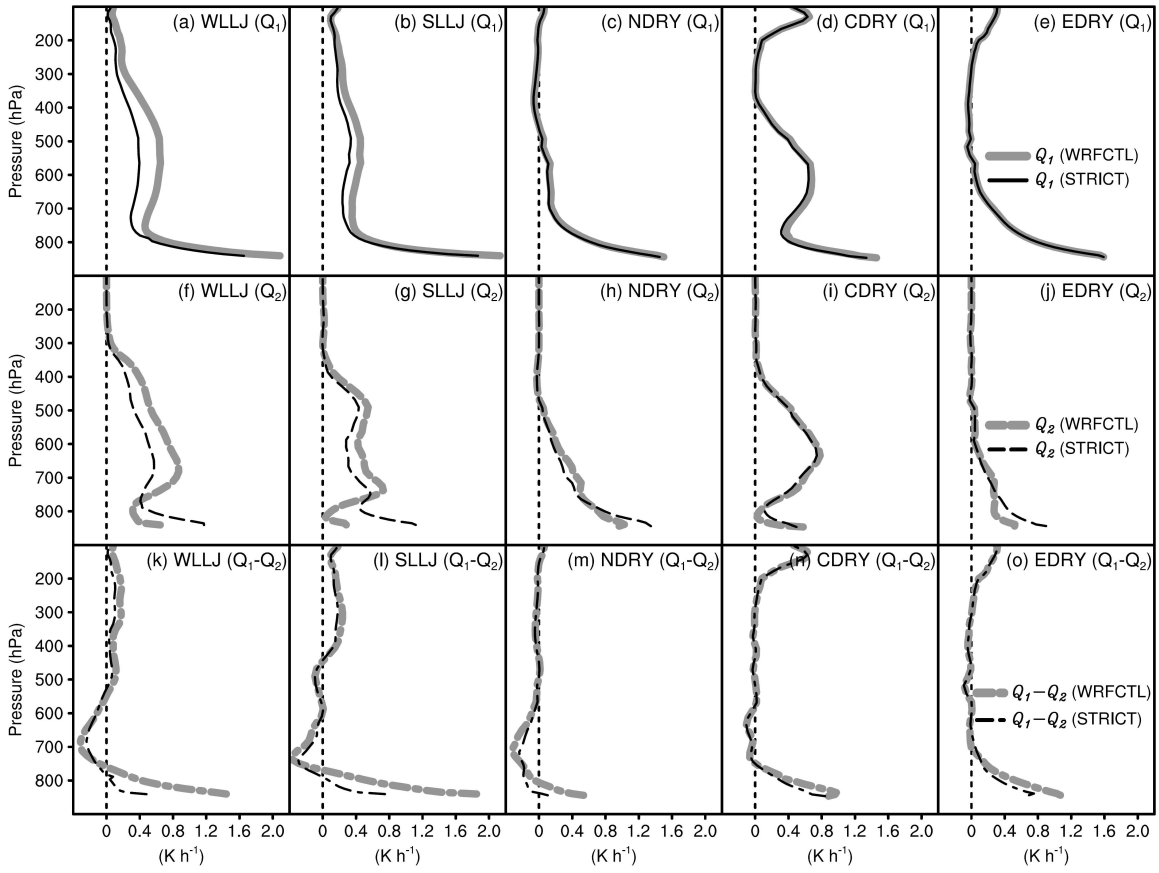

Figure 5.10: Daytime averaged Q_1 (solid), Q_2 (dashed) and $Q_1 - Q_2$ (dashed-dot) in K h^{-1} from the WRFCTL (thick gray) and STRICT (thin black) experiments as indicated in the panel titles. The spatial average is conducted over the EADS within the innermost nest (Δ_h = 1.2 km).

The vertical eddy fluxes also vary with the strength of convection. For instance, the upward transport of FC_H is much weaker in the WLLJ_ADS and SLLJ_ADS than in the WLLJ_CTL and SLLJ_CTL (Figures 5.11a and 5.11b). In the lower troposphere,

including the boundary layer, the downward FC_{LE} can be associated with evaporation of raindrops, and enhanced in the STRICT experiments. Above that level, however, the profiles of FC_{LE} of the WRFCTL and STRICT experiments are nearly indistinguishable. In part, this can be due to the offset between reduced drying and damped convection in the WLLJ_ADS and SLLJ_ADS throughout the mid to upper troposphere. Alternatively, as Q_2 is more sensitive to microphysical processes (Emanuel 1994), the close agreement of FC_{LE} profiles in these two cases could be associated with adjustments of entrainment and detriment processes. As illustrated in Figure 5.11i, despite its deep convective nature, the vertical eddy flux of latent heat in the CDRY is trivial, supporting our inference that the precipitation is not closely related to surface thermodynamic processes but externally forced by large-scale ascent. For EDRY, the monotonically decreased vertical eddy flux for total heat is indicative of convective inhibition, similar to the suppressed regime described by Thompson et al. (1979, their Figure 20).

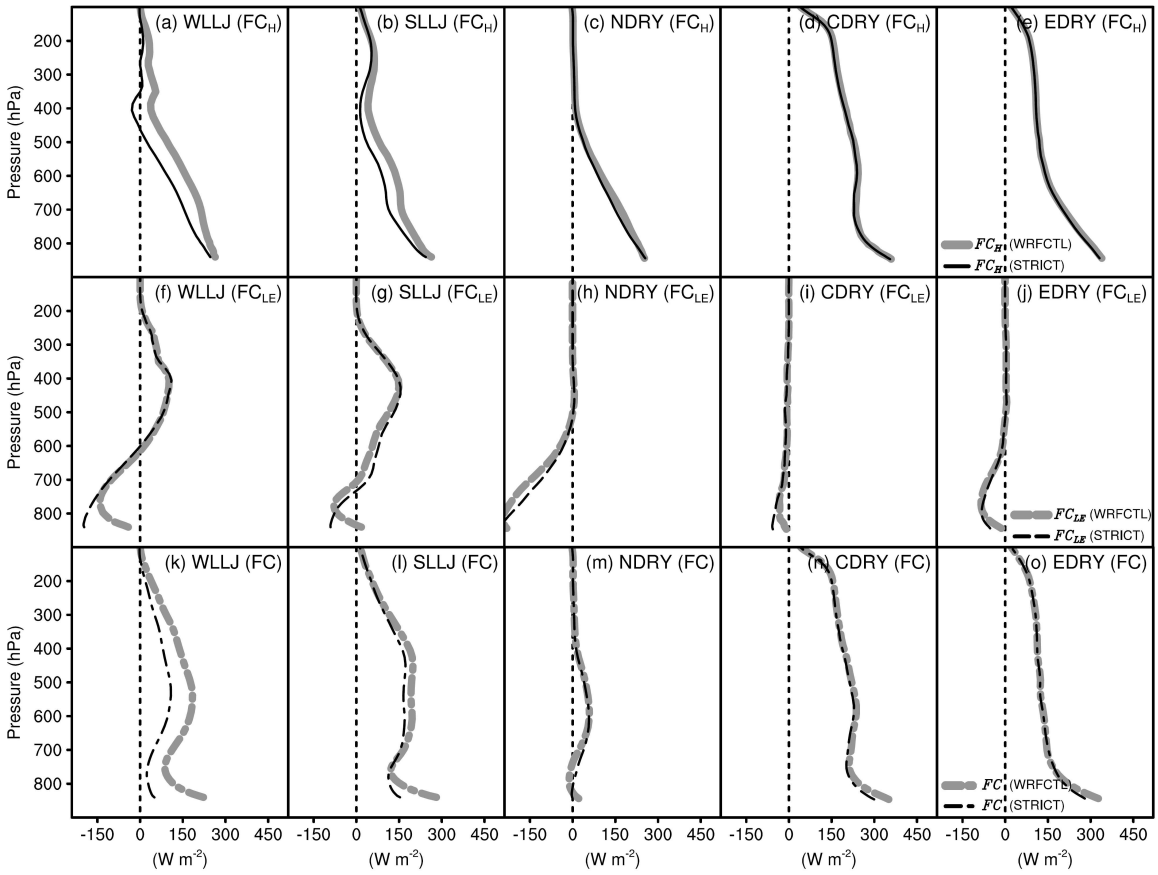

Figure 5.11: Daytime averaged vertical eddy flux for sensible (FC_H, solid), latent (FC_{LE}, dashed) and total (FC, dashed-dot) heat in W m^{-2} from the WRFCTL (thick gray) and STRICT (thin black) experiments as indicated in the panel titles. The spatial average is conducted over the EADS within the innermost domain (Δ_h = 1.2 km).

Characterized by damped convection, the atmosphere is generally colder in the STRICT experiments (row 1, Figure 5.12), except within the boundary layer of the SLLJ_ADS (Figure 5.12b) and EDRY_ADS (Figure 5.12e). This implies that in these two experiments even though evaporative cooling is enhanced at low levels (not shown) as the atmosphere is relatively dry (row 1, Figure 5.7), other processes, e.g., advection, can

dominate. Nevertheless, the differences do not exceed 0.3 K among all simulations. In ARW-WRF3.4.1 (Skamarock et al. 2008), the moist Brunt-Väisälä frequency (N^2) is defined as

$$N^2 = \begin{cases} g\left(A\frac{\partial \theta_e}{\partial z} - \frac{\partial r_T}{\partial z} \right), & r \geq r^* \quad or \quad r_c \geq 0.01g \quad kg^{-1} \\ g\left(\frac{1}{\theta}\frac{\partial \theta}{\partial z} + 1.61\frac{\partial r}{\partial z} - \frac{\partial r_T}{\partial z} \right), & r < r^* \quad or \quad r_c < 0.01g \quad kg^{-1} \end{cases}, \tag{5.8}$$

where r_T stands for total water mixing ratio, r^* represents saturation water vapor mixing ratio, r_c is cloud water mixing ratio, and $A = \frac{1}{\theta}\frac{1+\frac{1.61\varepsilon L_v r}{R_d T}}{1+\frac{\varepsilon L_v^2 r}{c_p R_v T^2}}$ with R_v as the gas constant for water vapor and ε as the ratio of the molecular weight of water to the mean molecular weight of dry air. In the lower troposphere and when the atmosphere is saturated, the effect of eliminating surface ET on N^2 is not straightforward, since both $\frac{\partial \theta_e}{\partial z}$ (row 2, Figure 5.7) and $\frac{\partial r_T}{\partial z}$ (not shown) tend to become less negative. Under unsaturated conditions, however, the Brunt-Väisälä frequency in the subcloud layer may be approximated as

$$N^2 = g\left(\frac{1}{\theta}\frac{\partial \theta}{\partial z} + 0.61\frac{\partial r}{\partial z} \right), \quad r < r^* \quad or \quad r_c < 0.01g \quad kg^{-1}, \tag{5.9}$$

since $r \approx r_T$. Thus, N^2 can be less negative or more positive in the STRICT experiments, because $\frac{\partial r}{\partial z}$ tends to be less negative (row 1, Figure 5.7) while the variation of $\frac{1}{\theta}\frac{\partial \theta}{\partial z}$ is trivial as indicated by the marginally modified temperature profiles shown in Figure 5.12 (row 1). Indeed, as documented in the second row panels of Figure 5.12, the atmosphere is more statically stable in the lower troposphere in the STRICT simulations. This renders a relatively small Froude number $F_r = \frac{U}{Nh_m}$ (U is the basic flow speed and h_m denotes mountain height) for that layer, and therefore weaker upslope flows (Lin 2007) that result in slightly reduced mass convergence over the EADS (row 3, Figure 5.12). However, the influence on the low-level moisture convergence is appreciable, for the WLLJ and SLLJ in particular, because of the moisture-rich atmosphere. This is also in agreement with the moisture budget analysis documented in Figure 5.5 (right panels).

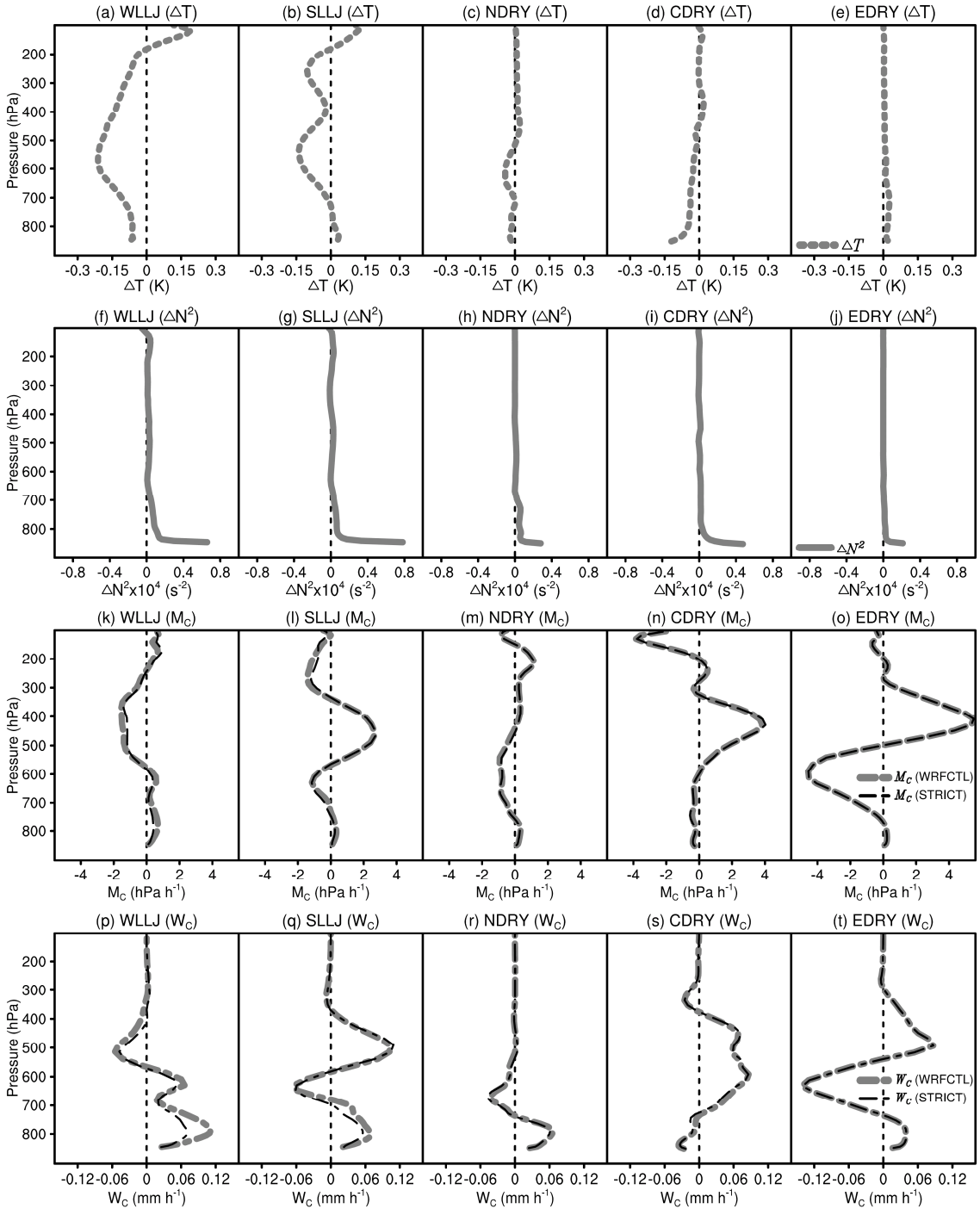

Figure 5.12: The top row panels document the vertical profiles of the residual of daytime averaged temperature ΔT (K, dotted gray) between the WRFCTL and

STRICT simulations (STRICT - WRFCTL) as indicated in the panel titles. The second row panels are the same as the top ones, but for moist Brunt-Väisälä frequency ΔN^2 (s^{-2}, solid gray). The remaining two rows are the daytime averaged vertical profiles of mass convergence M_c (hPa h^{-1}, solid) and moisture convergence W_c (mm h^{-1}, dashed) from the WRFCTL (thick gray) and STRICT (thin black) simulations, respectively. They are averaged over the EADS and from the innermost grid (Δ_h = 1.2 km).

5.4 Conclusions and Discussion

Instead of perturbing soil moisture, the role of surface evapotranspiration (ET) along the eastern flanks of the Andes (EADS) was investigated using an *assembled land surfac*e. Essentially, it is comprised of 13 "connectors" *from the land surface to the atmosphere* and proved to be necessary and sufficient according to a group of one-hour simulations described in Section 2a. This framework, as well as a comprehensive examination of the Noah and RMM5 schemes, provides a clear representation of *land surface sensible heat effects* in the WRF model. In this regard, quasi-idealized experiments were conducted, where at *every time step* the surface sensible heat effects are exactly the same as in the reference runs while surface moisture and latent heat fluxes are prevented from entering the atmosphere if they represent a source.

Covering a wide spectrum of weather conditions in South America and through simulations down to 1.2 km grid spacing, our results suggest that surface ET along the EADS has a significant influence on moist convection through its impact on conditional instability (e.g., in the WLLJ, SLLJ and NDRY), because it acts as an important source of moist entropy to the air parcels within the boundary layer as illustrated by the detailed

energy balance analysis. Specifically, up to ~60% CAPE can be explained by surface ET along the EADS. Given that convective motion is strongly attenuated after removing surface ET, there is a dramatic decrease in cloudiness, with daily precipitation reduced by up to ~50% in the WLLJ_ADS and SLLJ_ADS experiments. In contrast, when convection is not thermally driven (CDRY) or under conditionally stable conditions (EDRY), the effect of surface ET becomes secondary.

At the mountain range scale, removal of surface ET weakens upslope flows by increasing static stability in the lower troposphere. As illustrated by Eq. (5.9), this is related to the fact that the vertical gradient of water vapor mixing ratio in the lower troposphere tends to be less negative. Although the impact on mass convergence is trivial, the influence on moisture transport is obvious, because the atmospheric water vapor content primarily concentrates at low levels. In the STRICT experiments, the decreased moisture convergence operates in concert with the elimination of surface ET.

Further seasonal simulations of South America at 18 km grid increment show that during most of the time in the austral summer the troposphere over the EADS is conditionally unstable, which is also largely the case during the transition from the dry to wet season (Sun and Barros 2014b, in preparation). This implies that the surface ET associated with montane forests plays an active role in retaining cloudiness, and consequently in rainfall harvesting at high elevations (Barros 2013). Immersed in low

clouds for additional water and nutrients through canopy interception (Beiderwieden et al. 2007), Andean cloud forests are more vulnerable to this process, since without surface ET the LCL can be elevated by as much ~400 m.

Moisture budget analysis (Figure 5.5) points to the importance of moisture transport from the adjacent Amazon lowlands. This is in keeping with earlier Amazonia deforestation studies. For instance, variations of Andean rainfall were reported in Medvigy et al. (2011, their Figure 3a), where the Amazon forest was completely logged in a General Circulation Model. The impact of surface ET in the Amazon on precipitating processes in the high Andes will be addressed separately from other land surface attributes in Chapter 6.

6 Impact of Amazonian ET on Moisture Transport and Convection along the Eastern Andes

6.1 Introduction

Harboring the most extensive rainforest, the Amazon basin represents the largest source of terrestrial evapotranspiration (ET) in the planet (Jun et al. 2010, their Figure 1a). In this region, surface moisture flux, and the related latent heat, can be crucial to atmospheric convection, since the temperature gradient is generally weak in the tropics and diabatic heating appears as the primary convective energy source. The dominant role of diabatic heating was elucidated by Gill (1980), who demonstrated that symmetric heating about the equator in the maritime subcontinent can generate low-level westerly inflows into the heated area via westward propagating Rossby waves, and low-level easterlies over the Pacific through eastward propagating Kelvin waves. Upon meridional integration, Gill's solution to the east of the heating source resembles the Walker cell, while the zonally averaged flow bears typical features of Hadley type circulations. The success of Gill's model motivated further studies for South America, analytically and numerically (e.g., Silva Dias et al. 1983; DeMaria 1985; Figueroa et al. 1995). With specified heating profiles, these authors consistently reported well simulated Bolivian high, a prominent component of summertime upper-level circulations over South America, although the Andes topography needs to be incorporated to reproduce the Northeast ("Nordeste" in Portuguese) low and improve the accuracy of the

simulated South Atlantic convergence zone (SACZ) (Figueroa et al. 1995). Admittedly, studies with a priori prescribed heating profiles do not fully describe regional atmospheric dynamics as feedbacks to the forcing are excluded, the results by Lenters and Cook (1997), however, further corroborate that condensational heating, which can be modified by topography and not necessarily confined within the Amazon, is the fundamental driver behind.

On the other hand, Salati (1987) showed that during the austral summer, the wet season in South America, nearly half of the water vapor converted as precipitation over the Amazon originates from the tropical Atlantic (see also Figure 6.3). High moist static energy air from the Atlantic (Ma et al. 2011, their Figure 10) is advected toward the continent (see e.g., Figures 6.8f and 6.8g) and modifies convective activity within the Amazon. At longer time scales, the balance between the local (surface ET) and remote moisture sources has significant implications on South American monsoon. As pointed out by Li and Fu (2004), if the local surface moisture flux is an important source of moisture, the onset of the wet season would be delayed with decreased pre-season surface ET; on the contrary, if the primary moisture source is from the Atlantic, pre-season dry conditions would accelerate the wet to dry seasonal transition, due to enhanced land-ocean temperature contrast and moist static energy gradients. Most literatures documented stronger controls per the sea surface temperature in the tropical

Atlantic and/or over the Pacific Oceans (e.g., Hastenrath and Heller 1977; Moura and Shukla 1981; Fu et al. 2001), the large values of precipitation recycling ratio over the Amazon (Salati et al. 1979; Eltahir and Bras 1994), however, imply that the influence of surface ET may not be trivial. The first attempt to reconcile these two aspects was made by Li and Fu (2004), who divided the evolution of South American monsoon into initiation, developing and mature phases. Based on ECMWF (European Centre for Medium-Range Weather Forecasts) reanalysis, they concluded that surface fluxes, latent heat flux in particular, play an important role on monsoon initiation, building up available potential energy, destabilizing the atmosphere and promoting the switch from net moisture divergence to convergence. Although their analysis suggests that the influence of surface fluxes becomes secondary after initiation, it indicates that lower land surface latent heat fluxes during the dry season and the initiation phase of the monsoon tend to delay the large-scale circulation transition over the Amazon. Nevertheless, whether surface ET *itself* can induce significant atmospheric adjustment and how this interacts with larger-scale systems remain elusive.

Situated along the western side of South America, the climate of the Andes varies along with the atmospheric conditions over the Amazon. For instance, trajectory

analysis showed that the summertime precipitation over the Altiplano plateau[2] originates eastward of the central Andes (Vuille et al. 1998; Garreaud 1999). As revealed in Garreaud (1999, 2000a), the summertime rainy episodes over the plateau are closely related to the mean easterlies in the middle and upper troposphere, because the downward turbulent momentum mixing into the boundary layer is the leading contributor causing enhanced upslope flows. Thus, the position and intensity of the Bolivian high, associated with the upper-level flow anomalies, may play a role on shaping the intraseasonal rainfall variability over the Altiplano (Garreaud et al. 2003, their Figure 3). More recently, the connections between Amazon and high Andes rainfall were examined by Vizy and Cook (2007), where a regional model was employed to simulate conditions during the Last Glacial Maximum (LGM, ~21,000 year ago), when the Amazon was drier than present-day conditions. Their model results suggest that Amazonian convection delayed in the austral spring is concurrent with precipitation increases over the Andes. They argued that this is due to a stronger zonal geopotential height gradient toward the west, rendering upslope winds more perpendicular to the Andean mountain range. Since the variation of wind fields was attributed to the weakened thermal low over the South American continent during the LGM, which in

[2] The Altiplano, also known as the Bolivian Plateau, is an elevated region around 250 km wide and roughly spans from 15°S to 22°S.

turn was linked to surface temperature response, the findings from Vizy and Cook (2007) still stem from the coupled adjustment of surface sensible and latent heat fluxes.

In Sun and Barros (2014, henceforth SB14), a framework was proposed to isolate the role of surface ET on moist convection. Specifically, the moderate-complex Noah land surface model (Chen and Dudhia 2001, henceforth Noah) and the revised MM5 surface layer (Jimenéz et al. 2012, henceforth RMM5) in the Advanced Research Weather Research and Forecasting (ARW-WRF3.4.1, Skamarock et al. 2008) model were simplified as an *assembled land surface* that only relies on 13 independent variables to represent the feedbacks from the land surface to the atmosphere

$$F_{LA} = f\left(\alpha,\ \varepsilon,\ T_{sk},\ H,\ E,\ z_0,\ F_{\psi_m},\ F_{\psi_h},\ R_B,\ u_{10},\ v_{10},\ u_*,\ U_L\right), \quad (6.1)$$

where α denotes albedo; ε is emissivity; T_{sk} is surface skin temperature; H and LE are surface sensible and latent fluxes respectively; z_0 represents surface roughness length; F_{ψ_m} (F_{ψ_h}) is a function of stability function for momentum ψ_m (heat/moisture ψ_h); R_B represents bulk Richardson number; u_{10} and v_{10} are the 10 m wind speed; u_* is the frictional velocity; and U_L stands for the adjusted lowest model level wind speed to adapt free convection conditions (Beljaars 1995) with sub-grid velocity scale considerations (Mahrt and Sun 1995). Given the variables in Eq. (6.1), also referred as "connectors" in SB14, formulate the unique path from the land surface to the atmosphere (see Section 2a of SB14 for the verification), provided their values are exactly

the same at *every time step*, any simulation shall produce identical atmosphere even in the absence of Noah and RMM5. This offers the chance to define surface sensible heat effects, i.e., any temperature related variables involved in the computation of these connectors. After a thorough examination of ARW-WRF3.4.1 [Eqs. (4) to (22) of SB14], SB14 found that α, ε, T_{sk}, H, T_{soil} (soil temperature) and T_{soilB} (bottom soil temperature) represent the land surface sensible heat effects exclusively. This is appealing, because if the surface sensible heat effects are known and specified at *each time step*, it is possible to isolate latent heat effects. For example, if the surface sensible heat effects are exactly the same as in reference runs, the specific contribution of surface ET can be characterized independently. One key advantage of this approach is that complications from changes of other land surface properties, such as albedo, surface roughness and Bowen ratio are eliminated.

The principal objective here is to understand the role of Amazonian evapotranspiration (ET) on moisture transport and convection along the eastern flanks of the Andes (EADS), approximated as the elevation band between 500 and 3500 m (Figure 2.2). The motivation stems from the substantial deforestation and LULC (Land-Use Land-Cover) change in the Amazon basin in the past decades (Skole and Tucker 1993), which is expected to increase with the Interoceanic Highway and ongoing urbanization, mining dam building projects (Walker et al. 2011). Certainly, the approach

followed here does not amount to deforestation proper, but it provides a fundamental examination of the atmospheric response (and thus impacts) to changes in surface moisture supply in the AMZL. We first focus on complete removal of surface ET to identify the physical impacts, and then rely on stepwise removal and addition of surface ET as a surrogate of progressive forest thinning or densification. The remainder of this Chapter is structured as follows. Section 6.2 describes the numerical simulations conducted, with the methodologies quantifying the relevant effects briefly reviewed in Chapter 3. Analyses and interpretation of the results are detailed in section 6.3, followed by conclusions and discussion in section 6.4.

6.2 Numerical Experiments

The Advanced Research Weather Research and Forecasting (ARW-WRF3.4.1, Skamarock et al. 2008) model was employed for simulations presented in this Chapter. They were implemented on three nests (316 × 496, 433 × 604 and 756 × 726 grid elements) at 18, 6 and 1.2 km grid spacing (Figure 2.2), with 60 sigma levels in the vertical and 14 of them concentrating in the lowest 1 km. To avoid discontinuities across lateral boundaries between nested grids (e.g., Figure 2 of Sun and Barros 2013), one-way nesting was applied. The physics options used are the Dudhia shortwave, RRTM longwave (Rapid Radiative Transfer Model), Lin et al. microphysics, Kain-Fritsch cumulus (for the two outer domains only), Yonsei University (YSU) boundary layer,

revised MM5 surface layer and Noah land surface (Skamarock et al. 2008, and references therein).

The weather conditions investigated are the same as in Chapter 5 (Figure 2.1 and Table 2.1), including 1) a weak low level jet (LLJ) event accompanied with a prominent Bolivian high (WLLJ, Jan. 15, 2003); 2) a strong LLJ condition but weakened Bolivian high (SLLJ, Feb. 6, 2003); 3) a dry season precipitation case with accumulations around the climatological mean (NDRY, Jun. 28, 2003); 4) a rainy day in the austral winter characterized by cold surge (CDRY, Aug. 9, 2003); and 5) a rainless situation during which precipitation is nearly absent over the EADS (EDRY, Jul. 20, 2003). The former two are frequently observed in the wet season, while the latter three are for the austral winter. Essentially, the primary atmospheric features related to precipitation process along the EADS, such as the SALLJ (Giovannettone and Barros 2009), Bolivian high (Garreaud 1999) and cold surge (Garreaud 2000b), are considered in these numerical experiments. They are for the year of 2003 to take the advantage of existing observations from the South American LLJ Experiment (SALLJEX, Nov. 15, 2002 to Feb. 15, 2003; Vera et al. 2006).

The atmospheric initial and lateral boundary conditions were derived from the Final Operational Global Analysis produced by the National Centers for Environmental Prediction (NCEP-FNL), while the initial land surface conditions were obtained from the

National Center for Atmospheric Research (NCAR) High-Resolution Land Data Assimilation System (HRLDAS, Chen et al. 2007), using the Global Land Data Assimilation System (GLDAS, Rodell et al. 2004) product as the forcing. To have a sufficient spin-up of soil moisture, five one-year cycling were conducted. Specifically, the outermost grid started one day earlier than the period of interest at 0600 UTC (around the middle night the Andes) to provide lateral boundary conditions more consistent with model physics, whereas in the two inner domains the model ran for 36 hours from 0000 UTC on the same day of each case. These WRFCTL simulations are labeled as WLLJ_CTL, SLLJ_CTL, NDRY_CTL, CDRY_CTL and EDRY_CTL, respectively. The first six hours model integration was disregarded to avoid spin-up issues associated with the atmosphere (e.g., Sun and Barros 2012).

In another set of five experiments for the same study cases, the contribution of surface ET is isolated by imposing surface sensible heat variables α, ε, T_{sk}, H, T_{soil} and T_{soilB}[3] exactly the same as in the WRFCTL runs *at every time step*, but with E, such that LE, removed from the atmosphere when they represent a source over the Amazon lowlands. The Amazon lowlands (AMZL) are approximated as the Amazonia region with elevation lower than 500 m delineated in Figure 2.2. These quasi-idealized

[3] In general, for weather-scale simulations, T_{soilB} is set as time invariant.

simulations are referred as STRICT experiments in the sense that the surface sensible heat effects are strictly identical to their WRFCTL counterparts, and named as WLLJ_AMZ, SLLJ_AMZ, NDRY_AMZ, CDRY_AMZ and EDRY_AMZ, respectively. Finally, a separate set of simulations is discussed for which AMZL ET is uniformly varied between 0-200% of the values in the CTL simulations by increments of 20%, which can be viewed as forest thinning (< 100%) and forest densification (> 100%) experiments.

6.3 Results

The evaluation of the WRFCTL simulations against observational datasets is detailed in Section 5a and the supplemental materials of SB14. Here, we focus on the role of surface ET over the AMZL and the subsequent impacts along the EADS.

6.3.1 Atmospheric Adjustment over the Amazon

Without surface ET, daily precipitation over the AMZL decreases significantly in the STRCIT simulations: ~71% in the WLLJ_AMZ and SLLJ_AMZ, ~69% in the NDRY_AMZ, ~62% in the CDRY_AMZ and ~76% in the EDRY_AMZ. As suggested by the hydrostatic surface pressure tendency analysis (right panels, Figure 6.2), these changes should not be *directly* attributed to the artificial mass sink due to the removal of surface moisture supply, because it is trivial in comparison with mass convergence.

During the daytime, more air mass tends to accumulate over the AMZL in the STRICT experiments, but the opposite occurs at night (left panels, Figure 6.2).

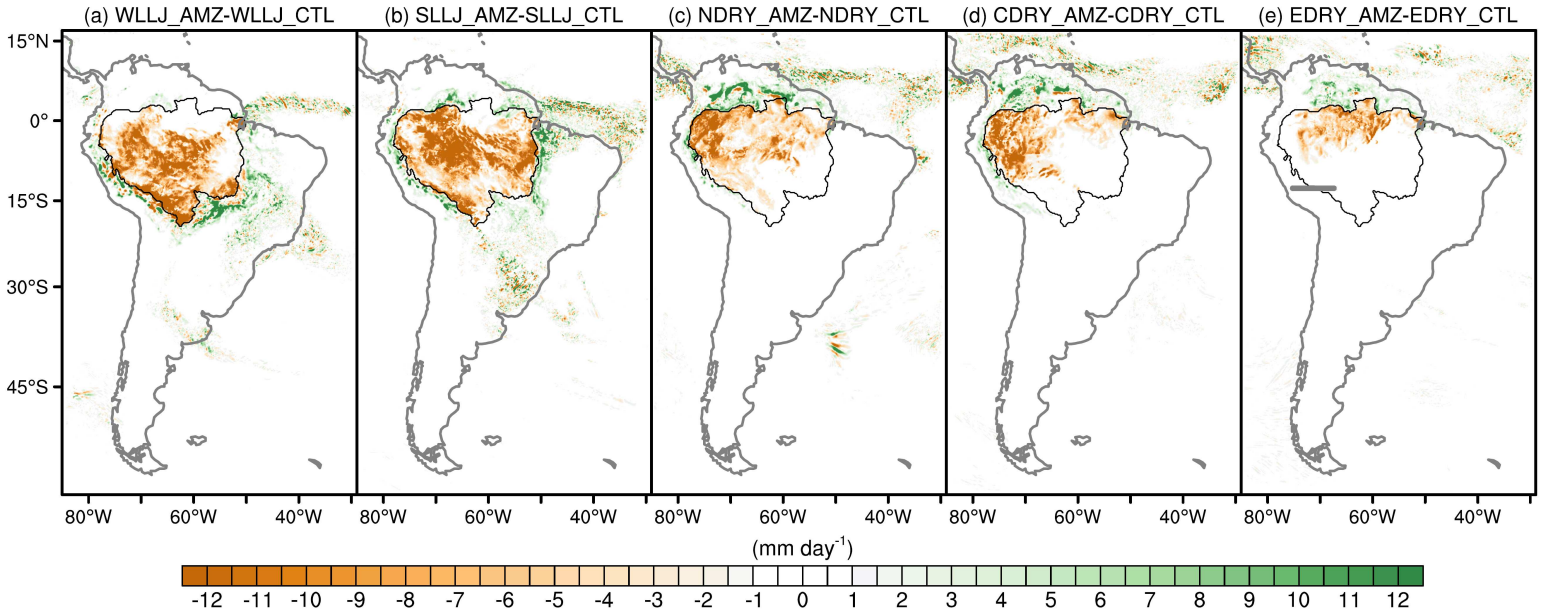

Figure 6.1: Residual of daily precipitation (mm day^{-1}) between the WRFCTL and STRICT simulations (STRICT - WRFCTL) as indicated in the panel titles, with the boundary of the AMZL denoted by the black contour. They are from the outermost domain (Δ_h = 18 km). The gray line from (75˚W, 12.6˚S) to (67˚W, 12.6˚S) in panel (e) marks the cross section for Figures 6.10 and 6.11.

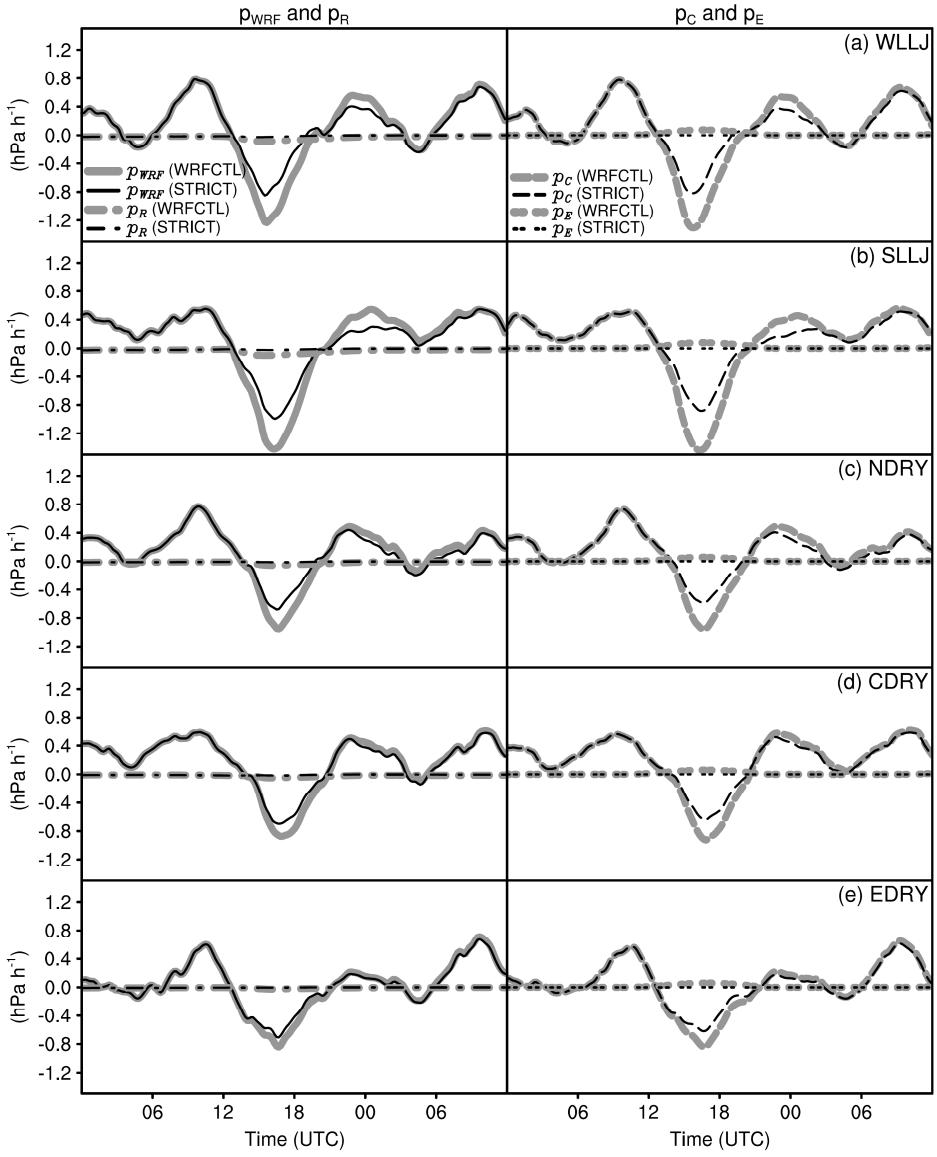

Figure 6.2: Hydrostatic surface pressure tendency (hPa h^{-1}) associated with precipitation ($p_R = -g\rho_l \overline{P}$, dashed-dot), convergence ($p_C = -g\nabla \cdot \int_0^{z_{top}} \rho_a \mathbf{v_H} dz$, dashed) and ET ($p_E = g\rho_l \overline{E}$, dotted), as well as the surface pressure tendency (hPa h^{-1}) diagnosed from the WRF model ($p_{WRF} = \frac{\partial \overline{p_s}}{\partial t}$, solid). They are averaged over the AMZL and from the outermost grid (Δ_h = 18 km), with the thick gray (thin black) for the WRFCTL (STRICT) simulations as indicated in the panel titles.

Depending on the magnitude, precipitation serves as a strong sink of atmospheric moisture over the AMZL (left panels, Figure 6.3). The contribution of surface ET to moisture budget within the AMZL (Figure 6.3, W_E in the right panels) is of the same order of magnitude as precipitation (Figure 6.3, W_R in the left panels), and can exceed moisture convergence from the surrounding regions, including the Atlantic, consistent with previous precipitation recycling studies (e.g. Eltahir and Bras 1994). Compared with the WRFCTL runs, moisture convergence is remarkably weakened when surface ET is eliminated, especially for the WLLJ_AMZ, SLLJ_AMZ and NDRY_AMZ (right panels, Figure 6.3).

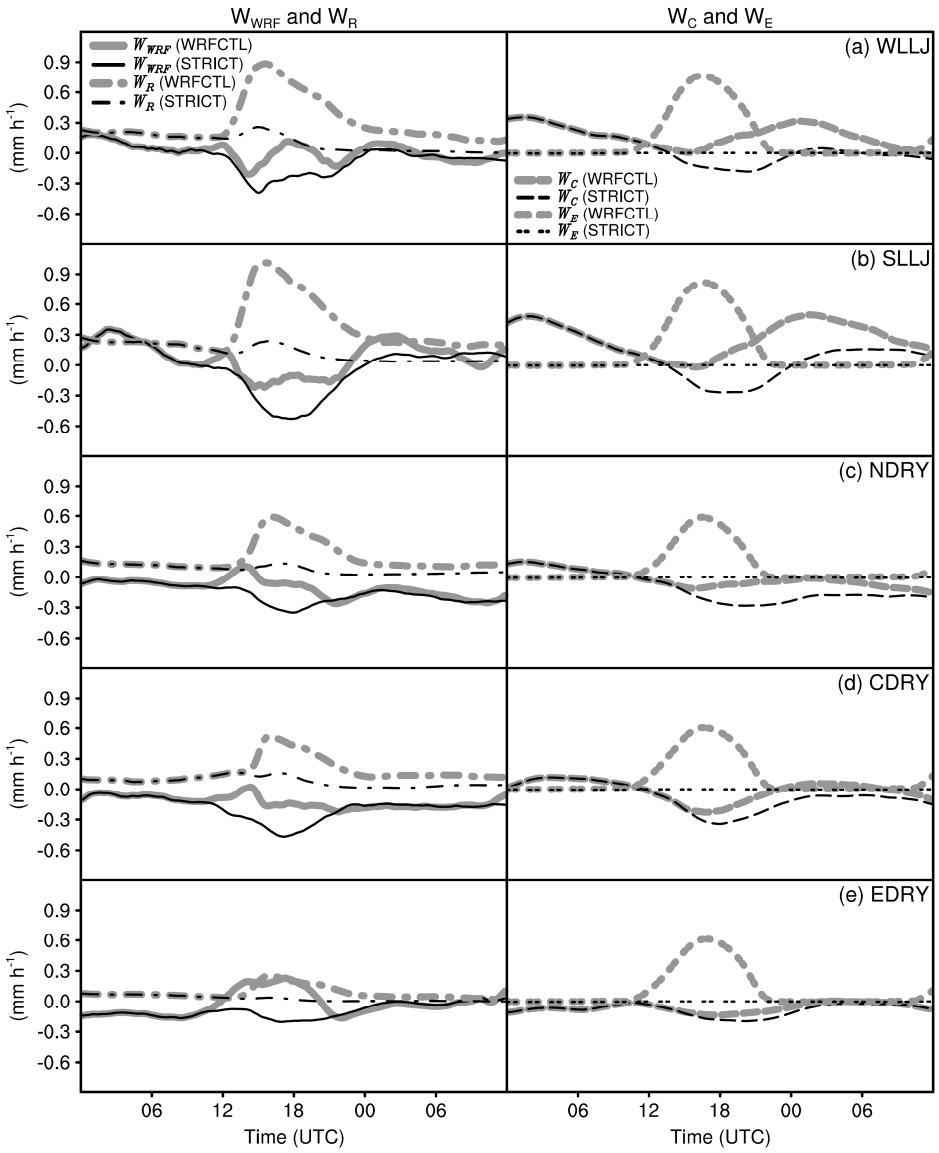

Figure 6.3: Moisture budget (mm h^{-1}) associated with precipitation ($W_R = P$, dashed-dot), convergence ($W_C = -\nabla \cdot \frac{1}{g}\int_0^{p_s} q\mathbf{v_H} dp$, dashed), and ET ($W_E = E$, dotted), as well as the precipitable water tendency (mm h^{-1}) diagnosed from the WRF model ($W_{WRF} = \frac{\partial W}{\partial t}$, solid). They are averaged over the AMZL and from the outermost grid (Δ_h = 18 km), with the thick gray (thin black) for the WRFCTL (STRICT) simulations as indicated in the panel titles.

The coupled variations of air mass and moisture content may be explained by atmospheric circulation adjustments at the continental scale. In the daytime, the lower troposphere over the AMZL is more divergent in the STRICT experiments (top panels, Figure 6.4), whereas convergence anomalies appear in the upper levels (bottom panels, Figure 6.4). These changes span across the entire air column (row 1, Figure 6.5), and probably related to the colder atmosphere in the STRICT simulations (row 2, Figure 6.5). According to temperature tendency analysis, this cooling trend is dominated by suppressed diabatic heating associated with damped convection over the AMZL, although the concurrent modifications of convergence and adiabatic processes counteract this tendency (row 3, Figure 6.5). Because moisture content concentrates at low levels, the result is to strengthen moisture transport from the AMZL toward adjacent regions (row 4, Figure 6.5), including the EADS, the Brazilian Highlands and the mountainous areas in Venezuela, where enhanced precipitation is observed (Figure 6.1). Since rainfall is an important atmospheric moisture sink over the AMZL (left panels, Figure 6.3), the reduction of Amazonian precipitation can be another source of enhanced moisture transport to the surroundings, as manifested by the depth of the atmospheric layer where enhanced moisture loss is prominent (row 4, Figure 6.5).

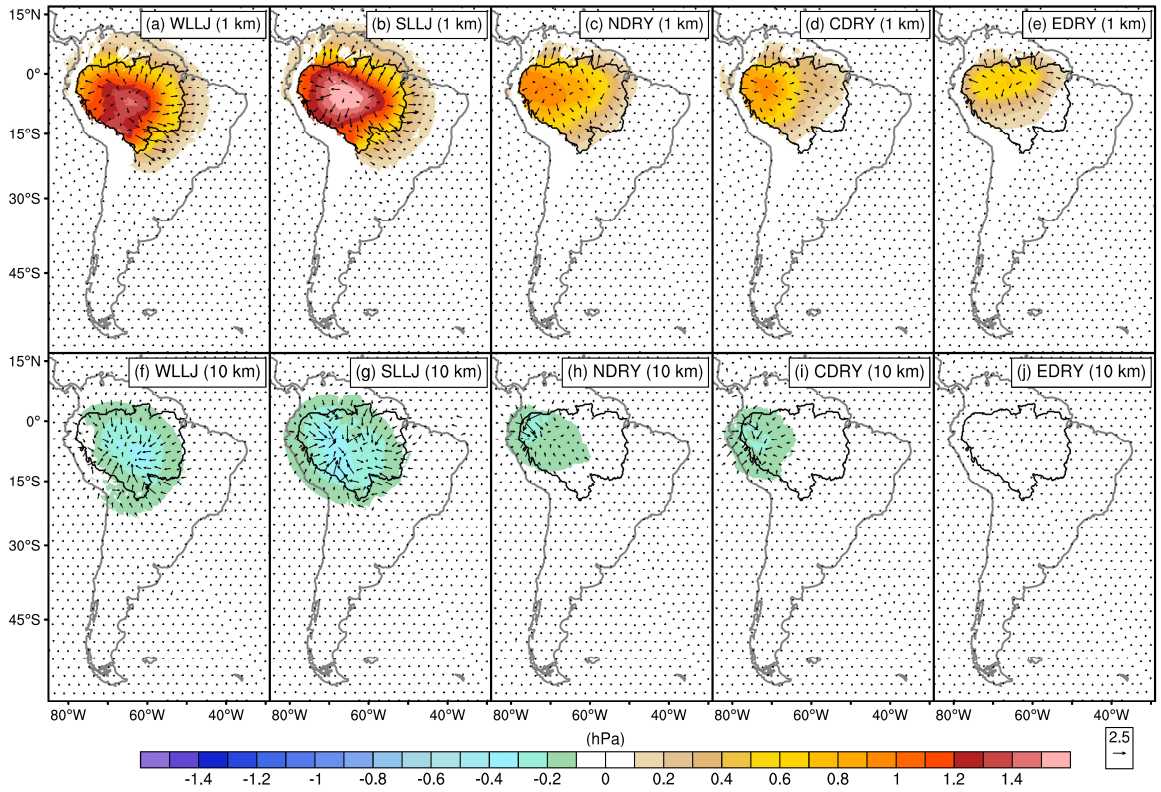

Figure 6.4: Residual of daytime averaged pressure (hPa) between the WRFCTL and STRICT simulations (STRICT - WRFCTL) at 1 (top) and 10 km (bottom) as indicated in the panel titles. The vectors represent the associated wind changes (m s^{-1}). They are from the outermost domain (Δ_h = 18 km), with the boundary of the AMZL denoted by the black contour.

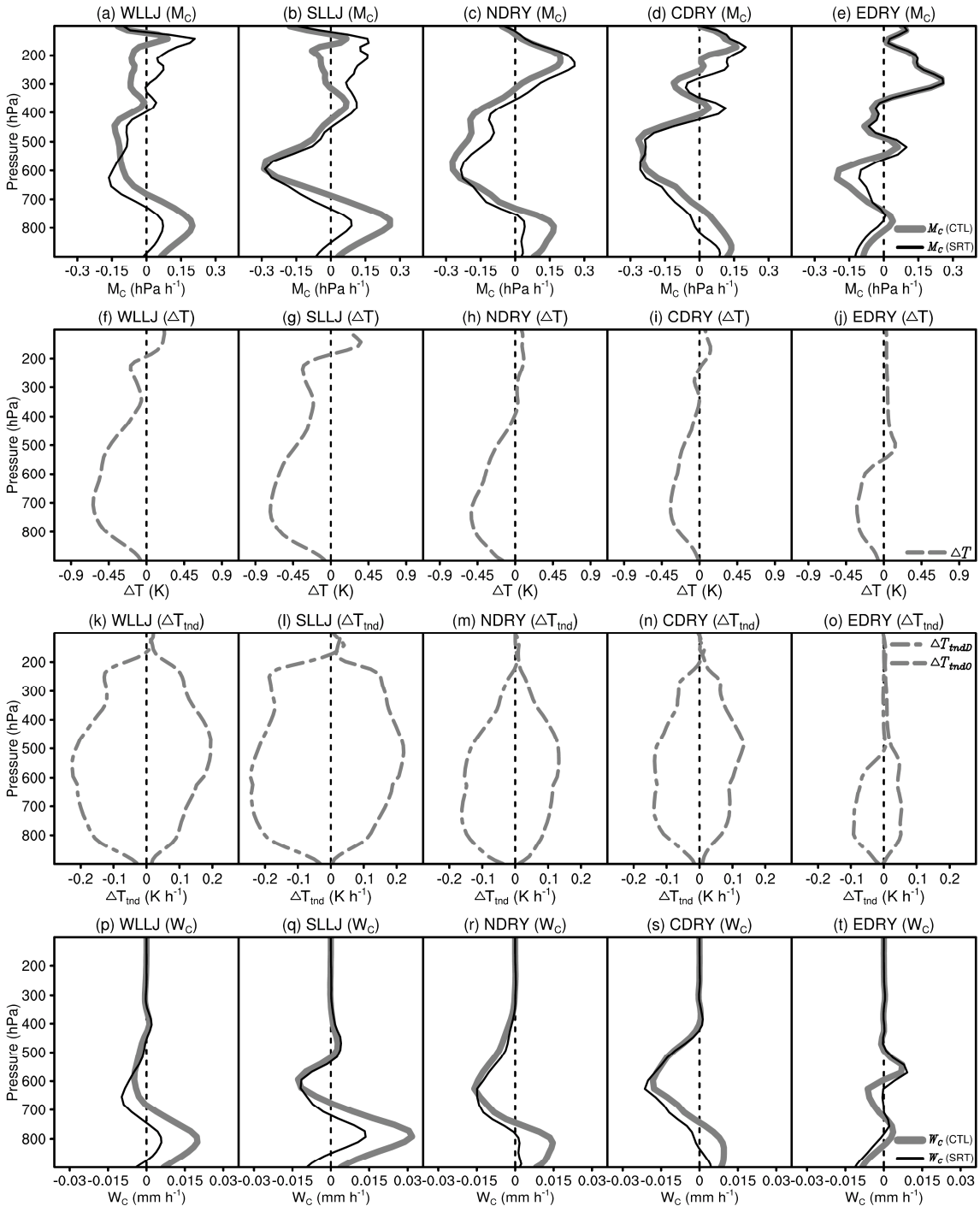
(a) WLLJ (M_C)
(b) SLLJ (M_C)
(c) NDRY (M_C)
(d) CDRY (M_C)
(e) EDRY (M_C)
Pressure (hPa)
M_C (hPa h^{-1})
M_C (CTL)
M_C (SRT)
(f) WLLJ (△T)
(g) SLLJ (△T)
(h) NDRY (△T)
(i) CDRY (△T)
(j) EDRY (△T)
△T (K)
△T
(k) WLLJ ($\triangle T_{tnd}$)
(l) SLLJ ($\triangle T_{tnd}$)
(m) NDRY ($\triangle T_{tnd}$)
(n) CDRY ($\triangle T_{tnd}$)
(o) EDRY ($\triangle T_{tnd}$)
$\triangle T_{tnd}$ (K h^{-1})
$\triangle T_{tndD}$
$\triangle T_{tnd0}$
(p) WLLJ (W_C)
(q) SLLJ (W_C)
(r) NDRY (W_C)
(s) CDRY (W_C)
(t) EDRY (W_C)
W_C (mm h^{-1})
W_C (CTL)
W_C (SRT)

Figure 6.5: The top row panels document the daytime averaged profiles of mass convergence M_c (hPa h^{-1}, solid) from the WRFCTL (CTL, thick gray) and STRICT (SRT, thin black) simulations as indicated in the panel titles. The second row panels are the residual of daytime averaged temperature ΔT (K, dashed gray) between the WRFCTL and STRICT experiments (STRICT - WRFCTL). The third row panels are the same as the second one, but for daytime temperature tendency (K h^{-1}) due to diabatic (ΔT_{tndD}, dashed-dot) and other processes (ΔT_{tndO}, dashed), respectively. The bottom row is the same as the top one, but for moisture convergence W_c (mm h^{-1}). They are averaged over the AMZL and from the outermost grid (Δ_h = 18 km).

The weakening of Amazonian convection is in agreement with the damped convective available potential energy (CAPE) documented in Figure 6.6: without surface ET, CAPE becomes nearly negligible. Generally, as a subcloud-layer air sample is lifted adiabatically and moves along within the boundary layer, its CAPE depends on parcel's entropy, which increases with surface ET, and processes adjusting the temperature of the atmosphere above the air parcel (the colder the upper level air, the larger the CAPE), including radiative cooling, horizontal advection and adiabatic processes associated with large-scale ascent (Emanuel 1994; his Eq. 14.2.13). Because of the magnitude and spatial scale of the large-scale circulation modifications in the STRICT experiments, disentangling the direct influence of surface ET on CAPE from other related feedbacks is not straightforward. However, the results show that MSE (Moist Static Energy) discharge-recharge processes exist over the AMZL at the diurnal time scale (left panels, Figure 6.7). Neglecting small effects arising from loss of mass by precipitation, convection merely transports MSE, instead of being a source or sink (Emanuel 1994).

Consequently, the variations of atmospheric thermodynamic properties in the STRICT experiments may be quantified per the MSE equation (Eq. 3.35), from which the impacts due to horizontal convergence, radiation and surface fluxes can be clearly isolated.

As shown in Figure 6.7 (right panels), when surface ET is removed, causing a decrease in MSE (negative h_{LE}), it is accompanied with an increase in MSE convergence (positive h_C). That is, the reduction of CAPE by preventing surface ET from entering the atmosphere is counteracted by atmospheric circulation adjustments. Given the radiative heating profiles in WRFCTL and STRICT simulations are very close except near the tropopause (not shown), as well as the fact that the surface latent heat effect overweighs horizontal compensation (right panels, Figure 6.7), CAPE decreases over the Amazonia lowlands.

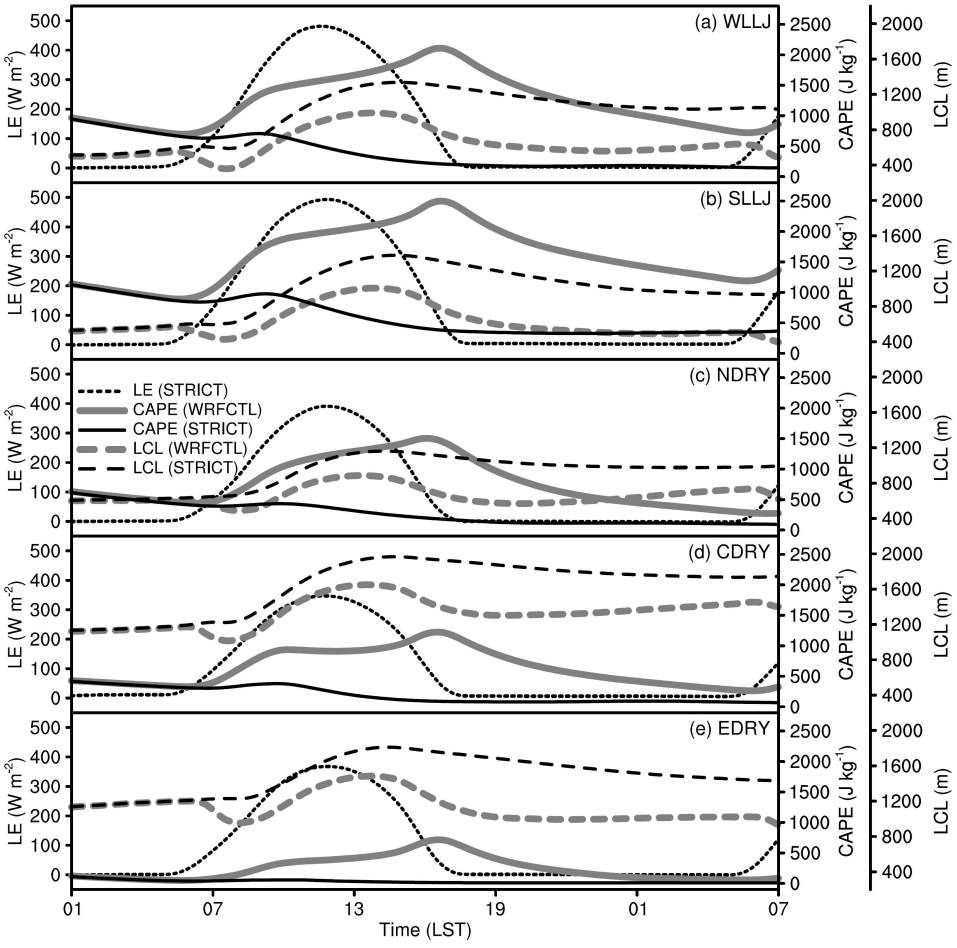

Figure 6.6: Surface latent heat flux *LE removed* from the atmosphere (W m^{-2}, dotted thin black) in the STRICT experiments, as well as maximum CAPE (J kg^{-1}, solid) and LCL (m, dashed) from the WRFCTL (thick gray) and STRICT (thin black) simulations as indicated in the panel titles. They are averaged over the AMZL and from the outermost domain (Δ_h = 18 km).

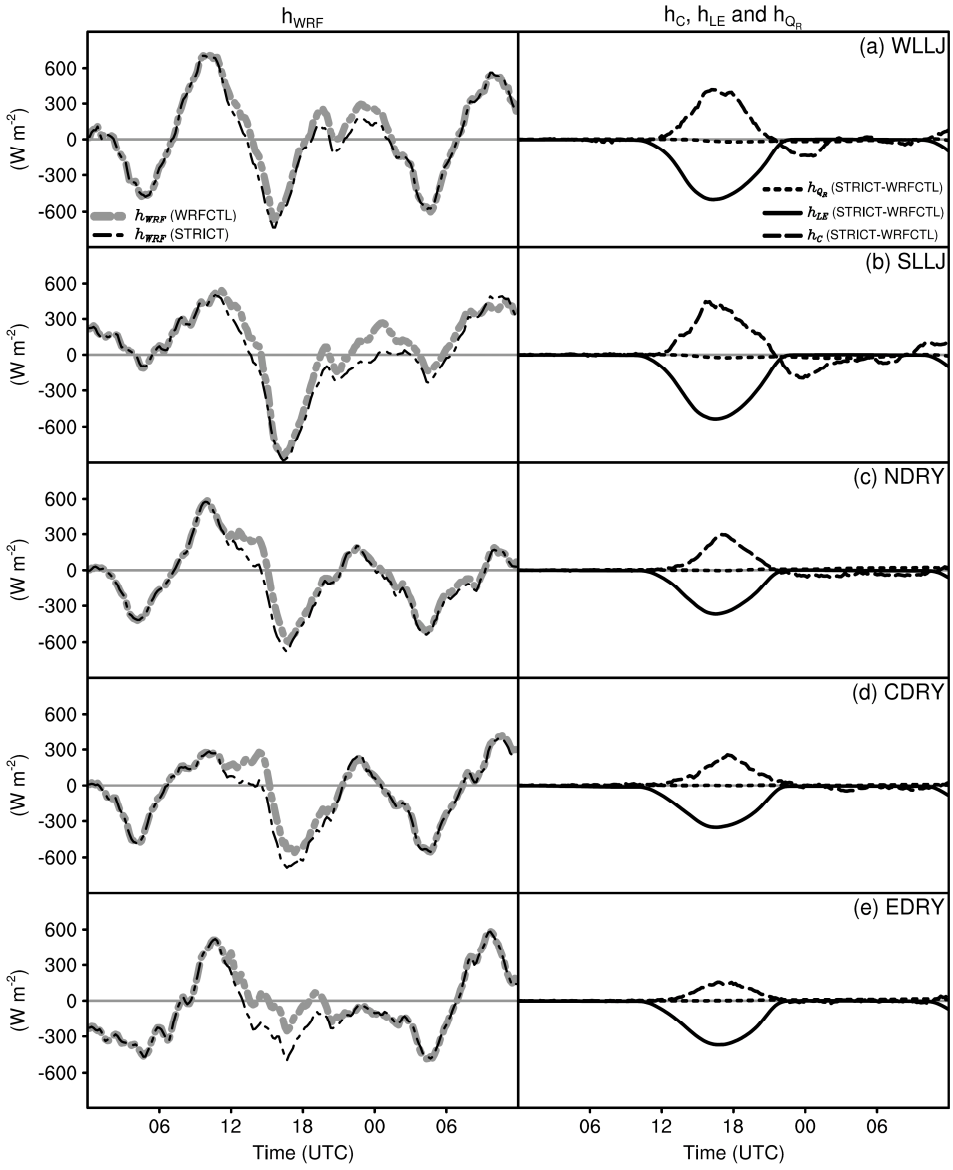

Figure 6.7: The left panels document the MSE tendency $h_{WRF} = \frac{1}{g}\frac{\partial}{\partial t}\int_0^{p_s} h dp$ (W m^{-2}, dashed-dot) diagnosed from the WRFCTL (thick gray) and STRICT (thin black) simulations. The right panels are the difference between the WRFCTL and STRICT experiments (STRICT - WRFCTL) for MSE budget (W m^{-2}) associated with convergence ($h_C = -\nabla \cdot \frac{1}{g}\int_0^{p_s} h\mathbf{v}_\mathbf{H} dp$, dashed), ET ($h_{LE} = LE$, solid) and radiative

forcing ($h_{Q_R} = \frac{c_p}{g}\int_0^{p_s} Q_R dp$, dotted). They are averaged over the AMZL and from the outermost grid (Δ_h = 18 km), with the corresponding experiment indicated in the panel titles.

At night, the dipole structure of convergence-divergence anomalies in the STRICT experiments persists (not shown). Yet, in the proximity of the central EADS, the low level winds tend to be aligned with the topography or oriented eastward away from the Andes (top panels, Figure 6.8). This modification may be related to blocking effects leading to mass accumulation within the concave region roughly between 16°S and 12°N (top panels, Figure 6.8). As demonstrated in Jiang (2006), the blocking magnitude and its location depend on wind fields and atmospheric thermodynamic properties. For the cases examined in this study, and the WLLJ_AMZ and SLLJ_AMZ in particular, the low level pressure anomalies are quite strong (cf. top and bottom panels of Figure 6.8), yielding horizontal pressure gradient force of the same order of magnitude as in the weather systems. Even though the Bolivian high weakens as can be inferred from earlier studies (e.g., Gill 1980; Silva Dias et al. 1983; DeMaria 1985; Figueroa et al. 1995; Lenters and Cook 1997), enhanced nighttime blocking appears to be the key mechanism to explain the low-level wind anomalies associated with the removal of surface ET over the AMZL.

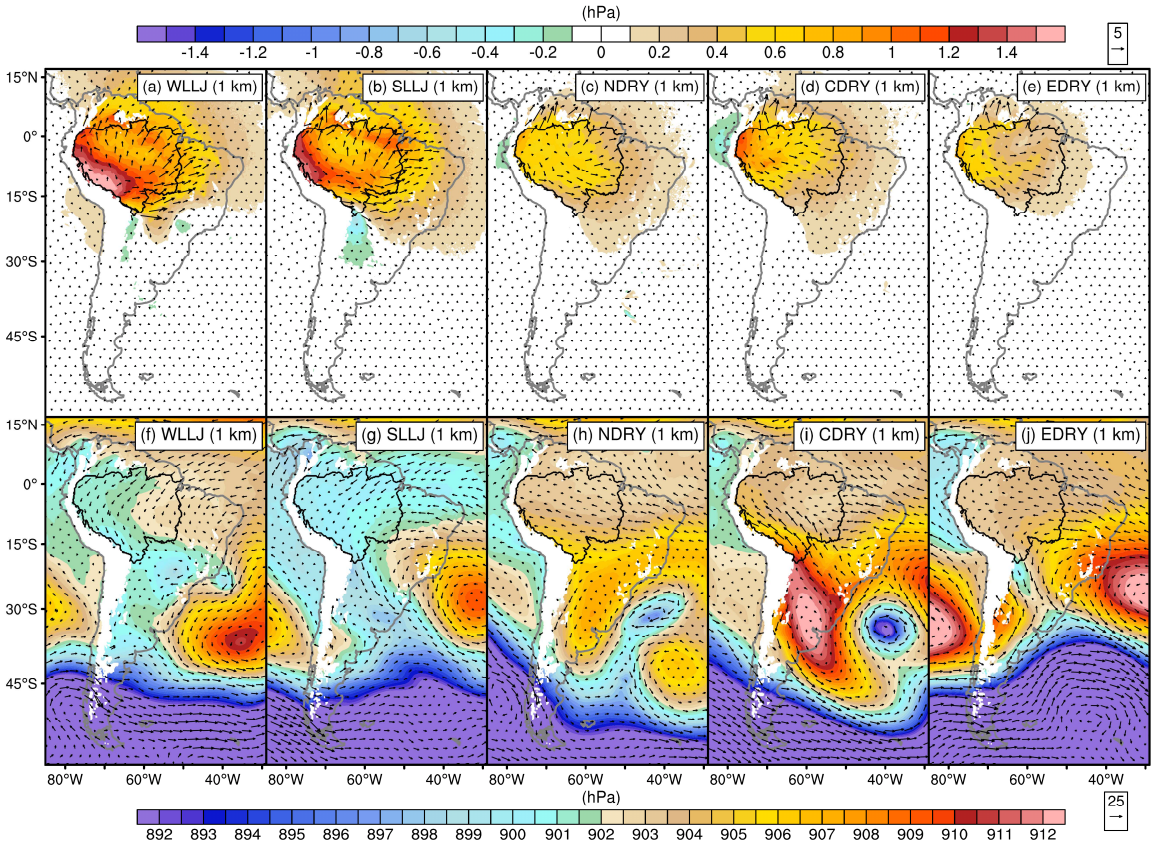

Figure 6.8: The upper panels are the residual of nighttime averaged pressure (hPa) between the WRFCTL and STRICT simulations (STRICT - WRFCTL) at 1 km as indicated in the panel titles, with the vectors showing the associated wind changes (m s^{-1}). The bottom panels document the nighttime averaged pressure (hPa) and wind (m s^{-1}) at 1 km in the WRFCTL runs. They are from the outermost nest (Δ_h = 18 km), with the boundary of the AMZL denoted by the black contour.

6.3.2 Impact on Convection along the Eastern Flanks of the Andes

Moisture convergence over the EADS varies accordingly with the diurnally modified upstream flows. Overall, it increases in the day, but decreases nocturnally in the STRICT experiments (right panels, Figure 6.9), although the timing of this reversal can be associated with the evolution of the lowlands blocking. The humid wet season

atmosphere over the AMZL may further promote this sensitivity, such as in the WLLJ_AMZ (right panel, Figure 6.9a) and SLLJ_AMZ (right panel, Figure 6.9b).

Along with enhanced upslope winds and moisture availability, daytime convection intensifies and cloudiness increases dramatically over the EADS (not shown). Early in the simulation period, precipitation increases (dashed-dot lines, left panels, Figure 6.9), and more water vapor is stored in the atmosphere as suggested by the less negative precipitable water tendency shown in the left panels of Figure 6.9 (solid lines). Thus, it is not surprising that clouds are more widespread at night (cf. Figures 6.10a to 6.10d with 6.10f to 6.10i) even with reduced moisture convergence, since these clouds can be either the daytime remnants or due to more conversion from water vapor to clouds. The lack of sensitivity in EDRY is not unexpected, because almost no clouds form in the control simulation (Figure 6.10e) and the remote moisture source changes very slightly (right panel, Figure 6.9e).

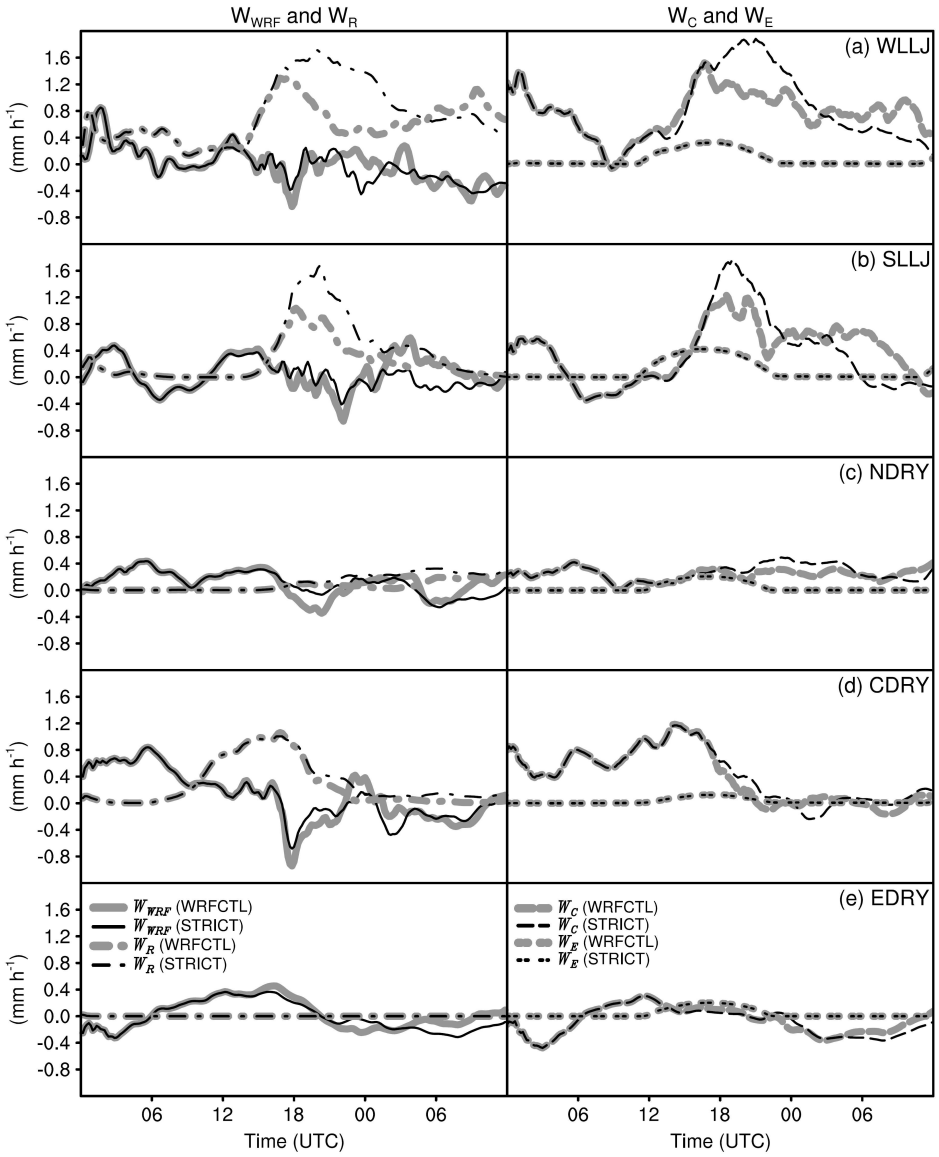

Figure 6.9: The same as Figure 6.3, but from the innermost domain (Δ_h = 1.2 km) and averaged over the EADS.

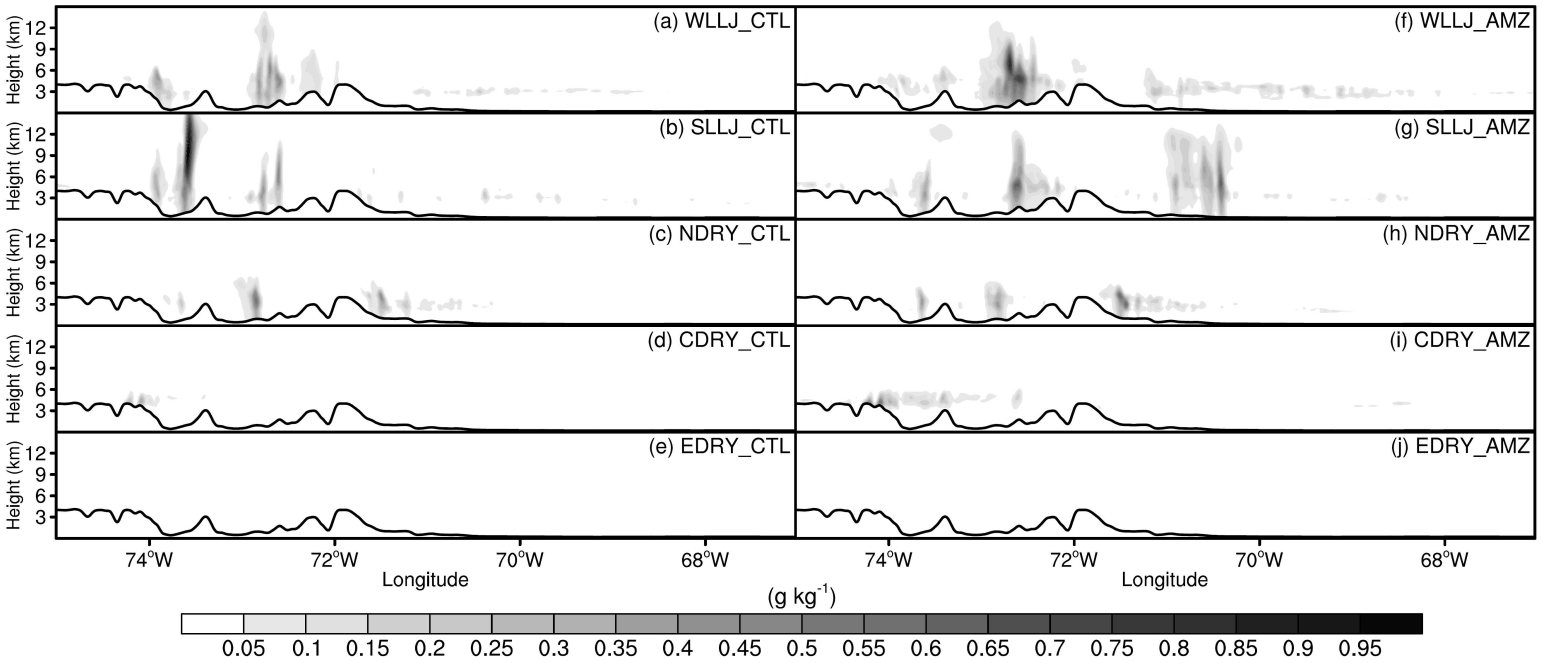

Figure 6.10: Nighttime averaged cloud content (g kg^{-1}, cloud water, ice, snow and graupel) along the cross section denoted by the gray line in Figure 6.1e. As indicated in the panel titles, the left is for the WRFCTL simulations, while the right is for the STRICT experiments. They are from the innermost nest (Δ_h = 1.2 km).

The nighttime convective strength, as measured by the maximum vertical velocity, also weakens, but appears more widespread (cf. Figures 6.11a to 6.11c and Figures 6.11f to 6.11h). The variations of maximum vertical velocity can be further examined by the CFADs (contoured frequency by altitude diagrams, Yuter and Houze 1995) documented in Figure 6.12, where they are presented in the form of $-\left[\log\left(\frac{CFAD}{100}\right)\right]^{-1}$ (CFAD is in percentage) to highlight the extremes. Because greater values of $-\left[\log\left(\frac{CFAD}{100}\right)\right]^{-1}$ correspond to higher frequencies, nighttime convection is more intense in the WLLJ and SLLJ cases (cf. Figures 6.12a and 6.12b with 6.12f and 6.12g), while differences are minor or negligible otherwise (cf. Figures 6.12c to 6.12e and 6.12h to 6.12j).

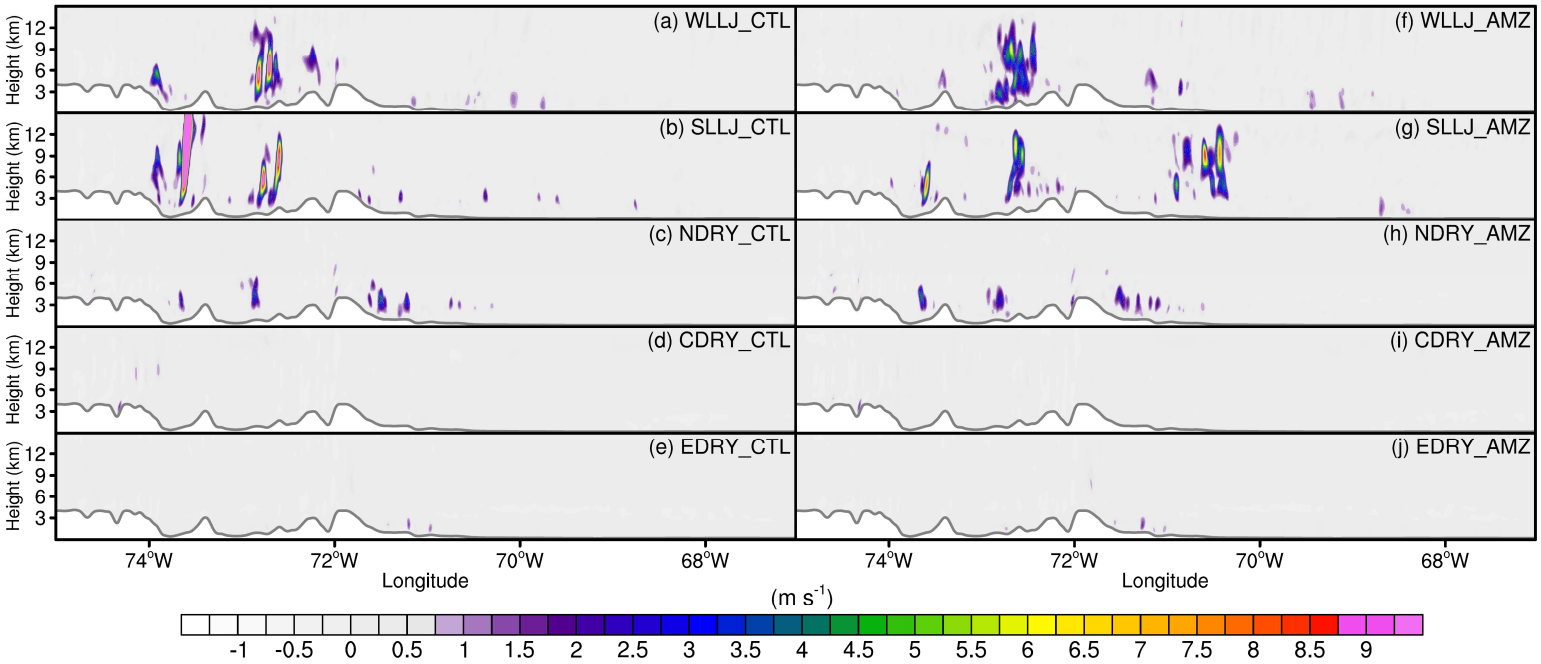

6.11: Nighttime maximum vertical velocity (m s^{-1}) along the cross section denoted by the gray line in Figure 6.1e. As indicated in the panel titles, the left is for the WRFCTL simulations, while the right is for the STRICT experiments. They are from the innermost grid (Δ_h = 1.2 km).

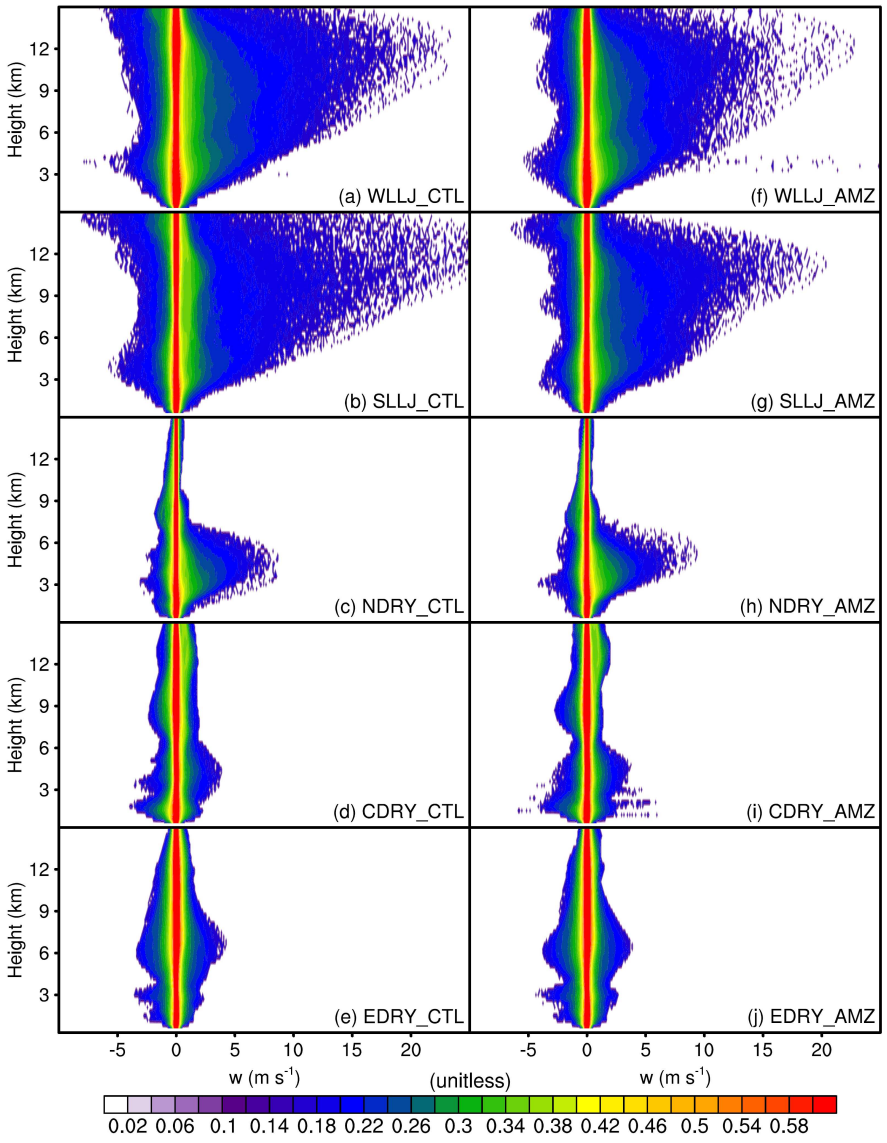

Figure 6.12: Nighttime contoured frequency by altitude diagrams (CFADs) of vertical velocity (m s^{-1}) over the EADS from the innermost domain (Δ_h = 1.2 km). To emphasize the frequency at extreme values, they are presented in the form of $-\left[\log\left(\frac{CFAD}{100}\right)\right]^{-1}$ with CFAD in percentage. As indicated in the panel titles, the left is for the WRFCTL simulations, while the right is for the STRICT experiments.

A quantitative estimate of convective fraction σ may be achieved as follows. Consider a general quantity ψ within a convective region, its vertical eddy flux can be written as (Arakawa et al. 2011)

$$\overline{w'\psi'} = \overline{w\psi} - \overline{w}\,\overline{\psi} = \frac{\sigma}{1-\sigma}(w_c - \overline{w})(\psi_c - \overline{\psi}), \tag{6.2}$$

where subscript c denotes average within the clouds, and the overbar indicates the regional mean. To make the problem more tractable, instead of for convective updrafts, σ here is defined as the fraction occupied by both convective updrafts and downdrafts[1]. Using tilde for environmental values, the water vapor mixing ratio r and total water mixing ratio r_T follows

$$\overline{r} = (1-\sigma)\tilde{r} + \sigma r_t \tag{6.3}$$

$$\overline{r_T} = \tilde{r} + \sigma(r_{T_t} - \tilde{r}) \tag{6.4}$$

and the corresponding eddy fluxes are

$$\overline{\rho}\,\overline{w'r'} = \overline{\rho}\left(\overline{wr} - \overline{w}\,\overline{r}\right) = \frac{1}{1-\sigma}(M_t - \overline{\rho}\sigma\overline{w})(r_t - \overline{r}) \tag{6.5}$$

$$\overline{\rho}\,\overline{w'r_T'} = \overline{\rho}\left(\overline{wr_T} - \overline{w}\,\overline{r_T}\right) = \frac{1}{1-\sigma}(M_t - \overline{\rho}\sigma\overline{w})(r_{T_t} - \overline{r_T}), \tag{6.6}$$

[1] As detailed in Emanuel (1994, his Figures 15.7 and 15.8), the mass flux estimation can be much more accurate for total cumulus than for updrafts.

in which subscript t denotes quantities of the combined updrafts and downdrafts and $M_t = \sigma \overline{\rho} w_t$ is the corresponding mass flux. The latter quantity can be obtained as per (Emanuel 1994)

$$\frac{\partial \overline{h_{lv}}}{\partial t} + \overline{\mathbf{v_H}} \cdot \nabla \overline{h_{lv}} + \overline{w} \frac{\partial \overline{h_{lv}}}{\partial z} - Q_R = \frac{M_t}{\overline{\rho}} \frac{\partial \overline{h_{lv}}}{\partial z}, \tag{6.7}$$

where $h_{lv} \approx c_{pd} T + gz - L_{v0} l$ (L_{v0} is the latent heat of vaporization at 0°C and l is the liquid water content) is the liquid water virtual static energy, neglecting the effect of water substance on heat capacity and density, and z is model height. Equations (6.3) to (6.6) form a closed system with four unknowns: σ, $\tilde{r}$, r_t and r_{T_t}. After some mathematical manipulation, a simple solution can be obtained for moist convective fraction

$$\sigma = \frac{M_t}{\overline{M} + \overline{\rho} C}, \tag{6.8}$$

where $\overline{M} = \overline{\rho} \overline{w}$ represents the mean large-scale mass flux and $C = \frac{\overline{w' r_T'} - \overline{w' r'}}{\overline{r_T} - \overline{r}}$ is the specific condensate eddy flux, with r_{cnd} denoting total condensate mixing ratio, including rain water, cloud water, cloud ice, snow and graupel. Note that σ only applies to regions with condensate, else Eqs. (6.3) and (6.5) would be equal to Eqs. (6.4) and (6.6), and the system would not be closed anymore. Further, its validity is limited to

the mid-upper troposphere, since one assumption behind Eq. (6.7) is that detrainment occurs at neutral buoyancy, which must break down near the surface, where negatively buoyant air detrains into the boundary layer (Emanuel 1994). In addition, the estimate of σ is most reliable when condensate concentrations are not very low, such that Eqs. (6.5) and (6.6) provide distinct information.

The convective fraction, after applying a threshold of $\overline{q_T}$ as 10^{-5} g kg^{-1}, is shown in Figure 6.13 (leftmost column) for the WLLJ, SLLJ and NDRY cases. Because of limited clouds, almost no atmospheric layers meet this requirement in CDRY, and EDRY fails to have $\overline{q_T}$ beyond this threshold everywhere (not shown). Nevertheless, nocturnal convection does occur more widely in the STRICT simulations (Figures 6.13a, 6.13f and 6.13k). According to Eq. (6.8), the expansion of convective regions could be simply related to enhanced convective mass flux M_t, e.g., in the NDRY_AMZ (Figure 6.13l)[2]. Yet, it is generally suppressed in the WLLJ_AMZ (Figure 6.13b) and SLLJ_AMZ (Figure 6.13g) below around 9 km. For the mean mass flux $\overline{M}$, even less consistency exists: increases above but decreases below ~9 km in the WLLJ_AMZ (Figure 6.13c); weakens throughout the entire troposphere in the SLLJ_AMZ (Figure 6.13h); and amplifies at low

[2] The relatively cold lower troposphere in the NDRY_AMZ (not shown) might be responsible for its enhanced M_t, since cooling decreases the moisture threshold necessary to sustain convection (Neelin et al. 2003).

levels in the NDRY_AMZ (Figure 6.13m). The magnitude of $\overline{\rho C}$ in the denominator of Eq. (6.8), however, is substantially lower and the vertical profile is consistent among all STRICT experiments as compared to WRFCTL. More importantly, the change in $\overline{\rho C}$ from the WRFCTL to STRICT is one order of magnitude greater than that for $\overline{M}$ (cf. Figures 6.13c, 6.13h and 6.13m with 6.13d, 6.13i and 6.13n), *apparently* indicating the predominant influence of the local condensate eddy flux on nocturnal convective fraction over the EADS.

Since $\sigma << 1$ (leftmost panels, Figure 6.13), one may also approximate it using Eqs. (6.3), (6.4), (6.7) and the relations

$$\overline{\rho w' r'} = \overline{\rho}\left(\overline{wr} - \overline{w}\,\overline{r}\right) = M_t (r_t - \overline{r}) \tag{6.9}$$

$$\overline{\rho w' T'} = \overline{\rho}\left(\overline{wT} - \overline{w}\,\overline{T}\right) = M_t (T_t - \overline{T}) \tag{6.10}$$

$$\overline{\rho w' T_\rho}' = \overline{\rho}\left(\overline{wT_\rho} - \overline{w}\,\overline{T_\rho}\right) = M_t (T_{\rho_t} - \overline{T_\rho}) \tag{6.11}$$

$$T_{\rho_t} = T_t \frac{1 + \frac{r_t}{\varepsilon}}{1 + r_{T_t}}, \tag{6.12}$$

where T_ρ stands for density temperature and $\varepsilon = \frac{R_d}{R_v}$, with R_d and R_v as the gas constant for dry air and water vapor, respectively. The corresponding convective fraction

$$\sigma = \frac{\overline{r_{cnd}}}{r_{cnd\,t}} \tag{6.13}$$

is almost identical to that derived from Eq. (6.8) (not shown). This is not unexpected, because the only additional but legitimate assumption in Eqs. (6.9) to (6.12) is that σ is much less than unity (Figures 6.13a, 6.13h and 6.13o). The absence of condensate eddy flux in solution (6.13), however, advocates that the associated transfer of buoyancy, which can be non-insignificant in heavily precipitating systems (Emanuel 1986), should not be fundamental to the widely spread convection in the STRICT experiments, consistent with the mild or slight nocturnal precipitation in the WLLJ, SLLJ and NDRY (dashed-dot lines, left panels, Figures 6.9a, 6.9b and 6.9c). Further, if the cumulus buoyancy B is evaluated as (Houze 1993)

$$B \approx g\left(\frac{T'}{\overline{T}} - \frac{p'}{\overline{p}} + 0.61r' - r_{cndt}\right), \tag{6.14}$$

the last term is one order of magnitude smaller than the first and second terms for the cases involved in this study (not shown), implying that the condensate loading effect is trivial as well. According to these observations, we postulate that, rather than being the direct cause, the appearance of condensate related variables and terms in relations (6.8) and (6.13) stems from other processes modulating condensation inside the updrafts and downdrafts.

Following Yanai et al. (1973), the bulk entrainment/detrainment rate might be defined as

$$\lambda = \frac{1}{M_t}\frac{dM_t}{dz}. \tag{6.15}$$

As reported in Figures 6.13e, 6.13l and 6.13s and below ~9 km, its absolute value is always greater in the STRICT, indicating stronger mixing with the environment. The low-level total cumulus condensate in the STRICT simulations, however, is not less than its counterpart in the WRFCTL runs (Figures 6.13f, 6.13m and 6.13t). This suggests that evaporation in the lower troposphere is weaker in the STRICT, as collaborated by the higher relative humidity (RH) shown in the rightmost panels of Figure 6.13. Given evaporatively driven downdrafts tend to cut off updrafts, suppressing convection, it is argued that the widespread nocturnal convection over the EADS in the STRICT experiments presented in this chapter is due to the reduction of low-level evaporation, which modifies condensation insides the cumulus clouds [see relations (6.8) and (6.13)].

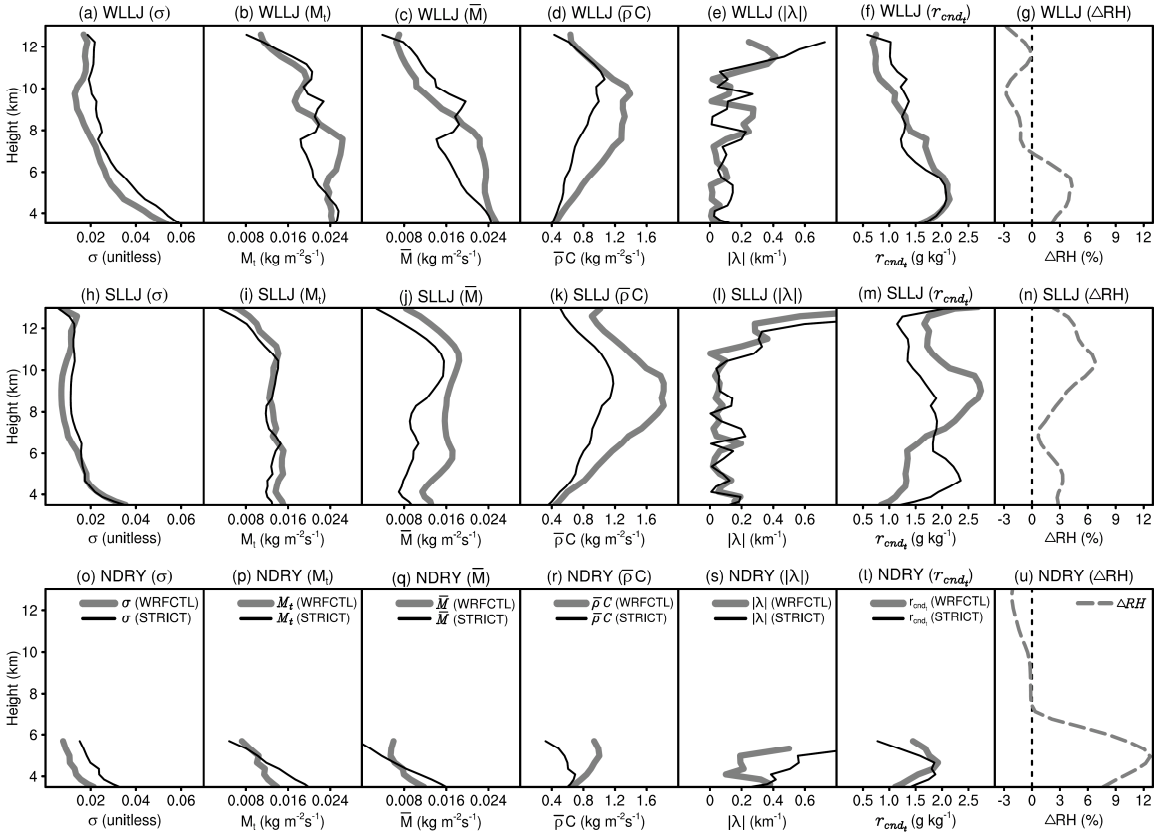

Figure 6.13: Nighttime averaged vertical profiles of convective fraction σ (unitless, a, h and o), cumulus mass flux M_t (kg m^{-2}s^{-1}, b, i and p), mean mass flux $\overline{M}$ (kg m^{-2}s^{-1}, c, j and q), $\overline{\rho C}$ (kg m^{-2}s^{-1}, d, k and r), entrainment/detrainment rate $|\lambda|$ (km^{-1}, e, l and s) and r_{cndt} (g kg^{-1}, f, m and t) from the WRFCTL (thick gray) and STRICT (thin black) simulations as indicated in the panel titles. The relative humidity differences ΔRH (%) between the WRFCTL and STRICT experiments (STRICT - WRFCTL) are documented in the rightmost panels (g, n and u). They are averaged over the EADS and from the innermost nest (Δ_h = 1.2 km).

6.4 Conclusions and Discussion

Following the quasi-idealized framework proposed by SB14 (see their Sections 2 and 3 for details), the role of Amazonian surface ET on moisture transport and convection along the eastern flanks of the Andes (EADS) was isolated. Specifically, over the Amazon lowlands (AMZL) and *at each time step*, surface sensible heat effects are specified identically to the reference runs, whereas surface moisture and latent heat fluxes are removed from the atmosphere when they represent a source. Compared with earlier studies, either relying on perturbed soil moisture or through land-use land-cover change, complications from other modifications of land surface properties, such as albedo, surface roughness and Bowen ratio, are excluded.

Simulations of frequently observed weather conditions in South America, using ARW-WRF3.4.1 down to 1.2 km grid spacing, show that without surface ET daily precipitation within the AMZL drops by up to ~75%. This dramatic influence is attributed to the dipole structure of convergence-divergence anomalies over the AMZL, primarily due to the appreciable troposphere cooling induced by suppressed convection. Diurnal evolution of moist static energy over the AMZL indicates that although the related large-scale circulation change tends to compensate for CAPE, elimination of surface ET removes it more efficiently. Accompanied with the large-scale atmospheric adjustment, moisture transport toward surrounded regions is largely enhanced. In the

adjacent mountainous areas, including the EADS to the west, the Brazilian Highlands to the east and the northern mountainous region in Venezuela, daily rainfall nearly doubles.

Because of the concave shape of the Andean mountain range, the enhanced low-level divergence in the STRICT experiments with surface ET removed from the atmosphere promotes air mass accumulation to the east of the central EADS. This perturbation develops with time and becomes sufficiently strong around nightfall. Model results suggest that it can produce significant eastward low-level pressure gradient force, rendering wind currents more away from the Andes, as well as attenuated nocturnal moisture convergence. Not surprisingly, convection over the EADS varies accordingly, intensifying during the day and weakening at night. However, nocturnal convective motion is more widespread in the STRICT experiments. Simple analytical solutions of convective fraction (Eqs. 6.8 and 6.13) and the relevant analyses (Figure 6.13) reveal that this feature may be related to the reduction of lower troposphere evaporation. This conclusion is confirmed by the examinations of maximum convective inhibition (CIN), which merely changes slightly over the EADS (not shown).

As surface ET is crucial for the moisture budget within the AMZL in both austral summer and winter (right column, Figure 6.3), another group of simulations at 18 km grid spacing (outermost domain in Figure 2.2) were conducted to further understand its

impact on EADS. Preferring rainfall as a simple measure, the WLLJ was selected, because EADS rainfall in the WLLJ_AMZ increases in the daytime, but decreases at night as compared with the WLLJ_CTL. These set of experiments are configured the same as the STRICT simulations, except that, instead of removing surface ET completely, the surface flux is made to vary between 0 and 200% of the value in the WRFCTL runs at 20% increments to represent forest thinning and densification. The results show that precipitation over the AMZL is monotonically proportional to the surface ET (Figure 6.14a), increasing by as much as ~60% for the ET doubling experiment (200ET). Over the EADS, reduced Amazonian surface ET promotes (suppresses) EADS precipitation in the daytime (at night) by about 30% relative to the WRFCTL simulations (Figure 6.14b). When specified ET over AMZL is larger than WRFCTL, the opposite takes place: less rainfall during daytime, and an increase at night. To evaluate this relationship in a more realistic manner, another exploratory experiment was carried out. This simulation (WLLJ_RLXSH) is identical to the WLLJ_AMZ (000LE), but allows the surface sensible heat effects to adjust freely. As illustrated by the dashed gray line in Figure 6.14, similar responses were produced, although slightly weaker. The differences between the WLLJ_AMZ and WLLJ_RLXSH, however, should not be primarily associated with modifications of atmospheric radiation, since, except near the surface, the radiative heating rate are roughly the same in these two experiments (Figure 6.15). Rather, this

may be attributed to the relatively enhanced thermal circulations over the AMZL in the latter, as the daytime surface skin temperature is ~1-2 degrees warmer (not shown). Nevertheless, these experiments demonstrate that even small changes in surface ET over the AMZL are sufficient to impact convection over the EADS, and the connection of these two regions is robust.

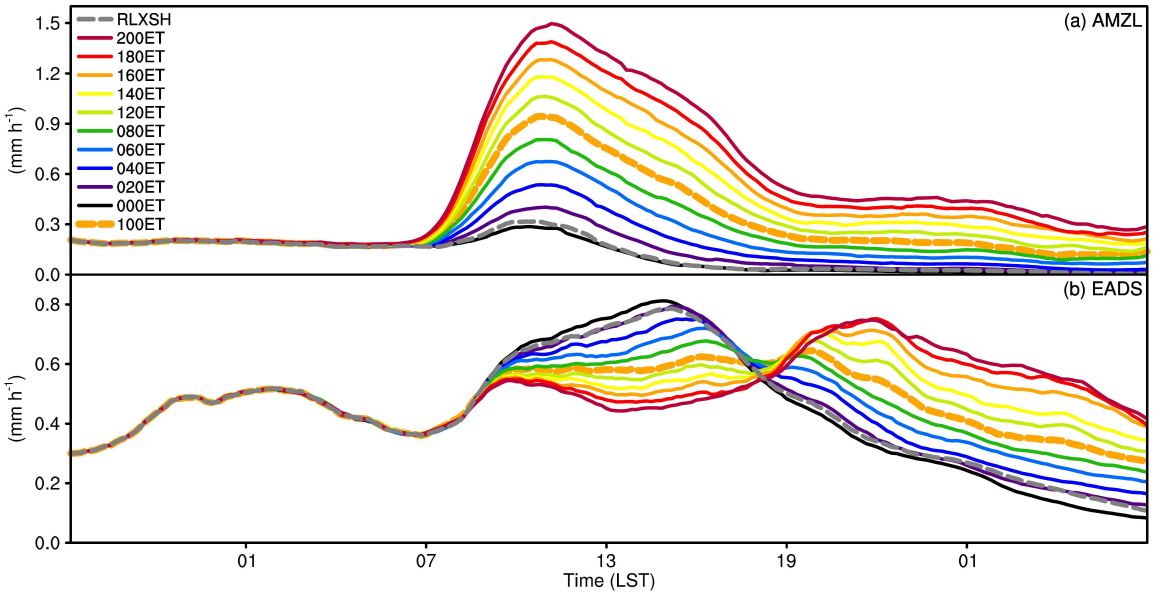

Figure 6.14: Rain rate (mm h^{-1}) from simulations with varied surface ET over the AMZL as indicated in the legend. For instance, 020ET denotes the experiment with surface ET as 20% of the WRFCTL run, while 100LE (000LE) is the WLLJ_CTL (WLLJ_AMZ) simulation, with the dashed gray for the WLLJ_RLXSH. The top panel is averaged over the AMZL, while the bottom panel is the mean along the EADS. They are for the WLLJ and from the outermost grid (Δ_h = 18 km).

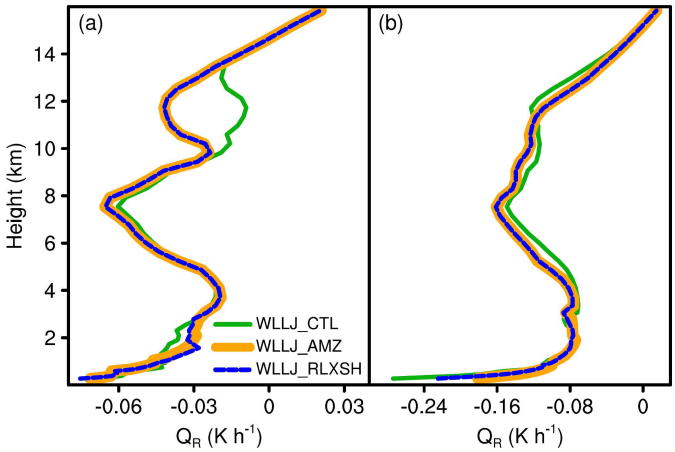

Figure 6.15: (a) Daytime and (b) nighttime radiative heating rate (K h^{-1}) from the WLLJ_CTL (solid thin green), WLLJ_AMZ (solid thick orange) and WLLJ_RLXSH (dashed thin blue). They are averaged over the AMZL and from the outmost domain (Δ_h = 18 km).

7 Concluding Remarks

7.1 Research Summary

The subject matter of this dissertation is the role of surface ET on moist convection along the eastern flanks of the Andes (EADS), both from "local" surface moisture supplies over the EADS, and from "remote" upwind Amazonian ET.

Compared with prior studies, the focus here is on the physical processes (mechanical and thermodynamic) by which surface latent heat fluxes directly impact the lower troposphere over complex terrain. Through the development of an assembled land surface, complications from other land surface properties (e.g., albedo, surface roughness and Bowen ratio) were side-stepped. The assembled land surface model was derived by combining and simplifying the moderate-complex Noah land surface model and the revised MM5 surface layer parameterization (see Chapter 2). Furthermore, the ARW-WRF3.4.1 was substantially modified to accommodate external data streams at sub-second frequency.

The WRFCTL simulations down to 1.2 km grid spacing showed reasonable agreement with various observational datasets, lending confidence for further analyses of model results. The events simulated are based on the climate of South America and covers a wide spectrum of weather conditions of this continent.

The time step output of surface sensible heat variables from the WRFCTL were subsequently imposed in the STRICT experiments, with surface ET eliminated either over the EADS or the Amazon lowlands (AMZL).

Quantifications of model results mainly rely on hydrostatic surface pressure tendency, moisture budget, apparent heat source and apparent moisture sink casted into σ-coordinates, temperature tendency over irregular regions and column integrated moist static energy equation.

Besides numerical analysis, a simple analytical solution of convective fraction is proposed to explain the widespread nighttime convection over the EADS when the surface ET in the Amazon is prevented from entering the Atmosphere. Limitations of this analytical approach are emphasized.

7.2 Research Findings

7.2.1 Role of Local Surface ET on Moist Convection over the EADS

- Energy balance analysis indicates that local surface ET along the EADS influences moist convection primarily through its impact on conditional instability, because it acts as an important source of moist entropy in this region. The energy available for convection decreases by up to ~60% when the ET contribution is withdrawn.

- In contrast, when convective motion is not thermally driven, or under conditionally stable conditions, latent heating from the land surface becomes secondary.
- At the scale of the Andes proper, removal of surface ET weakens upslope flows by increasing static stability of the lower troposphere, as the vertical gradient of water vapor mixing ratio tends to be less negative. Consequently, moisture convergence is reduced over the EADS.
- In the absence of local surface ET, this process operates in concert with damped convective energy, suppressing cloudiness, and decreasing daily precipitation by up to ~50% in the simulations presented here.

7.2.1 Role of Remote Surface ET on Moist Convection over the EADS

- When the surface ET is eliminated over the Amazon lowlands (AMZL), the results show that daily precipitation within the AMZL drops by up to ~75%, but nearly doubles over the surrounded mountainous regions.
- This dramatic influence is attributed to the dipole structure of convergence-divergence anomalies over the AMZL, primarily due to the considerable cooling of the troposphere associated with suppressed convection.

- Further analysis of moist static energy indicates that although the related large-scale circulation change tends to compensate for convective available potential energy (CAPE), elimination of surface ET is more effective on reducing CAPE.
- Because of the concave shape of the Andean mountain range, the enhanced low-level divergence promotes air mass accumulation to the east of the central EADS. This perturbation becomes sufficiently strong around nightfall and produces significant eastward low-level pressure gradient force, leading to wind currents more away from the Andes.
- Moisture convergence and convection over the EADS vary accordingly, strengthened in the day but attenuated at night. The nocturnal convective motion, however, is more widespread. A simple analytical solution of convective fraction suggests that this feature may be related to buoyancy transfer induced by vertical eddy flux of total condensate.
- Additional exploratory experiments demonstrate that the connection between the AMZL and EADS is robust.

7.3 Discussion and Recommendations for Further Research

One of the big challenges in completing this research was the computational demand, especially regarding the specification of boundary conditions in the case of STRICT experiments (every 0.2 s) and the analysis of the simulations that mount to

nearly 50 Tb. The STRICT simulations can be investigated in a more affordable and theoretical framework, for example conducting highly idealized simulations using a Gaussian-type mountain or mimicking a plateau similar to the Altiplano. However, it is worthy to note that these experiments may be limited to quasi-2D configurations and for the role of local ET only, because it is not that possible to specify simplified but reasonable background wind fields for the complex weather systems over South America.

The STRICT simulations did not allow examination of the adjustment of the surface sensible heat fluxes, and thus radiative forcing partitioning, for the specified changes in latent heat. This could be accomplished easily by slightly revising the STRICT experiments, e.g., releasing the control of surface sensible heat variables, and extending the duration of the simulations to examine the impact of land-use land-cover change at seasonal and longer time-scales in regional climates.

The robust connection between the AMZL and EADS indicates that improved representation of upstream surface fluxes can potentially enhance model performance over the Andes. Recently, the global canopy height observations became available (Leafsky 2010). One possible continuation of this work is to incorporate these observations into the WRF model, as the surface fluxes could be more accurately calculated using the displacement heights derived from the observations. This work is

being conducted by the author and his advisor, and collaborating with the research scientists at NCAR.

Another salient feature of the South America continent is the Brazilian Highlands to the east. Consequently, one may wonder whether the relevant effects are important. Since pasture and cropland expansion in this region has been substantial, another interesting direction to further explore may be related with LULC change over the Cerrado.

A key result of this research was to demonstrate the role of surface ET on Andes rainfall beyond that of moisture budget studies by elucidating the mechanisms by which it affects atmospheric stability at the mountain range scale. Clearly, in practice, actual LULC change is not expected to follow contour lines and to be uniform in space and time, but rather to exhibit strong heterogeneity. Therefore, in order to fully understand the impacts, or indeed to predict the impacts of ongoing or upcoming altitudinal ecosystem shifts or land-use change, more specific targeted numerical experiments would be necessary. Finally, this research elucidated quantitatively for the first time the contribution of surface ET in the Amazon lowlands on Central Andes rainfall. This means that thinning or LULC change in the Amazon such as that currently planned (e.g. Walker et al. 2011) can impact downstream freshwater resources in Andean countries,

which has not yet been a concern in international water resources agreements in the region but it is likely to gain interest in the near future.

Appendix: On Equation 2.41

In ARW-WRF3.4.1-Noah, the frozen soil moisture content in Eq. (2.41) is obtained by solving Eq. (A1) iteratively (Koren et al. 1999)

$$\frac{g\Psi_s}{L_f}(1+C_k\Theta_{ice})^2\left(\frac{\Theta-\Theta_{ice}}{\Theta_s}\right)^{-b}-\frac{T_{soil}}{T_{soil}+273.16}=0, \tag{A1}$$

where Ψ_s stands for saturation soil matric potential, L_f is latent heat of fusion, $C_k=8.0$ is a coefficient to account for the effect of increases in specific surface of soil minerals and ice-liquid water (Kulik 1978), b is a soil type dependent constant with an upper bound as 5.5[1] and T_{soil} is in ˚C. If Eq. (A1) cannot converge after 10 times of iterations, an explicit solution (A2) is granted, which is also the first guess during the iterative process.

$$\Theta-\Theta_{ice}=\Theta_s\left[\frac{L_f}{g\Psi_s}\left(\frac{T_{soil}}{T_{soil}+273.16}\right)\right]^{-\frac{1}{b}} \tag{A2}$$

Newton iteration is applied as follows,

1) Converting T_{soil} from ˚C into K, Eq. (A1) becomes

$$\frac{g\Psi_s}{L_f}(1+C_k\Theta_{ice})^2\left(\frac{\Theta-\Theta_{ice}}{\Theta_s}\right)^{-b}-\frac{T_{soil}-T_0}{T_{soil}}=0, \tag{A3}$$

[1] In Koren et al. (1999), b is a constant without soil type dependence.

where $T_0 = 273.15$, with $-T_0 + 273.16 \approx 0$ applied.

2) After natural logarithm,

$$\ln\left[\frac{g\Psi_s}{L_f}(1+C_k\Theta_{ice})^2\left(\frac{\Theta_s}{\Theta-\Theta_{ice}}\right)^b\right]-\ln\left(\frac{T_{soil}-T_0}{T_{soil}}\right)=0. \quad \text{(A4)}$$

3) Take $f(\Theta_{ice})=\ln\left[\frac{g\Psi_s}{L_f}(1+C_k\Theta_{ice})^2\left(\frac{\Theta_s}{\Theta-\Theta_{ice}}\right)^b\right]-\ln\left(\frac{T_{soil}-T_0}{T_{soil}}\right)$, such that

$$f'(\Theta_{ice})=\frac{2C_k}{(1+C_k\Theta_{ice})^2}+\frac{b}{\Theta-\Theta_{ice}}. \quad \text{(A5)}$$

4) Iteratively,

$$\Theta_{ice}(n+1)=\Theta_{ice}(n)-\frac{f(\Theta_{ice})}{f'(\Theta_{ice})}, \quad \text{(A6)}$$

until $\left|\Theta_{ice}(n+1)-\Theta_{ice}(n)\right| \le 0.005$ and $n \le 10$, where n denotes the number of iterations.

References

Arakawa, A., J.-H. Jung, and C.-M. Wu, 2011: Toward unification of the multiscale modeling of the atmosphere. Atmos. Chem. Phys., 11, 3731-3742.

Barros, A. P., 2013: Orographic precipitation, freshwater resources, and climate vulnerabilities in mountainous regions. Climate vulnerability: Understanding and addressing threats to essential resources. Academic Press, 57-78.

Barros, A. P., J. M. Putkonen, and D. W. Burbank, 2000: A study of the 1999 monsoon rainfall in a mountainous region in central Nepal using TRMM products and raingauge observations. Geophys. Res. Lett., 27, 3683-3686.

Barros, A. P., and T. J. Lang, 2003: Monitoring the monsoon in the Himalayas: Observations in central Nepal, June 2001. Mon. Wea. Rev., 131, 1408-1427.

Barros, A. P., and W. Hwu, 2002: A Study of land-atmosphere interactions during summertime rainfall using a mesoscale model. J. Geophys. Res., 107, doi 10.1029/2000JD000254.

Barthlott, C., and N. Kalthoff, 2011: A numerical sensitivity study on the impact of soil moisture on convection-related parameters and convective precipitation over complex terrain. J. Atmos. Sci., 68, 2971-2987.

Beiderwieden, E., A. Schmidt, Y. J. Hsia, S. C. Chang, T. Wrzesinsky, and O. Klemm, 2007: Nutrient input through occult and wet deposition into a subtropical montane cloud forest. Water Air Soil Pollut., 186, 273-288.

Beljaars, A. C. M., 1995: The parameterization of surface fluxes in large-scale models under free convection. Q. J. R. Meteorol. Soc., 121, 255-270.

Bhushan, S., and A. P. Barros, 2007: A numerical study to investigate the relationship between moisture convergence patterns and orography in central Mexico. J. Hydrometeor., 8, 1264-1284.

Chen, F., and J. Dudhia, 2001: Coupling an advanced land surface-hydrology model with the Penn State-NCAR MM5 modeling system. Part I: Model implementation and sensitivity. Mon. Wea. Rev., 129, 569-585.

Chen, F., and Coauthors, 2007: Description and evaluation of the characteristics of the NCAR high-resolution land data assimilation system. J. Appl. Meteorol. Climatol., 46, 694-713.

Costa, M. H., S. N. M. Yanagi, P. J. O. P. Souza, A. Ribeiro, and E. J. P. Rocha, 2007: Climate change in Amazonia caused by soybean cropland expansion as compared to caused by pastureland expansion. Geophys. Res. Lett., doi: 10.1029/2007GL029271.

DeMaria, M., 1985: Linear response of a stratified tropical atmosphere to convective forcing. J. Atmos. Sci., 42, 1944-1959.

Dickinson, R. E., and Kennedy P. J., 1992: Impacts on regional climate of Amazon deforestation. Geophys. Res. Lett., 19, 1947-1950.

Dirmeyer, P. A., R. D. Koster, and Z. Guo, 2006: Do global models properly represent the feedback between land and atmosphere?. J. Hydrometeor, 7, 1177-1198.

Moura, A. D., and J. Shukla, 1981: On the dynamics of droughts in northeast Brazil: Observations, theory and numerical experiments with a general circulation model. J. Atmos. Sci., 38, 2653-2675.

Eltahir, E. A. B., and R. L. Bras, 1994: Precipitation recycling in the Amazon basin. Q. J. R. Meteorol. Soc., 120, 861-880.

Emanuel, K. A., 1986: Some dynamical aspects of precipitating convection. J. Atmos. Sci., 43, 2183-2198.

Emanuel, K. A., 1994: Atmospheric convection. Oxford University Press, New York, 580 pp.

Emanuel, K. A., J. D. Neelin, and C. S. Bretherton, 1994: On large-scale circulations in convecting atmospheres. Q. J. R. Meteorol. Soc., 121, 1111-1143.

Emanuel, K. A., and M. Bister, 1996: Moist convective velocity and buoyancy scales. J. Atmos. Sci., 53, 3276-3285.

Figueroa, S. N., P. Satyamurty, and P. L. D. Silva Dias, 1995: Simulations of the summer circulation over the South American region with an Eta coordinate model. J. Atmos. Sci., 52, 1573-1584.

Fu, R., R.E. Dickinson, M. Chen, and H. Wang, 2001: How do tropical sea surface temperatures influence the seasonal distribution of precipitation in the equatorial Amazon?. J. Climate, 14, 4003-4026.

Garreaud, R. D., 1999: Multiscale analysis of the summertime precipitation over the central Andes. Mon. Wea. Rev., 127, 901-921.

Garreaud, R. D., 2000a: Intraseasonal variability of moisture and rainfall over the South American Altiplano. Mon. Wea. Rev., 128, 3337-3346.

Garreaud, R. D., 2000b: Cold air incursions over subtropical South America: Mean structure and dynamics. Mon. Wea. Rev., 128, 2544-2559.

Garreaud, R. D., M. Vuille, and A. Clement, 2003: The climate of the Altiplano: Observed current conditions and mechanisms of past changes. Palaeogeogr. Palaeoclimatol. Palaeoecol., 194, 5-22.

Garreaud, R. D., M. Vuille, R. Compagnucci, and J. Marengo, 2009: Present-day South American climate. Palaeogeogr. Palaeoclimatol. Palaeoecol., 281, 180-195.

Gill, A. E., 1980: Some simple solutions for heat-induced tropical circulation. Q. J. R. Meteorol. Soc., 106, 447-462.

Giovannettone, J. P., and A. P. Barros, 2009: Probing regional orographic controls of precipitation and cloudiness in the central Andes using satellite data. J. Hydrometeor., 10, 167-182.

Grimm, A. M., J. S. Pal, and F. Giorgi, 2007: Connection between spring conditions and peak summer monsoon rainfall in South America: Role of soil moisture, surface temperature, and topography in eastern Brazil. J. Climate, 20, 5929-5945.

Hastenrath, S., and L. Heller, 1977: Dynamics of climatic hazards in northeast Brazil. Q. J. R. Meteorol. Soc., 103, 77-92.

Holton, J. R., 2004: An Introduction to Dynamic Meteorology. 4th ed. Elsevier Academic: Burlington, MA, 535 pp.

Hong, S.-Y., Y. Noh, and J. Dudhia, 2006: A new vertical diffusion package with an explicit treatment of entrainment processes. Mon. Wea. Rev., 134, 2318-2341.

Hong, S.-Y., and J. Dudhia, 2012: Next-generation numerical weather prediction: Bridging parameterization, explicit Clouds, and large eddies. Bull. Amer. Meteor. Soc., 93, ES6-ES9.

Houze, Jr. R. A., 1993: Cloud Dynamics. Academic Press: San Diego, CA, 573 pp.

Huffman, G. J., R. F. Adler, D. T. Bolvin, G. Gu, E. J. Nelkin, K. P. Bowman, Y. Hong, E. F. Stocker, and D. B. Wolff, 2007: The TRMM multisatellite precipitation analysis (TMPA): Quasi-global, multiyear, combined-sensor precipitation estimates at fine scales. J. Hydrometeorol., 8, 38-55.

Iwasaki, H., 2004: Diurnal variation of precipitable water and convective activity with dual maxima in summer season around Mt. Tanigawa in the northern Kanto district. Japan. J. Meteor. Soc. Japan, 82, 805-816.

Jiang, Q., 2006: Precipitation over concave terrain. J. Atmos. Sci., 63, 2269-2288.

Jiménez, P. A., J. Dudhia, J. F. González-Rouco, J. Navarro, J. P. Montávez, and E. García-Bustamante, 2012: A revised scheme for the WRF surface layer formulation. Mon. Wea. Rev., 140, 898-918.

Jung, M., and Coauthors, 2010: Recent decline in the global land evapotranspiration trend due to limited moisture supply. Nature, 467, 951-954.

Kasahara, A., 1974: Various vertical coordinate systems used for numerical weather prediction. Mon. Wea. Rev., 102, 509-522.

Klein, S. A., 1997: Comments on "Moist convective velocity and buoyancy scales". J. Atmos. Sci., 54, 2775-2777.

Lackmann, G. M., and R. M. Yablonsky, 2004: The impact of the precipitation mass sink in tropical cyclones and other heavily precipitating systems. J. Atmos. Sci., 61, 1674-1692.

Lenters, J. D., and K. H. Cook, 1997: On the origin of the Bolivian High and related circulation features of the South American climate. J. Atmos. Sci., 54, 656-678.

Lefsky, M. A., 2010: A global forest canopy height map from the Moderate Resolution Imaging Spectroradiometer and the Geoscience Laser Altimeter System, Geophys. Res. Lett., 37, L15401, doi:10.1029/2010GL043622.

Li, L., W. Li, and A. P. Barros, 2013: Atmospheric moisture budget and its regulation of the summer precipitation variability over the Southeastern United States. Clim. Dyn., 41, 613-631.

Li, W., and R. Fu, 2004: Transition of the large-scale atmospheric and land surface conditions from the dry to the wet season over Amazonia as diagnosed by the ECMWF Re-analysis. J. Climate, 17, 2637-2651.

Lin, Y.-L., S. Chiao, T.-A. Wang, M. L. Kaplan, and R. P. Weglarz, 2001: Some common ingredients for heavy orographic rainfall. Wea. Forecasting, 16, 633-660.

Lin, Y.-L., 2007: Mesoscale Dynamics. Cambridge University Press, 674 pp.

Liu, C., E. J. Zipser, D. J. Cecil, S. W. Nesbitt, and S. Sherwood, 2008: A cloud and precipitation feature database from nine years of TRMM observations. J. Appl. Meteor. Climatol., 47, 2712-2728.

Lowman, L. E. L., and A. P. Barros, 2014: Investigating links between climate and orogeny in the central Andes: Coupling erosion and precipitation using a physical-statistical model. J. Geophys. Res., Under review.

Ma, H.Y., X. Ji, J. D. Neelin, and C. R. Mechoso, 2011: Mechanisms for precipitation variability of the astern Brazil/SACZ convective margin. J. Climate, 24, 3445-3456.

Mahrt, L. T., and J. Sun, 1995: The subgrid velocity scale in the bulk aerodynamic relationship for spatially averaged scalar fluxes. Mon. Wea. Rev., 123, 3032-3041.

Medvigy, D., R. L. Walko, and R. Avissar, 2011: Effects of deforestation on spatiotemporal distributions of precipitation in South America. J. Climate, 24, 2147-2163.

Mei, R., and G. Wang, 2010: Rain follows logging in the Amazon? Results from CAM3-CLM3. Clim. Dyn., 34, 983-996.

Neelin, J. D., and I. M. Held, 1987: Modeling tropical convergence based on the moist static energy budget. Mon. Wea. Rev., 115, 3-12.

Neelin, J. D., C. Chou, and H. Su, 2003: Tropical drought regions in global warming and El Niño teleconnections. Geophys. Res. Lett., 30: 2275, doi:10.1029/2003GL018625, 24.

Nitta, T., 1977: Response of cumulus updraft and downdraft to GATE A/B-scale motion systems. J. Atmos. Sci., 34, 1163-1186.

Oliveira, P. J. C., E. L. Davin, S. Levis, and S. I. Seneviratne, 2011: Vegetation-mediated impacts of trends in global radiation on land hydrology: a global sensitivity study. Global Change Biology, 17, 3453-3467.

Peñuelas, J., and M. Boada, 2003: A global change-induced biome shift in the Montseny mountains (NE Spain). Global Change Biology, 9131-140.

Rao, V. B., I. F. A. Cavalcanti, and K. Hada, 1996: Annual variation of rainfall over Brazil and water vapor characteristics over South America. J. Geophys. Res., 101, 26539-26551,

Rasmussen, K. L., S. L. Choi, M. D. Zuluaga, and R. A. Houze Jr., 2013: TRMM precipitation bias in extreme storms in South America. Geophys. Res. Lett., 40, 3457-3461.

Raymond, D. J., 1995: Regulation of moist convection over the west Pacific warm pool. J. Atmos. Sci., 52, 3945-3959.

Rennó, N. O., and A. P. Ingersoll, 1996: Natural convection as a heat engine: A theory for CAPE. J. Atmos. Sci., 53, 572-585.

Rodell, M., and Coauthors, 2004: The Global Land Data Assimilation System. Bull. Amer. Meteor. Soc., 85, 381-394.

Romatschke, U., and R. A. Houze Jr., 2010: Extreme summer convection in South America. J. Climate, 23, 3761-3791.

Salati, E., 1987: The forest and the hydrological cycle. The Geophysiology of Amazonia. R. E. Dickinson, Ed., John Wiley, New York, 273-296.

Salati, E., A. Dall'Olio, E. Matsui, and J. R. Gat, 1979: Recycling of water in the Amazon Basin: An isotopic study. Water Resour. Res., 15, 1250-1258

Salio, P., M. Nicolini, and A. C. Saulo, 2002: Chaco low-level jet events characterization during the austral summer season. J. Geophys. Res., 107, 4816, doi:10.1029/2001JD001315.

Silva Dias, P. L., W. H. Schubert, and M. DeMaria, 1983: Large-scale response of the tropical atmosphere to transient convection. J. Atmos. Sci., 40, 2689-2707.

Skamarock, W. C., J. B. Klemp, J. Dudhia, D. O. Gill, D. M. Barker, W. Wang, and J. G. Powers, 2008: A description of the advanced research WRF Version 3, NCAR Tech. Note, NCAR/TN-475+STR, 113 pp.

Skole, D., and C. Tucker, 1993: Tropical deforestation and habitat fragmentation in the Amazon: Satellite data from 1978 to 1988. Science, 260, 1905-1910.

Shukla, J. and Y. Mintz, 1982: Influence of land-surface evapotranspiration on the Earth's climate. Science, 215, 1498-1501.

Sun, X., and A. P. Barros, 2012: The impact of forcing datasets on the high-resolution simulation of tropical storm Ivan (2004) in the Southern Appalachians. Mon. Wea. Rev., 140, 3300-3326.

Sun, X., and A. P. Barros, 2013: High resolution simulation of Tropical Storm Ivan (2004) in the Southern Appalachians: Role of planetary boundary layer schemes and cumulus parameterization. Q. J. R. Meteorol. Soc., DOI: 10.1002/qj.2255.

Sun, X., and A. P. Barros, 2014: Isolating the role of surface evapotranspiration on moist convection along the eastern flanks of the Andes using a quasi-idealized approach. J. Atmos. Sci., In review.

Sun, X., and A. P. Barros, 2014b: Variations of the South Atlantic Convergence Zone associated with human induced LULC change over the Brazilian Highlands. In preparation.

Thomas, C. D., and Coauthors, 2004: Extinction risk from climate change. Nature, 427, 145-148.

Thompson, R. M., S. W. Payne, E. E. Recker, and R. J. Reed, 1979: Structure and properties of synoptic-scale wave disturbances in the intertropical convergence zone of the eastern Atlantic. J. Atmos. Sci., 36, 53-72.

Trenberth, K. E., and C. J. Guillemot, 1995: Evaluation of the global atmospheric moisture budget as seen from analyses. J. Climate, 8, 2255-2272.

Trenberth, K. E., J. T. Fasullo, and J. Kiehl, 2009: Earth's global energy budget. Bull. Amer. Meteor. Soc., 90, 311-323.

Vera, C., and Coauthors, 2006: The South American low-level jet experiment. Bull. Amer. Meteor. Soc., 87, 63-77.

Vizy, E. K., and K. H. Cook, 2007: Relationship between Amazon and high Andes rainfall. J. Geophys. Res., 112, D07107, doi:10.1029/2006JD007980.

Vuille, M., D. R. Hardy, C. Braun, F. Keimig, R. S. Bradley, 1998: Atmospheric circulation anomalies associated with 1996/1997 summer precipitation events on Sajama Ice Cap, Bolivia. J. Geophys. Res., 103, 11191-11204.

Walker, R., S. Sterz, E. Arima, and C. Simmons, 2011: The transamazon highway - past, present, and future. Engineering Earth. S. D. Brunn, Ed., Springer, 569-599.

Wei, J., and P. A. Dirmeyer, 2012: Dissecting soil moisture-precipitation coupling. Geophys. Res. Lett., 39, L19711, doi:10.1029/2012GL053038.

Werth, D., and R. Avissar, 2002: The local and global effects of Amazon deforestation. J. Geophys. Res., doi: 10.1029/2001JD000717.

Wild, M., 2012: Enlightening global dimming and brightening. Bull. Amer. Meteor. Soc., 93, 27-37.

Yanai, M., S. Esbensen, and J. Chu, 1973: Determination of bulk properties of tropical cloud clusters from large-scale heat and moisture budgets. J. Atmos. Sci., 30, 611-627.

Yanai, M., and R. H. Johnson, 1993: Impacts of cumulus convection on thermodynamic fields. The Representation of Cumulus Convection in Numerical Models, Meteor. Monogr. No. 46, Amer. Meteor. Soc. 39-62.

Yuter, S. E., and R. A. Houze, 1995: Three-dimensional kinematic and microphysical evolution of Florida cumulonimbus. Part II: Frequency distributions of vertical velocity, reflectivity, and differential reflectivity. Mon. Wea. Rev., 123, 1941-1963.

Biography

Xiaoming Sun was born in 1981, Zibo, China. After a long journey in universities (BS from China University of Mining and Technology, MS from Nanjing University and the University of Connecticut), he ultimately realized that atmospheric convection is his favorite topic, owing to the exposure to hurricane research during his early stay at Duke. In 2013, he visited the National Center for Atmospheric Research for three months to incorporate the observed global canopy height into the Advanced Research Weather Research and Forecasting model.

Sun, X., and A. P. Barros, 2010: An evaluation of the statistics of rainfall extremes in rain gauge observations, satellite-based and reanalysis products using Universal Multifractals. J. Hydrometeor, **11,** 388-404.

Sun, X., and A. P. Barros, 2012: The impact of forcing datasets on the high-resolution simulation of Tropical Storm Ivan (2004) in the Southern Appalachians. Mon. Wea. Rev., **140,** 3300-3326.

Sun, X., and A. P. Barros, 2013: High resolution simulation of Tropical Storm Ivan (2004) in the Southern Appalachians: Role of planetary boundary layer schemes and cumulus parameterization. Q. J. R. Meteorol. Soc., doi: 10.1002/qj.2255.

Sun, X., and A. P. Barros, 2014a: Isolating the role of surface evapotranspiration on moist convection along the eastern flanks of the Andes using a quasi-idealized approach. J. Atmos. Sci., In review.

Sun, X., and A. P. Barros, 2014b: Impact of Amazonian evapotranspiration on moisture transport and convection along the eastern flanks of the Andes. Q. J. R. Meteorol. Soc., In review.

Sun, X., and A. P. Barros, 2014c: Variations of South Atlantic Convergence Zone associated with human induced LULC change over the Brazilian Highlands. J. Climate, In preparation.

Sun, X., A. P. Barros, F. Chen, M. Barlage and J. Dudhia, 2014: Incorporating the global canopy height observations into the WRF model and its impact in South America. Q. J. R. Meteorol. Soc., In preparation.